UNIVERSITY OF OKLAHOMA

GRADUATE COLLEGE

INVESTIGATION OF THIN BED STRATA USING BOREHOLE IMAGE LOG AND HIGH RESOLUTION SEISMIC DATA

A Dissertation

SUBMITTED TO THE GRADUATE FACULTY

in partial fulfillment of the requirements for the

degree of

Doctor of Philosophy

By

Michelle Lynn Abraham
Norman, Oklahoma
2005

UMI Number: 3159277

ProQuest Information and Learning Company
300 North Zeeb Road
P.O. Box 1346
Ann Arbor, MI 48106-1346

INVESTIGATION OF THIN BED STRATA USING BOREHOLE IMAGE LOG AND HIGH RESOLUTION SEISMIC DATA

A Dissertation APPROVED FOR THE
SCHOOL OF GEOLOGY AND GEOPHYSICS

BY

____
John Castagna

____
Roger Slatt

____
Roger Young

____
Richard Hughes

____
Shengjie Sun

ACKNOWLEDGEMENTS

I would like to thank both of my advisors, Dr. John Castagna and Dr. Roger Slatt, for all of their support and guidance in completing my research. Dr. Castagna has provided tremendous insight and direction on this project. Dr. Slatt introduced me to this research topic and always provided financial support during my stay at the University. I have learned a lot from classes and interactions with both of them. Thank you for the wonderful lessons that you have taught me.

To the rest of my committee, Drs. Roger Young, Richard Hughes, and Shengjie Sun, I would like to thank them for their willingness to participate in this project, for their time, help and suggestions.

I would like to thank the School of Geology and Geophysics and the Society of Exploration Geophysicists for providing funding to me throughout my Doctorate program.

I would like to thank all of the staff and professors at the School of Geology and Geophysics for all of their help and assistance during my years here. I appreciate all of the professors that I have taken classes from during my time here.

To my husband, Brian, I would like to acknowledge and thank him for his constant encouragement, love, and support. I would like to thank my parents for their support and belief in education.

TABLE OF CONTENTS

CHAPTER 1. INTRODUCTION

Overview

A wealth of information is contained in borehole image log data. Generally, data from the borehole image log are presented on a commercial log as images of the borehole wall. These logs are then manually interpreted on a workstation for different geologic features. A very important feature of these logs is that they have a vertical resolution on the order of millimeters (Ekstrom et al.1986; Serra, 1989). Most conventional well logs have a vertical resolution on the order of 20 to 60 centimeters (Slatt, 2004). For example, the gamma ray log has a vertical resolution of approximately 30 centimeters in optimum conditions (McLaughlin, 2004). Seismic data has a much lower resolution which is subject to the velocity and frequency of the recorded data. The high vertical resolution of the borehole image log provides detail of the geology that other open-hole logs and seismic cannot provide. This aspect of the borehole image log allows investigation of fine layering that is not detected by coarser well logs and seismic data.

This study is focused on the use of the microresistivity curve data from the borehole image log to determine information about thin-bedded reservoirs of relevance to seismic exploration and wave propagation. The purpose of this dissertation is to show how geological and geophysical information can be extracted from Fullbore Formation MicroImager™[1] (hereafter referred to as FMI™) logs to obtain reservoir properties

[1] Trademark of Schlumberger

relevant to reservoir characterization and seismic exploration. In particular, algorithms to digitally compute bed boundaries, well log spectra, adjusted mean thickness, adjusted standard deviation, estimated transverse anisotropy, and modified Fischer plots automatically obtained from the digital microresistivity data are developed and applied.

Organization of Dissertation

There are eight chapters in this dissertation. Chapter 1 is the introduction. It covers why borehole image logs are used in this research, their application, and how they have been used in previous research. It also discusses the data source, the borehole image log, used in the work. Chapter 2 covers the data preparation steps as well as the software packages used to prepare the data. Chapter 3 includes the methodology and geological and statistical analyses conducted on the microresistivity curve. Chapter 4 discusses the geophysical analysis conducted on the microresistivity curve which includes estimating transverse anisotropy and well log spectral analyses. Chapter 5 includes the core and permeability correlation to the borehole image log and discusses the techniques employed to find a relationship between permeability and microresistivity. Chapter 6 discusses the introduction, methodology, and results of spectral decomposition analysis conducted on a high-resolution seismic line that was acquired in conjunction with the borehole image log. Chapter 7 provides the results of the peak frequency and bed thickness analysis on the high-resolution seismic line. Chapter 8 covers the discussion and conclusions of this research. Recommendations for further work are also provided.

APPLICATIONS

FMI™ logs have many reservoir applications including sedimentary and structural geological interpretations (Hansen and Fett, 2000). Sedimentary features such as sedimentary dip and paleocurrent direction can be obtained from these logs. Thin-bedded reservoirs and carbonate texture are other sedimentary features that can be identified with these logs. In addition, bedding features such as scours, bed boundaries between lithologic units, and laminated beds can be identified. Faults, fractures, and structural dip are structural features identified from borehole image logs. These logs have also been used for larger scale geological purposes such as comparisons to outcrops, cores, and open-hole logs and to create a stratigraphic log to determine stratigraphic thinning and thickening trends of beds.

Borehole image logs have been used to compare features identified on the outcrop with those on an associated borehole image log (Slatt et al, 1994). Sullivan and Schepel (1995) used borehole image logs along with core and other open-hole logs to obtain hydrocarbon sand thickness in the Gulf of Mexico region. Borehole image log data was utilized to create Modified Fischer Plots to correlate relatively conformable successions of genetically related beds bounded by marine-flooding surfaces (Hurley, 1996). Simultaneous Acoustic and Resistivity Imaging Log, STAR™[1] data was used to analyze thin-beds in the Northern Gulf of Mexico (Pavlovic, 1999). Witton-Barnes et al., (2000)

[1] Trademark of Baker-Hughes

used a STAR™ borehole image log to correlate laterally continuous and discontinuous turbidite deposits to an outcrop in the Dad Sandstone Member of the Lewis Shale, south central Wyoming. A STAR™ borehole image log was used for detailed interpretation of bedding features and sedimentary structures as well as for displaying lithofacies that were calibrated with core data (Goolsby et al, 2001). The use of FMI™ borehole image logs along with outcrop and other subsurface data helped to obtain information about the geology of the Mt. Messenger Formation, New Zealand (Browne and Slatt, 2002).

In the research projects previously discussed, the borehole image log data was used as a tool to complement other geological data such as cores, open-hole logs, and outcrops. Also, it was used to aid in providing more details about the geology in a particular area and to provide information about the stratigraphic thinning and thickening trends of strata.

All of the literature previously discussed uses the borehole image log data by manually obtaining information from the "electrical" picture that is provided from this tool. In this dissertation research, the use of the borehole image log data follows a different approach. This research focuses on extracting various geological and geophysical parameters from the microresistivity values of a FMI™ borehole image log.

One technique developed in this research is an automatic bed boundary detection algorithm. The output from the algorithm is then used to generate the modified Fischer plots. Currently, these plots are manually intensive to generate. A geologist calculates the modified Fischer plots after manually picking bed boundaries from the borehole image log. The geologist then has to transfer the information to a spreadsheet and through various computations generate the modified Fischer plots.

The automated bed boundary detection algorithm developed in this dissertation minimizes the time needed to construct these plots and eliminates the subjectivity of the manual bed boundary picking. Other utilizations of the bed boundary detection results are the extraction of various statistics related to properties of beds.

Another objective of this research is to use the results from the bed boundary algorithm to generate modified Fischer plots (Hurley, 1996). In this dissertation, the modified Fischer plots are to be generated via automated methods. This is unique because currently there are no commercial products available to automatically generate modified Fischer plots.

FUNDAMENTAL CONCEPTS OF BOREHOLE IMAGE LOGGING

Borehole image logs include the Formation MicroScanner™[1] (FMS™[1]), the Fullbore Formation MicroImager™ (FMI™), and the Simultaneous Acoustic and Resistivity Imaging Log™ (STAR™). The borehole image log used in this research is the FMI™ and the following fundamental concepts will pertain to this particular type of log.

[1] Trademark of Schlumberger

In one embodiment, the tool is composed of an upper electrode and eight lower electrode assemblies. The lower electrode assemblies are each composed of one pad and one flap. Both the pad and flap contain two horizontally offset rows of twelve electrode buttons per row as shown in Figure 1.1.

Figure 1.1. Pad and flap assembly of the Formation MicroImager™ tool showing horizontally offset rows of electrode buttons (Schlumberger, 2002).

The tool is driven by an applied voltage causing an alternating current flow to each of the lower electrode buttons through the formation to the upper electrode. The current from the lower electrode (pad or flap) initially focuses on the formation facing the button but expands to measure a larger portion of the formation between the lower and upper electrodes. The formation conductivity of the borehole wall is thus measured. There is a special focusing circuitry that ensures the measuring currents are forced into the formation (Schlumberger, 2002). The current then produces both a low and high frequency component of conductivity. The low frequency component produces the lithological and petrophysical information. The high frequency component provides the microresistivity data used for imaging and dip interpretation.

This particular tool generates an electrical image or "picture" of the borehole wall from 192 simultaneous microresistivity measurements. The picture is fit to a color scale creating a color image of the borehole wall. The lighter colors on the color bar correspond to higher resistivities and the darker colors correspond to low resistivities.

Fullbore FMI™ logs provide microresistivity formation images only in water-based muds. This is a limitation in areas where water-based muds cannot be used in logging. However, there is an Oil-Base MicroImager tool™[1] (OBMI™[1]) that can provide microresistivity formation images in oil-based muds (Schlumberger, 2001). The OBMI™ has a lower resolution (3 centimeters) than the FMI™, so it provides a lower resolution "electrical" picture of the borehole wall.

[1] Trademark of Schlumberger

The depth of investigation for the FMI™ is similar to a shallow lateral resistivity tool, approximately 72 cm. The image resolution in vertical and azimuthal directions is 5 mm.

SEISMIC RESOLUTION

Seismic resolution is the ability to distinguish between separate points (Vertical Resolution Horizontal Resolution Fresnel Zone, 2004) or objects on seismic data. The resolution is the minimum distance between two objects where each object can be discernible. The velocity, frequency, and wavelength of the seismic data determine the resolution. There are two kinds of seismic resolution: temporal and spatial (Young, 1999).

The temporal or vertical resolution of the seismic data determines if the top and bottom of a bed or a boundary between two beds can be discerned. In order for a bed to be resolvable, the minimum thickness of the bed must be ¼ wavelength of the predominant seismic frequency. The ability to resolve boundaries decreases with depth due to attenuation of the seismic signal.

The spatial or horizontal resolution determines how close two objects can be and still be recognized as two separate objects. The horizontal resolution depends on the frequency and velocity of the seismic data. The Fresnel zone is used to determine the horizontal resolution of the seismic data.

This research focuses on vertically distinguishable features, thus only the temporal or vertical resolution is applied.

DESCRIPTION OF THE EXPERIMENT

The dataset was acquired in the Taranaki Peninsula, New Zealand area from the late Miocene Mount Messenger Formation as a research and learning tool for deep-water turbidites (Browne and Slatt, 2002). This dataset provides a better understanding of the thin-bedded, deep-water reservoir lithofacies through the combined outcrop and behind-outcrop studies that were conducted there.

The complete dataset gathered for the original study consists of (1) two behind-outcrop borehole image logs (FMI™), Platform Express™ logs, and core from behind a 200 meter thick, 4 kilometer long coastal outcrop section, (2) characterization of the vertical and lateral attributes of the cliff strata in front of the location of the boreholes, and (3) a high-resolution (150-hertz) 2D seismic line obtained on the beach in front of the cliff face (Figure 1.2). The two wells are named the North and Central well.

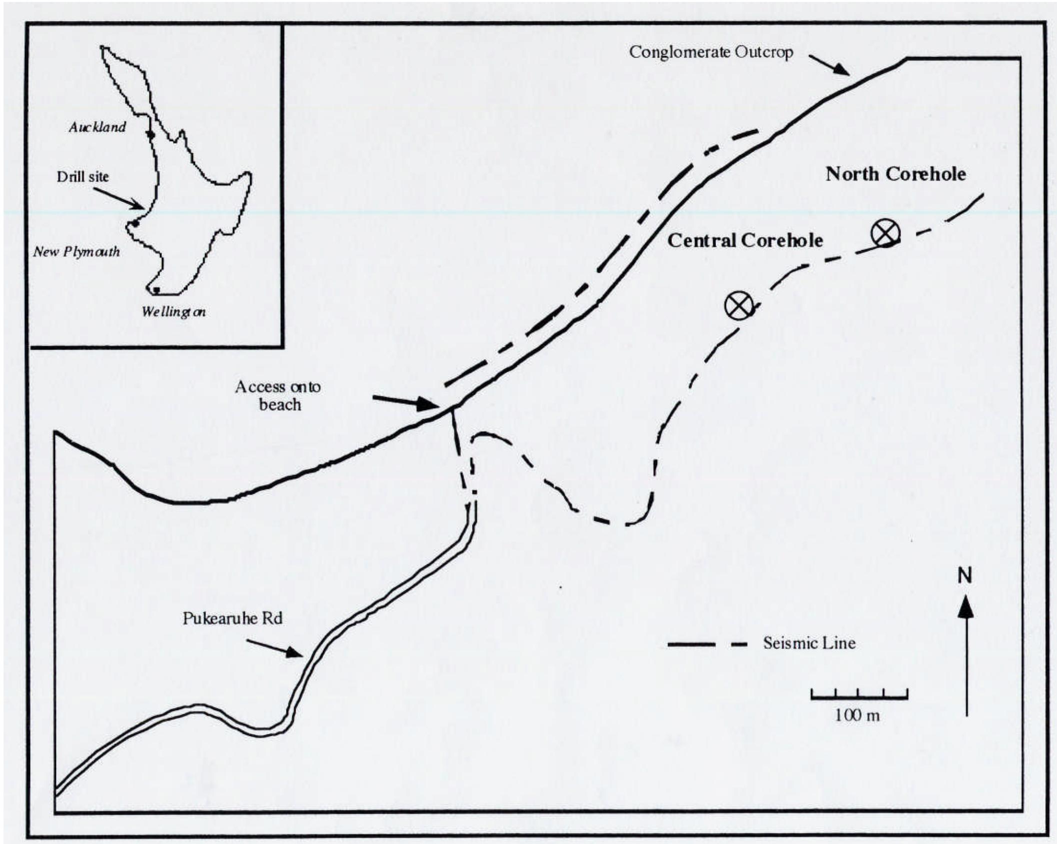

Figure 1.2. Map of New Zealand showing North and Central boreholes and seismic line (dashed line). Inset of New Zealand with field area location indicated by arrow (Spang 2000).

The data obtained for this research was (1) one unprocessed borehole image log from Schlumberger, (2) Platform Express™[1] (conventional log data) (3) data from a Masters' thesis (Spang, 2000), and (4) the high-resolution seismic line. The data from Spang's thesis include core description from the North well, rock velocity and permeability data. The North well microresistivity data was used in this dissertation.

[1] Trademark of Schlumberger

The North borehole image log is 46 meters long. The starting depth for the run is 24 meters. The borehole image log data was collected at 2.5 mm intervals. The core description is for the cored interval from 24 meters to 71 meters. There are two small gaps in the core at 30.50 meters and 36 meters. These gaps are 23 cm and 14 cm, respectively. The high-resolution seismic line is 500 meters long.

The microresistivity curve was used to develop a bed boundary detection algorithm and various statistical treatments of bed thickness measurements.

The borehole image log was processed at the University of Oklahoma in Schlumberger's GeoFrame™[1] software package. The processed borehole image log curves were then exported from GeoFrame™ and imported into Microsoft Excel™[2]. The calculations and computations for this research were then completed in Excel™.

Spectral decomposition analysis was run on the seismic data and the results were displayed in the 2d/3d Pak from Seismic Micro-Technology™[3] software package.

[1] Trademark of Schlumberger

[2] Trademark of Microsoft

[3] Trademark of Seismic Micro-Technology

GEOLOGICAL SETTING

The North well is a research well drilled behind an outcrop in the Taranaki Basin, New Zealand (Browne and Slatt, 2002; Figure 1.2). This well is 46 meters deep and was drilled about 100 meters behind a vertical cliff face. The well was drilled into the Miocene age Mount Messenger Formation. The Mount Messenger Formation contains two deep-water turbidite types: basin floor fans and channel-levee complexes (King et al., 1994; Coleman et al, 1998a, b; Browne et al., 2000; Browne and Slatt, 2002). The Mount Messenger Formation consists of well-sorted, very fine to fine-grained sandstone and siltstone. The channel levee facies contain thin-bedded, planar-laminated, climbing-ripple-laminated sandstone and massive siltstone (Browne and Slatt, 2002).

The North well contains both proximal and distal levee facies. In core, the proximal levee sandstones are dominantly planar-laminated Bouma Tb beds. (Browne and Slatt, 2002). Massive (Ta) and climbing-ripple-laminated (Tc) sandstones are found in the proximal levee, but are less common than the planar-laminated sandstones (Browne and Slatt, 2002). Scour surfaces are also common (Browne and Slatt, 2002). The proximal levee deposits consist of 60% to 80% sandstone beds (Browne and Slatt, 2002). Bouma Te makes up approximately 40% of the proximal levee deposits (Browne and Slatt, 2002). The distal levee facies are comprised of siltstone beds and relatively thin sandstones (Browne and Slatt, 2002). Bioturbated siltstone (Te) is found in the outcrop. Planar-laminated (Tb) and climbing-ripple-laminated (Tc) sandstones as well as sparsely found massive sandstones (Ta) are located in the outcrop (Browne and Slatt, 2002).

From 25% to 50% of distal levee deposits consist of sandstone beds (Browne and Slatt, 2002). The proximal levee and overbank correspond to the depth interval from 24 meters to 42 meters on the borehole image log. The distal levee and overbank deposits occur from 42 meters to the base of the core.

The Central well is another research well drilled behind the same outcrop in the Taranaki Basin, New Zealand (Browne and Slatt, 2002; Figure 1.2). The Central well is 105 meters deep and is located west of the North well. In this research the Central well location was used in the interpretation of the spectral decomposition results since (1) it is a deeper well than the North well, (2) there are more depositional facies packages identified on this well than on the North well, and (3) the depositional facies packages have been recorded in previous research (Spang 2000).

The Central well contains both channel-fill and distal levee facies. The channel-fill deposits are filled with conglomerate, planar-laminated sandstone (Tb), climbing-ripple-laminated sandstone (Tc), and massive siltstone (Te) (Browne and Slatt, 2002). The channel-fill deposits are comprised of 25% to 80% sandstone beds. In the core, the planar-laminated sandstone (Tb) is the most common Bouma interval found in the channel-fill deposits (Browne and Slatt, 2002). Also, ripple- and climbing-ripple laminated sandstone (Tc) and massive sandstone (Ta) Bouma sequences are found in these channel-fill deposits, but are less abundant than planar-laminated sandstones (Browne and Slatt, 2002). Planar-laminated (Tb) and climbing-ripple laminated (Tc) sandstones are more abundant in the outcrop (Browne and Slatt, 2002). For the channel fill deposits, the Central well contains over 60% abundance of Bouma Te, less than 10% for Bouma Ta and Td, and between 10% to 20% for Bouma Tb and Tc (Browne and Slatt, 2002).

The massive sandstones (Ta) are up to 50 cm thick and are moderately to well-sorted, medium to very fine-grained sandstone (Browne and Slatt, 1997). Bouma Tb horizontally-laminated sandstones are up to 80 cm thick and are well-sorted, and fine- to very fine-grained (Browne and Slatt, 1997). Ripple and climbing ripple-laminated sandstone (Tc) have beds up to 50 cm thick (Browne and Slatt, 1997). These sandstones are well-sorted, fine- to very fine-grained carbonaceous sandstone (Browne and Slatt, 1997). Massive siltstones (Te) are up to 20 cm thick and consist of very fine-grained sandy siltstone with variable clay content (Browne and Slatt, 1997).

CHAPTER 2. DATA PREPARATION

This chapter discusses the preparation of the data used in this research. The two types of data discussed are the microresistivity measurements from one borehole image log and one high-resolution seismic line.

BOREHOLE IMAGE LOG PREPARATION

The format of the borehole image log data is a Digital Log Information Standard (DLIS) formatted file. The DLIS file is a standard file format that can be read into Schlumberger's GeoFrame™ software package. The raw microresistivity data was loaded and processed using Schlumberger's processing flow (Schlumberger, 1999). The processing flow is as follows:

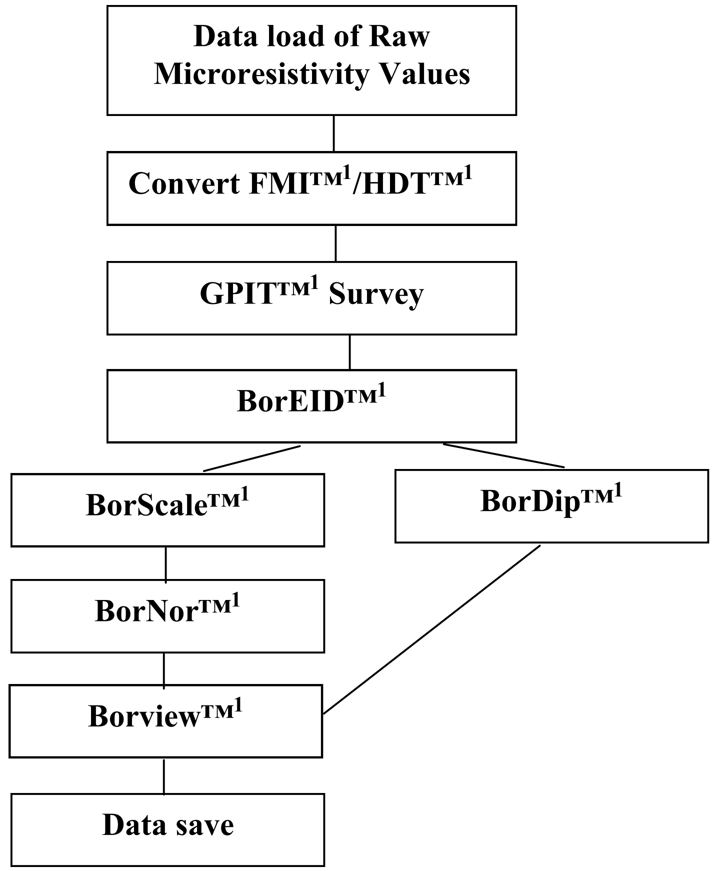

One purpose of the processing flow is to convert the raw microresistivity data into the best visual representation of the data. The data load module reads the raw field data files. The purpose of the convert FMI™/HDT™ module is to change the field data format into a more convenient form for processing. The primary function of the GPIT™ Survey module is to validate the quality of microresistivity data.

[1]Trademark of Schlumberger

The BorEID™ module has several important functions in the processing of the borehole image logs. The BorEID™ module performs the equalization of the buttons, corrections for the emitter exciter (EMEX) voltage, magnetic declination corrections, speed corrections, and dead button repair. Since each of the electrode buttons make an independent uncalibrated measurement of relative conductivity, equalization of the buttons is necessary to provide a uniform response. The equalization works by ensuring the mean and standard deviation of the measured values are the same as the mean and standard deviation of all of the data from the whole pad over the entire processed interval. This procedure amplifies the signal from the weak buttons and reduces the signal of the strong ones. In addition to the equalization procedure, the BorEID™ module makes corrections for the effects of changing the EMEX voltage. This correction allows the output to be more comparable to a calibrated resistivity tool. Both the speed corrections and the magnetic declination corrections are made in the BorEID™ module. There are two methods for the speed corrections. One method employs the accelerometer information and the other is an image-based method. Both of these methods are used to make the speed corrections. The measured data is at its true depth in the well once all of the speed corrections have been made. Based on the comparison of the overall button response, BorEID™ attempts to locate and repair individual bad buttons. Buttons that are dead or show little activity are replaced with the average of the adjacent buttons.

The last steps in the processing procedure are to run the BorScale™, BorDip™, BorNor™, Borview™, and Data Save modules. Calibration of the image with a shallow resistivity log is done in the BorScale™ module. The BorDip™ module attempts to automatically detect beds and then computes the dip magnitude and direction of those beds. Reasons for developing a new bed boundary detection technique instead of using BorDip™ are discussed in Chapter 3. To create a dynamic image of the borehole image log the BorNor™ module is used. BorNor™ normalizes the image to enhance the image contrast. The interactive or manual interpretation of the borehole image log is done in the Borview™ module. The Data save module saves all of the results of processing and interpretation.

All of these modules were used in the processing procedure except BorScale™ since a shallow resistivity log was not available at the start of this research. However, a high-resolution shallow resistivity laterolog was acquired at a later time and was used to calibrate the microresistivity data. Because the shallow resistivity log was received late in this research, some of the analyses used the uncalibrated microresistivity data. It is noted throughout this dissertation whether each analysis used calibrated or uncalibrated data. All of the Schlumberger default and suggested parameters were used to complete the processing of the borehole image log.

Once the processing was completed on the borehole image data, the 192 processed microresistivity curves were exported from GeoFrame™ into Microsoft Excel™. Of the 192 curves, one curve was chosen for all of the analyses. Specifically, curve 6 from Pad 1 was chosen. A thin green line indicates Pad 1 on the borehole image log in BorView™. Curve 6 was chosen to use in the analysis since it is one of the middle electrode buttons on the pad.

SEISMIC DATA PREPARATION

The high-resolution seismic line used in this research was shot along the beach in front of the outcrop cliff where the Miocene Mount Messenger Formation sediments are exposed. This seismic line was shot in parts and merged. This seismic line is 12 fold data and is 822.5 meters long. The instrument used to record the data was a 48-channel Sercel 338HR acquisition system. The basic recording system and parameters of the data are:

- Common depth point spacing was 2.5 meters
- Symmetric split spread geometry
- Shot spacing was 10 meters
- Group interval was 10 meters
- Near offset was 2.5 meters
- Far offset was 117.5 meters
- Record length was 3 seconds
- Sample rate was 1 millisecond
- 10 Hertz low cut filter
- The source was a 40 g of Powergel
- 40 Hertz single geophones were used

This line was processed through to final stack and migration by the New Zealand Institute of Geological and Nuclear Sciences using an in-house developed processing system. Noisy traces and spikes were edited. The shot gathers were used to find the optimum filter and deconvolution parameters. The line shows a very uniform and water saturated sand at the surface so refraction statics analysis was not performed since static problems were not expected. Relative amplitudes preserved (RAP) processing was applied to this data and a second processing sequence using amplitude gain control (AGC) as a pre-stack trace balance was used. The AGC applied data was used for velocity analysis and the analysis was done using constant velocity stacks. After the initial velocity analysis, residual statics were calculated and then recalculated after a second velocity analysis. Manual trace editing was done to suppress noisy traces before stacking in the RAP processing sequence. Deconvolution, filtering, and a coherency filter through deconvolution in the FX domain were part of the post stack processing sequence. The final stack was migrated using finite-difference migration.

The processed seismic line was taken into a spectral decomposition software package, INSPECT™. The analysis was broken into the overlay and residual components that were run from 1 to 400 hertz. The results from the analysis were imported into Seismic Micro-Technology's 2d/3d Pak™ for interpretation.

CHAPTER 3. GEOLOGICAL BOREHOLE IMAGE LOG ANALYSIS

This chapter discusses all of the geological methods and results used in the analyses of the processed uncalibrated microresistivity curve. The following procedures will be discussed: the bed boundary picking algorithm, the Modified Fischer Plot technique, adjusted mean thickness adjusted for threshold, standard deviation plots adjusted for threshold, and Modified Fischer Plot with zero threshold. All of the analyses discussed in this chapter were calculated using Microsoft Excel™.

BED BOUNDARY PICKING ALGORITHM

Picking bed boundaries from borehole image logs can be done interactively, which can be manually intensive. There are software packages such as Schlumberger's GeoFrame™ and TerraScience's TerraStation™ that will automatically generate bed boundaries and dips of beds. These software packages do not always provide the best bed boundary demarcation and were not used in this research. Through personal experience working with one of these programs, the automatic bed boundaries picked by the program did not match the bed boundaries that were manually picked. In general, geologists do not rely on the automated bed boundary picking, instead they use the manual approach. The objective of the bed boundary picking algorithm in this dissertation is to reduce subjectivity, time and cost of manual picking, and create an algorithm that can be used on any PC without incurring great expense or requiring a lot of experience.

The objective of the bed boundary picking algorithm in this research was twofold. One purpose of the algorithm was to generate bed boundaries automatically. Another purpose of the algorithm was to use the bed boundary information to create Modified Fischer Plots.

The bed boundary picking algorithm is a two step program. The first step is to use the sliding windowed difference equation to detect bed boundaries. This equation was a smoothing routine and helped to bring out the sharp boundary contacts. The second step was to use logic statements to enhance the bed boundaries and eliminate the background noise.

The sliding windowed difference equation is:

$$\sum_{j=n-1}^{j=n-4} b_j - \sum_{j=n+1}^{j=n+4} b_j \tag{3.1}$$

where b_j = microresistivity value at row j and n = row in the Excel™ spreadsheet representing the starting point for the equation and where the result will be placed.

There were 18, 426 microresistivity values that were used to compute the sliding windowed difference calculations in Excel™. These values extend the length of the log (24 to 70.8 meters) and the depth step for this log ranges from 0.0025 to 0.0026 meters. From the above equation, eight microresistivity values from eight depth steps were taken into account. Using this equation on the microresistivity data resulted in a log curve with prominent peaks and troughs (Figure 3.1).

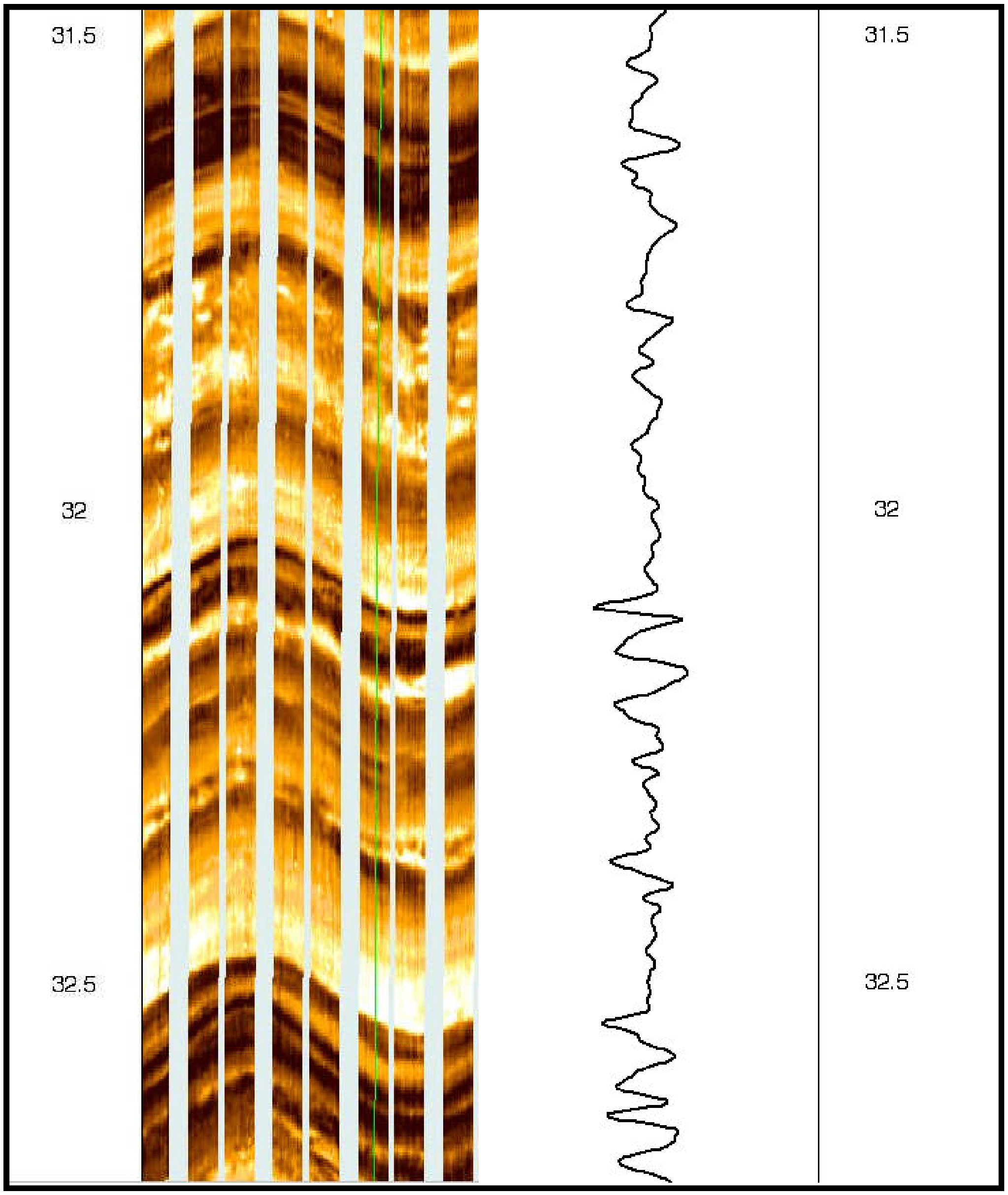

Figure 3.1. Borehole image log (left) and sliding window difference equation results (right). Depth shown in meters. Scale 1:6 (1.7cm:10cm).

To reduce the background noise and enhance the bed boundaries, a series of six nested IF statements and arbitrary threshold values were used in Excel™. *A threshold in this research is defined as a minimum value that the magnitude of any given data point must exceed to be further considered a potential bed boundary.* The threshold values that were tested were 10, 30, 50, 70, and 100 (Figures 3.2, 3.3, 3.4, 3.5, 3.6, and 3.7). These values are unitless because the microresistivity values are unitless. The FMI™ log is designed to measure contrast and it is not designed to make an absolute measurement (Schlumberger, 2003). However, a properly scaled image or an image scaled to a shallow resistivity log can have units of a "pseudo conductivity" log (Schlumberger, 2003). The units would then be microSiemens per meter (mS/m).

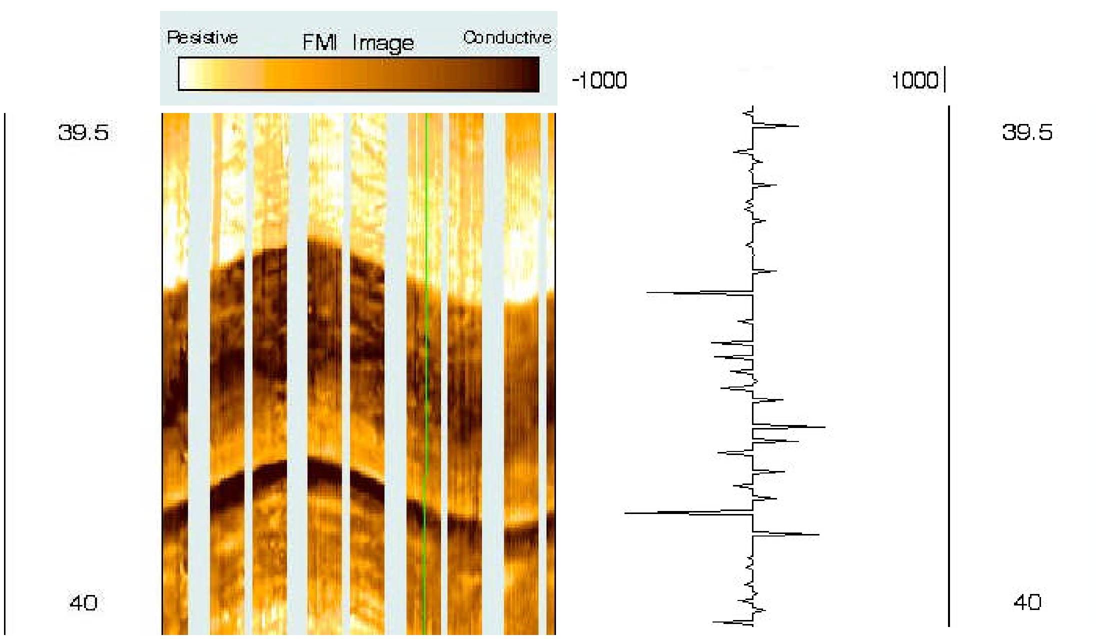

Figure 3.2. Borehole image log (left) with vertical scale of depth (meters). The darker colors are more conductive and the lighter colors are more resistive on the borehole image log. Bed boundary detection results (right) for threshold 10. The vertical scale (meters) is depth and the horizontal scale is microresistivity. Scale 1cm:6cm.

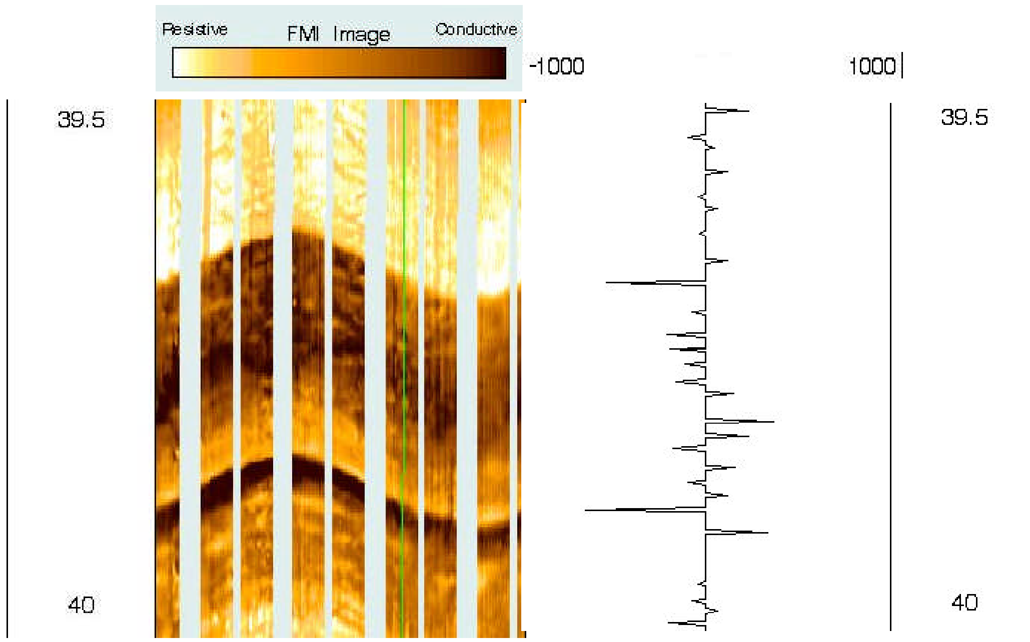

Figure 3.3. Borehole image log (left) with vertical scale of depth (meters). The darker colors are more conductive and the lighter colors are more resistive on the borehole image log. Bed boundary detection results (right) for threshold 30. The vertical scale (meters) is depth and the horizontal scale is microresistivity. Scale 1cm:6cm.

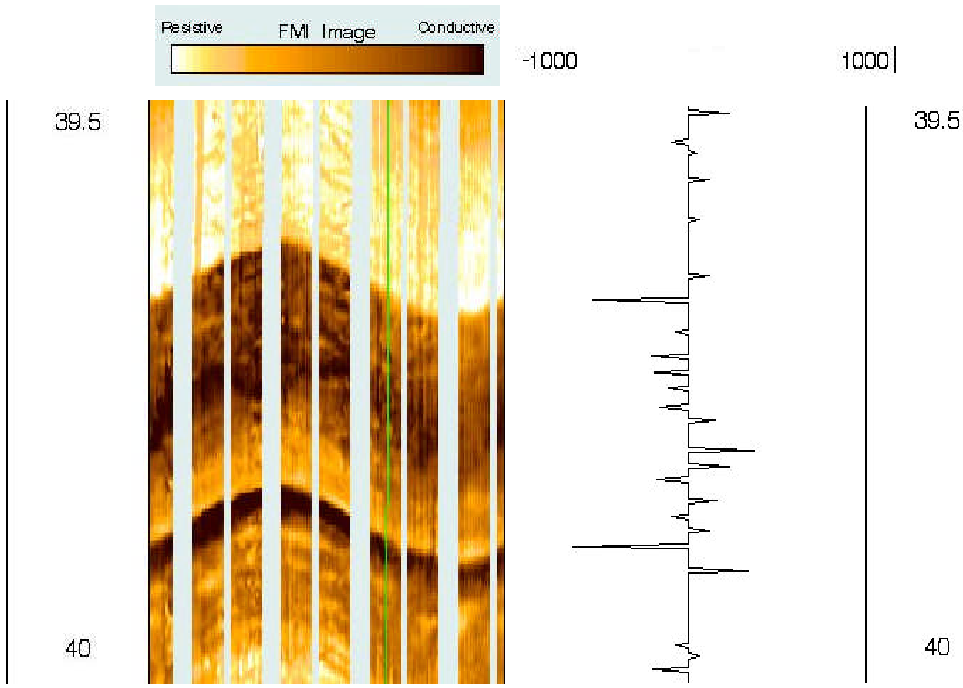

Figure 3.4. Borehole image log (left) with vertical scale of depth (meters). The darker colors are more conductive and the lighter colors are more resistive on the borehole image log. Bed boundary detection results (right) for threshold 50. The vertical scale (meters) is depth and the horizontal scale is microresistivity. Scale 1cm:6cm.

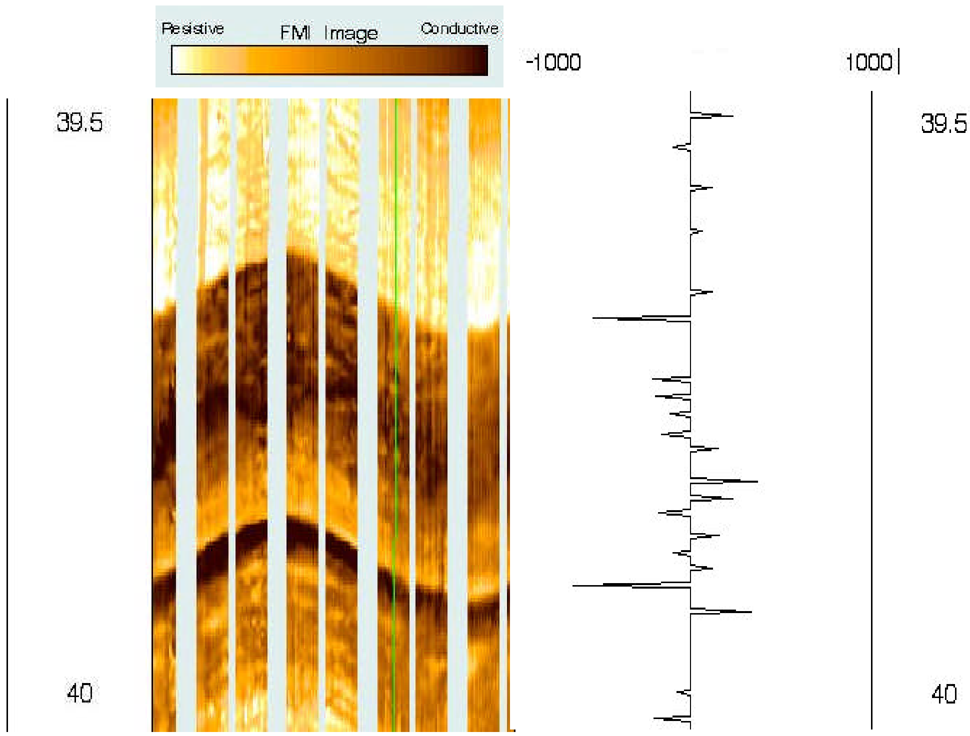

Figure 3.5. Borehole image log (left) with vertical scale of depth (meters). The darker colors are more conductive and the lighter colors are more resistive on the borehole image log. Bed boundary detection results (right) for threshold 70. The vertical scale (meters) is depth and the horizontal scale is microresistivity. Scale 1cm:6cm.

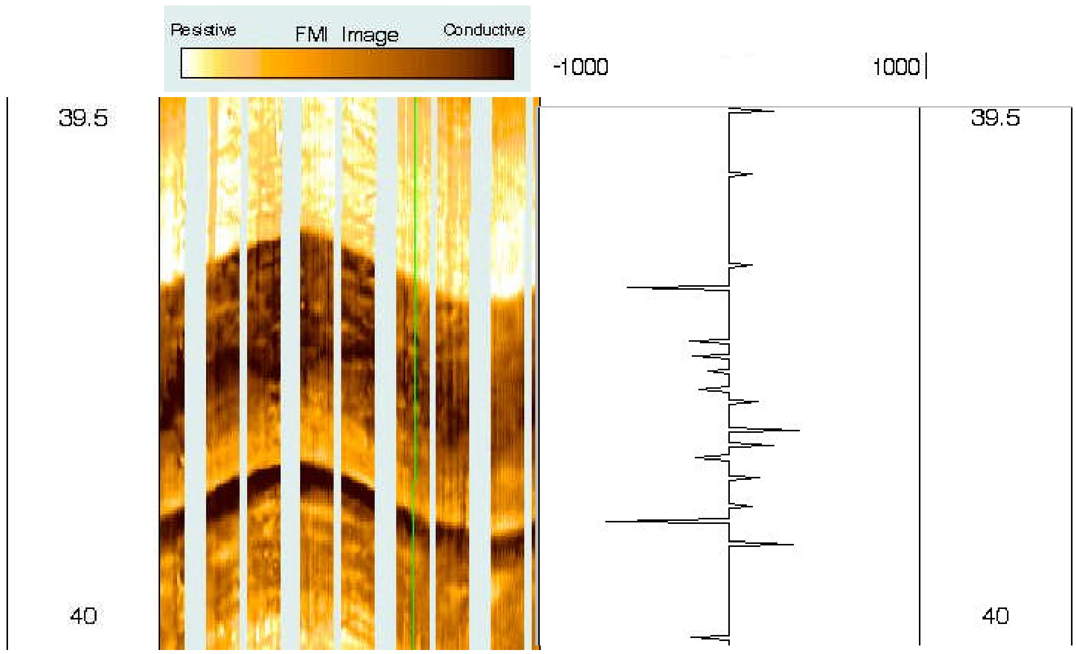

Figure 3.6. Borehole image log (left) with vertical scale of depth (meters). The darker colors are more conductive and the lighter colors are more resistive on the borehole image log. Bed boundary detection results (right) for threshold 100. The vertical scale (meters) is depth and the horizontal scale is microresistivity. Scale 1cm:6cm.

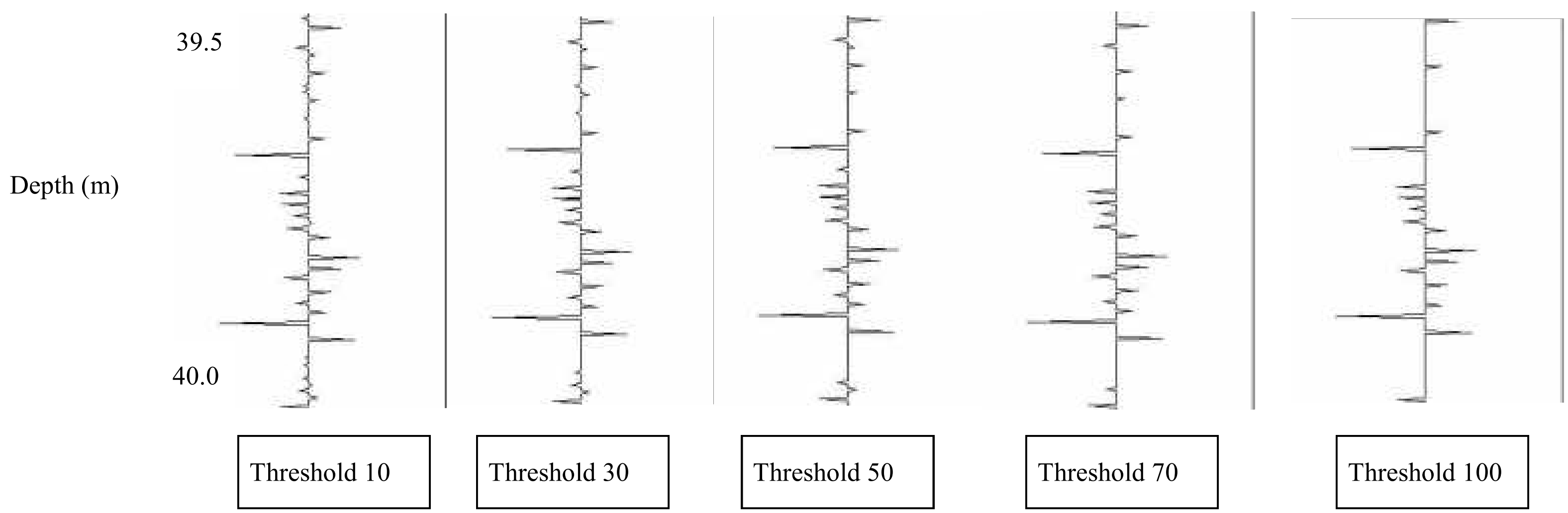

Figure 3.7. Bed boundary detection results for thresholds 10, 30, 50, 70, and 100.

The IF statements were established to analyze each sliding window difference value and evaluated if the values were larger than the threshold range. Once it was determined that the value was less than or greater than the given threshold value, the IF statements tested the adjacent values. Any value that fell less than the threshold range was not considered a bed boundary and therefore was not further analyzed in the nested IF statements.

BED BOUNDARY PICKING ALGORITHM: RESULTS

As the threshold value increased, fewer bed boundaries were identified. The threshold value and number of detected bed boundaries are inversely related (Table 3.1).

Threshold	Number of Bed Boundaries
10	2682
30	2541
50	2403
70	2260
100	2076

Table 3.1. Number of bed boundaries per threshold value for the depth interval from 24.005 m to 70.8 m.

MODIFIED FISCHER PLOTS

Modified Fischer Plots have been used to correlate relatively conformable successions of genetically related beds bounded by marine-flooding surfaces in subsurface reservoirs (Hurley, 1996). These groupings of beds are referred to as parasequences. Individual parasequences within deep marine sediments such as turbidites can be difficult to identify and correlate on conventional logs. However, the parasequence boundary correlations using the Modified Fischer Plots are based on high vertical resolution bed boundary detections that can be obtained from borehole image logs or dipmeter data. In this research, bed boundaries were obtained from a high resolution borehole image log. Then, calculations based on the stratigraphic depths of bed boundaries are generated in a spreadsheet to create the Modified Fischer Plot. The resulting plot can be used as a well log trace for correlating parasequences between wells (Hurley, 1996).

There are five steps in the Modified Fischer Plot technique once the bed boundaries are picked (Hurley, 1996) (Table 3.2). In the previous research that used Modified Fischer Plots, the bed boundaries are picked according to a cycle. Hurley (1996) defines a cycle as a pair of sandstone-shale or limestone-shale beds or laminae. For the first step, the tops of the cycles are picked and the thicknesses of the cycles are calculated. Once the cycle thicknesses are generated, the mean cycle thickness is calculated. The mean cycle thickness is then used to calculate the departure from mean cycle thickness. Departure from mean cycle thickness is calculated by subtracting the mean cycle thickness value from each of the thicknesses. The next step in the Modified Fischer Plot technique is to calculate the dimensionless departure from mean cycle thickness. This is calculated by dividing each departure from mean cycle thickness value by the mean cycle thickness. The last step in the Modified Fischer Plot technique is to calculate the cumulative dimensionless departure from mean cycle thickness. This is calculated by successively adding each dimensionless departure from mean cycle thickness value from the deepest bed through the shallowest bed. Beginning with the deepest bed maintains consistency with stratigraphic level.

MODIFIED FISCHER PLOT

Cycle Number	Cycle Top (ft.)	Cycle Thickness (ft.)	Departure from Mean Cycle Thickness	Dimensionless Departure from Mean Cycle Thickness	Cumulative Dimensionless Departure from Mean Cycle Thickness
283	14036	0.88	0.21	0.31	
282	14037	0.24	-0.43	-0.64	

260	14045	0.43	-0.24	-0.35	0.50
259	14045	0.78	0.12	0.18	0.85
258	14046	1.12	0.45	0.67	0.67

•Mean Cycle Thickness (MCT) ***for this sequence*** = 0.67ft.
•Dimensionless Departure from MCT =Departure from MCT/MCT

Table 3.2. Example of Modified Fischer Plot calculations using sample data (Slatt, 2001).

Modified Fischer Plots were used in a thesis on turbidites in the Miocene Mount Messenger Formation (Spang, 2000). This dissertation uses the same data as Spang (2000). In Spang's research, Modified Fischer Plots were manually generated and used to obtain geological data about the strata. Spang was able to distinguish if cycles were stratigraphically thinning, thickening, or remaining constant using the Modified Fischer Plots. Changes in the thickness of the beds can be determined by the varying slope of the

Modified Fischer Plot. Thinning beds are indicated by a negative slope, beds that are thickening are indicated by a positive slope, and beds with no change in thickness are indicated by a vertical trend or no slope.

In this dissertation, a cycle is defined differently than that of Hurley (1996). It is defined as an individual bed as detected by the bed boundary detection algorithm. Thus each boundary is a demarcation between lithologic changes. The five Modified Fischer Plot steps are the same steps used by Hurley (1996).

In this dissertation, the bed boundaries generated from the bed boundary picking algorithm were used to create five Modified Fischer Plots (Figures 3.8, 3.9, 3.10, 3.11, 3.12). Modified Fischer Plots were generated using the bed boundary results from each of the tested thresholds. The tested thresholds were 10, 30, 50, 70, and 100.

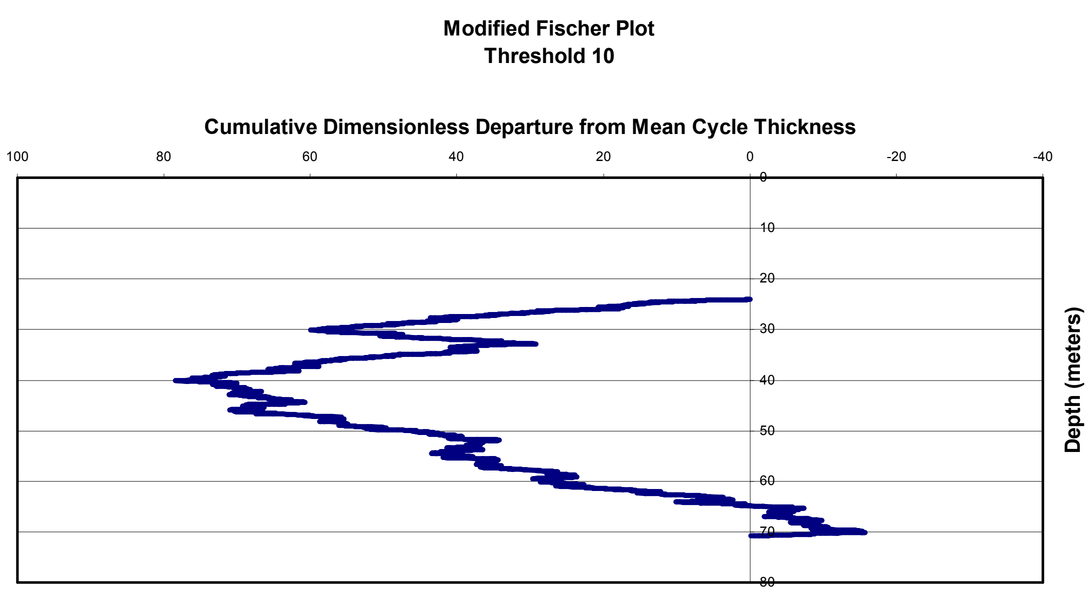

Figure 3.8. Modified Fischer Plot using bed boundaries for threshold 10. The cumulative dimensionless departure from mean cycle thickness is plotted on the x-axis and the depth is plotted on the y-axis.

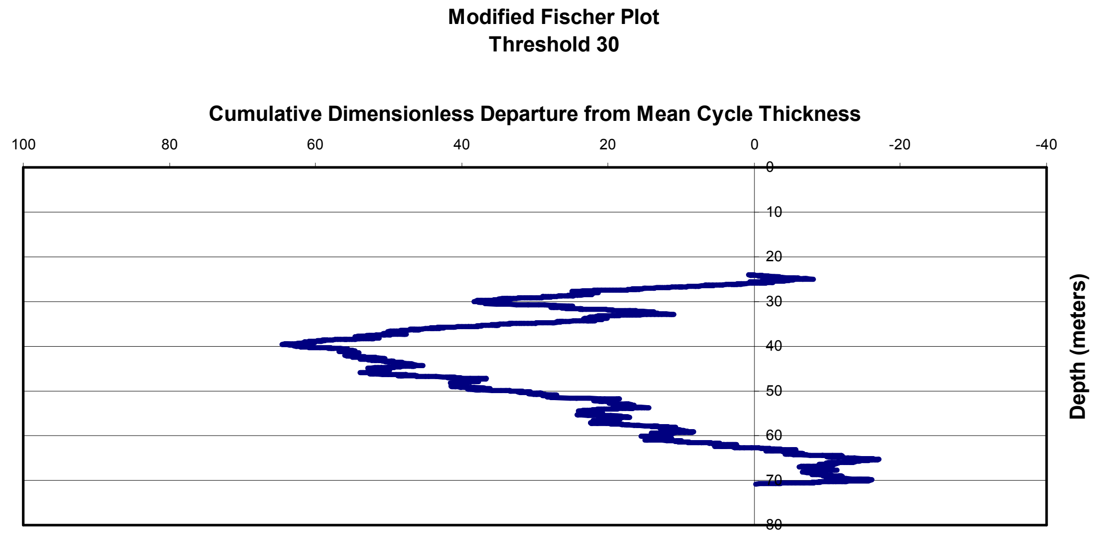

Figure 3.9. Modified Fischer Plot using bed boundaries for threshold 30. The cumulative dimensionless departure from mean cycle thickness is plotted on the x-axis and the depth is plotted on the y-axis.

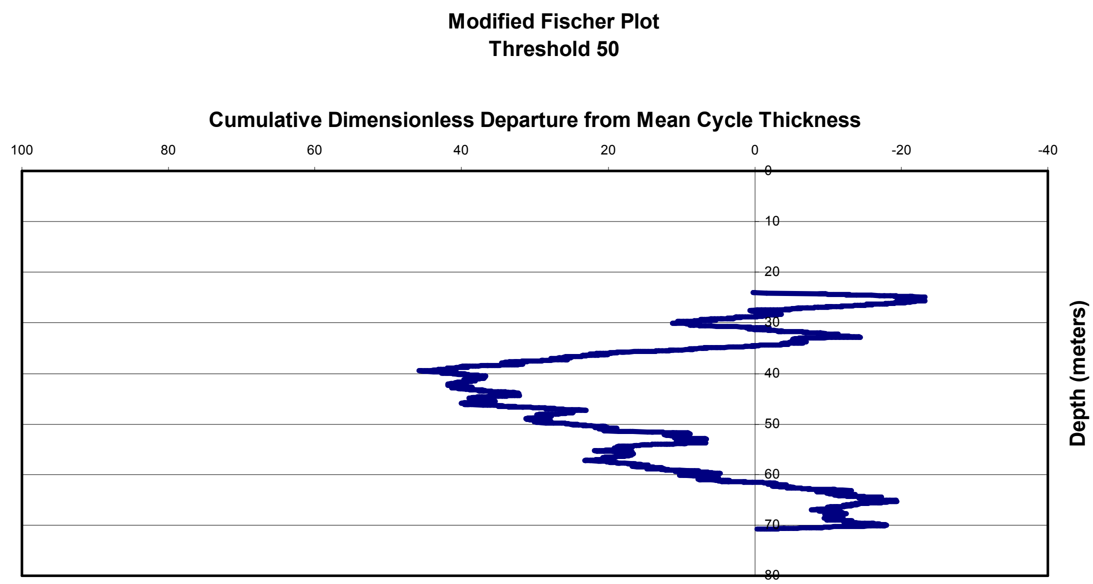

Figure 3.10. Modified Fischer Plot using bed boundaries for threshold 50. The cumulative dimensionless departure from mean cycle thickness is plotted on the x-axis and the depth is plotted on the y-axis.

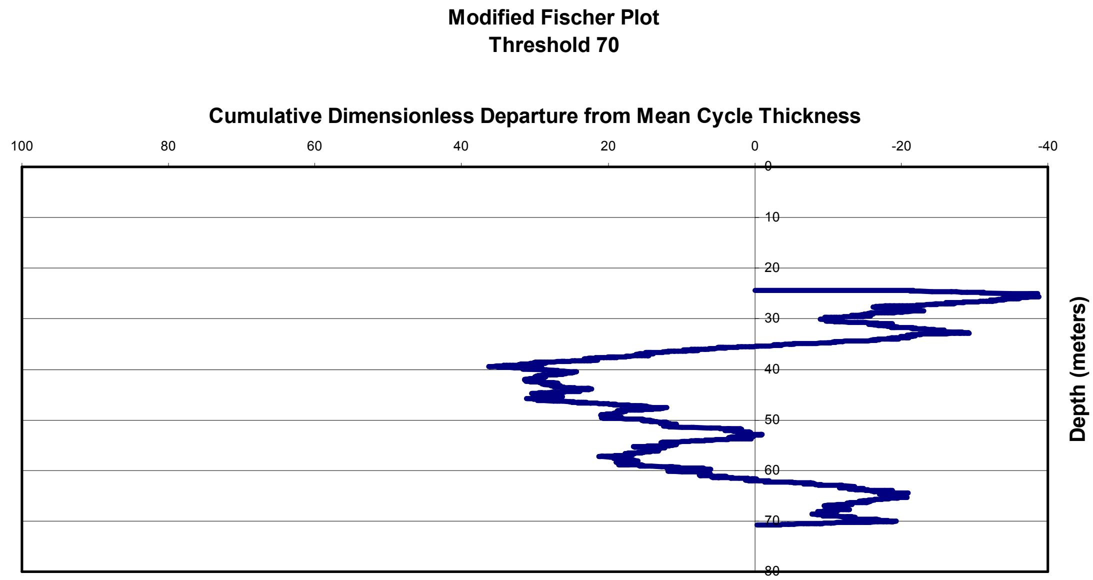

Figure 3.11. Modified Fischer Plot using bed boundaries for threshold 70. The cumulative dimensionless departure from mean cycle thickness is plotted on the x-axis and the depth is plotted on the y-axis.

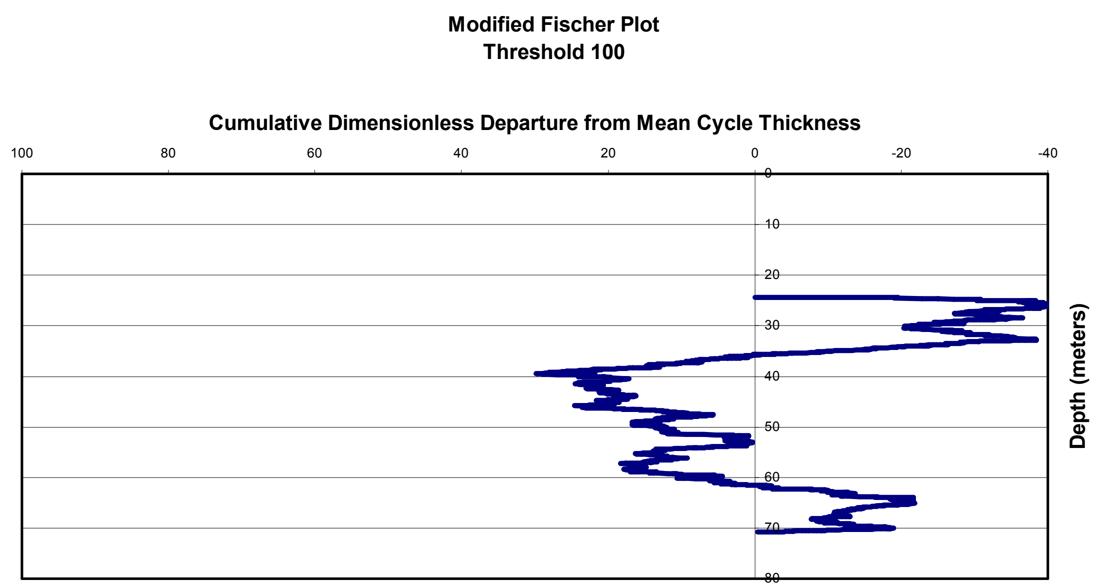

Figure 3.12. Modified Fischer Plot using bed boundaries for threshold 100. The cumulative dimensionless departure from mean cycle thickness is plotted on the x-axis and the depth is plotted on the y-axis.

The Modified Fischer Plots for the thresholds varied in the results. The Modified Fischer Plot for threshold 10 closely resembles the Modified Fischer Plot Spang created manually (Figure 3.13). The other Modified Fischer Plots created using higher threshold values showed different results and did not closely resemble Spang's Modified Fischer Plot. These results require development of a technique that would eliminate the threshold effect that would allow this technique to be used in other wells where the resistivity values may not be comparable for a variety of environmental or lithological reasons (ie, changes in drilling mud, borehole conditions, shale conductivity, etc).

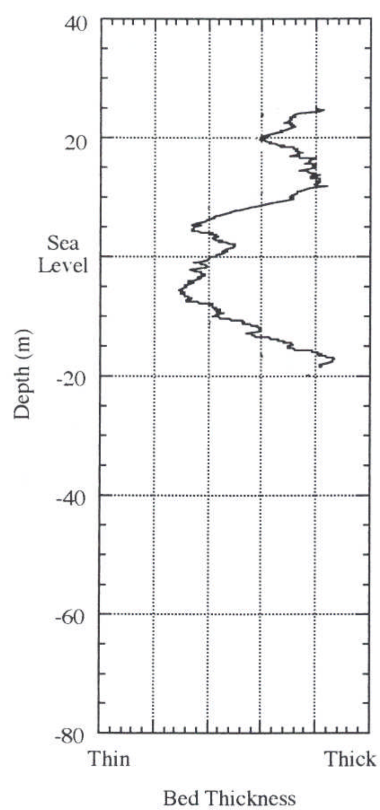

Figure 3.13. Modified Fischer Plot from Spang 2000.

ADJUSTED MEAN THICKNESS AND STANDARD DEVIATION PLOTS ADJUSTED FOR THRESHOLD

The adjusted mean thickness and adjusted standard deviation methods were performed in an attempt to estimate a Modified Fischer Plot that was not subject to thresholds. The thickness values for each threshold were used as inputs for each method. Both of these methods require the use of a sliding window. The size of the sliding window was set to the wavelength of the seismic, 13.3299 meters.

The value of 13.3299 meters was chosen since this represents a wavelength of the 150-hertz high-resolution seismic data acquired along the beach. The 13.3299 meters was calculated by using the equation:

$$V = f\lambda \tag{3.2}$$

where V = seismic velocity, f = frequency of the seismic data, and λ = wavelength of the seismic data. This resulted in a series of windowed mean thickness values for each threshold.

The seismic velocity of the uppermost 100 milliseconds is 2000 m/s (Spang 2000). The frequency of the high-resolution seismic data is 150 hertz. Thus, by using equation 3.2 the wavelength of the seismic data is 13.3299 meters.

After plotting the windowed mean thickness values, a local minimum and maximum value was chosen for each threshold (Figures 3.14, 3.15, 3.16, 3.17, 3.18). The local maximum and minimum values (Table 3.3) for each threshold were plotted on a graph with axes of mean thickness and threshold. Both the maximum and minimum mean thickness values plotted in relatively straight lines indicating there was a linear relationship between threshold and mean thickness (Figure 3.19).

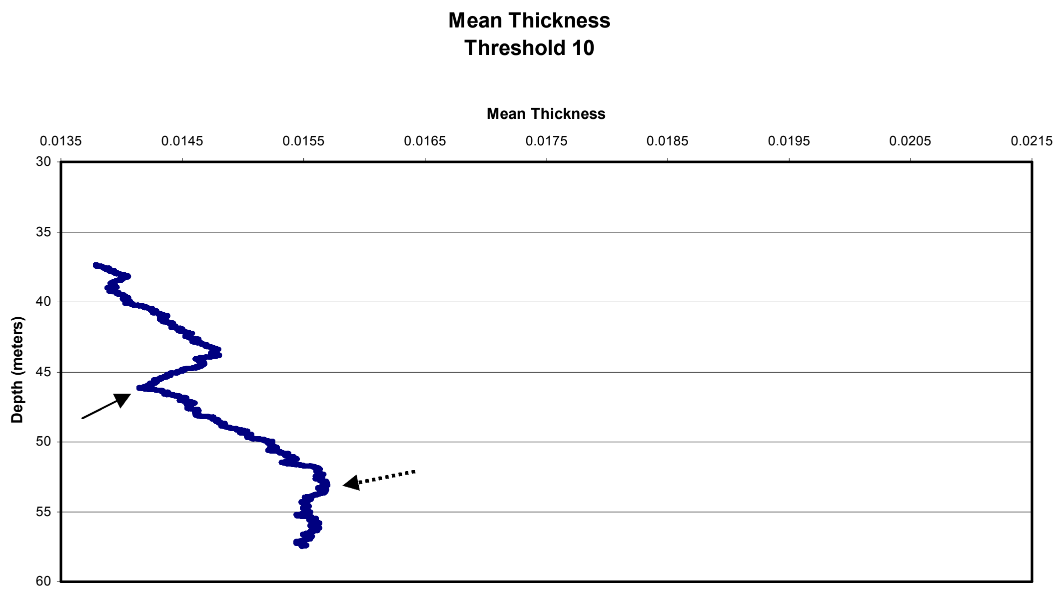

Figure 3.14. Mean thickness plot for threshold 10 illustrating the local minimum (solid arrow) and local maximum (dashed arrow) mean thickness values.

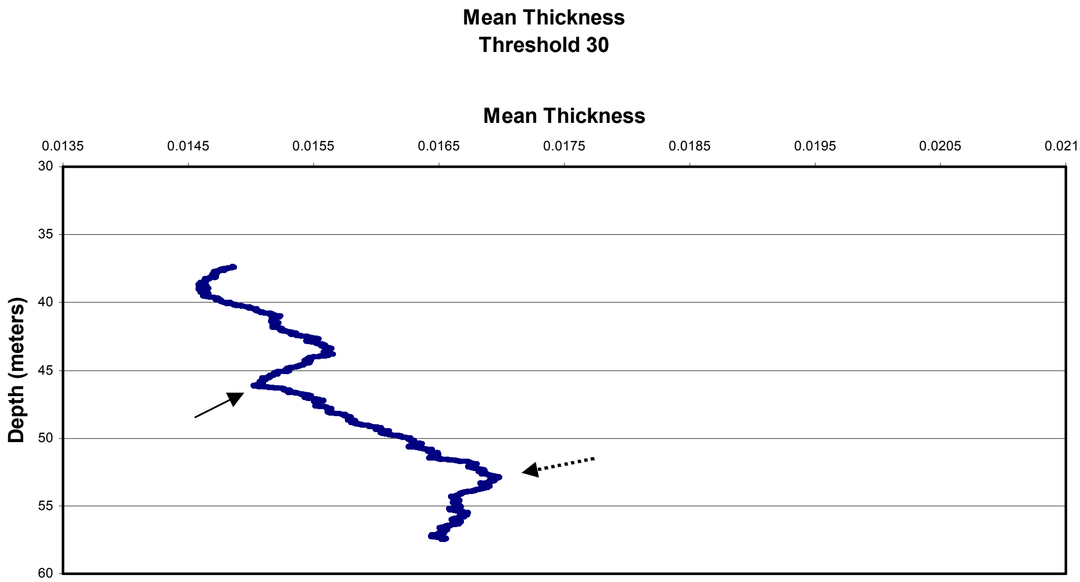

Figure 3.15. Mean thickness plot for threshold 30 illustrating the local minimum (solid arrow) and local maximum (dashed arrow) mean thickness values.

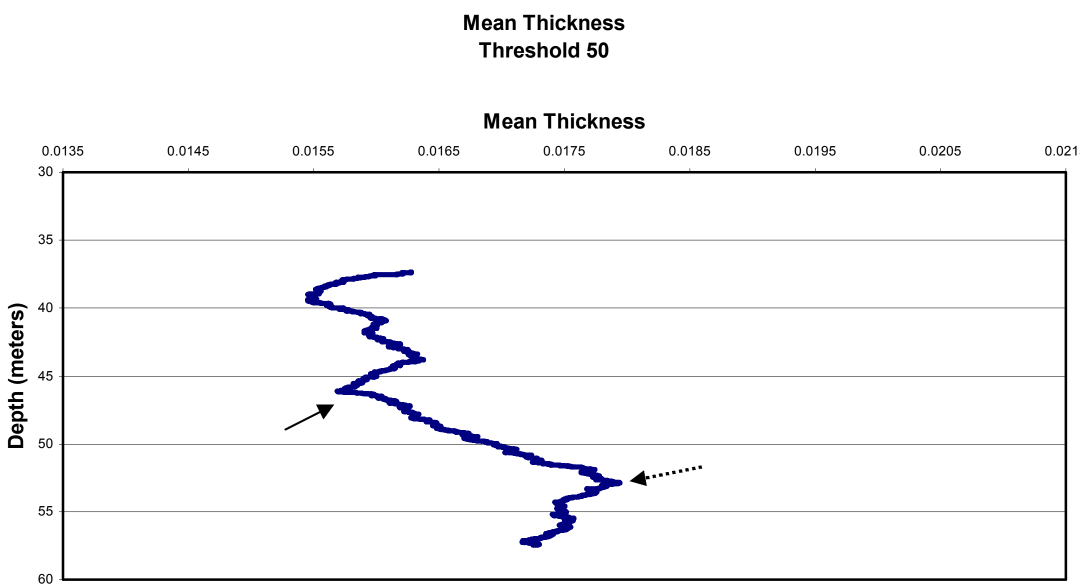

Figure 3.16. Mean thickness plot for threshold 50 illustrating the local minimum (solid arrow) and local maximum (dashed arrow) mean thickness values.

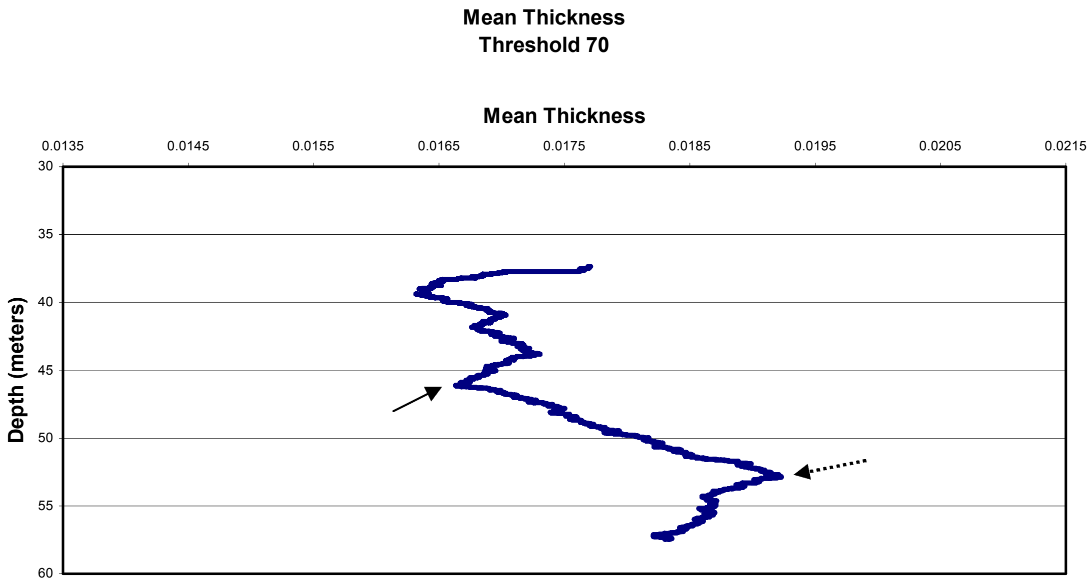

Figure 3.17. Mean thickness plot for threshold 70 illustrating the local minimum (solid arrow) and local maximum (dashed arrow) mean thickness values.

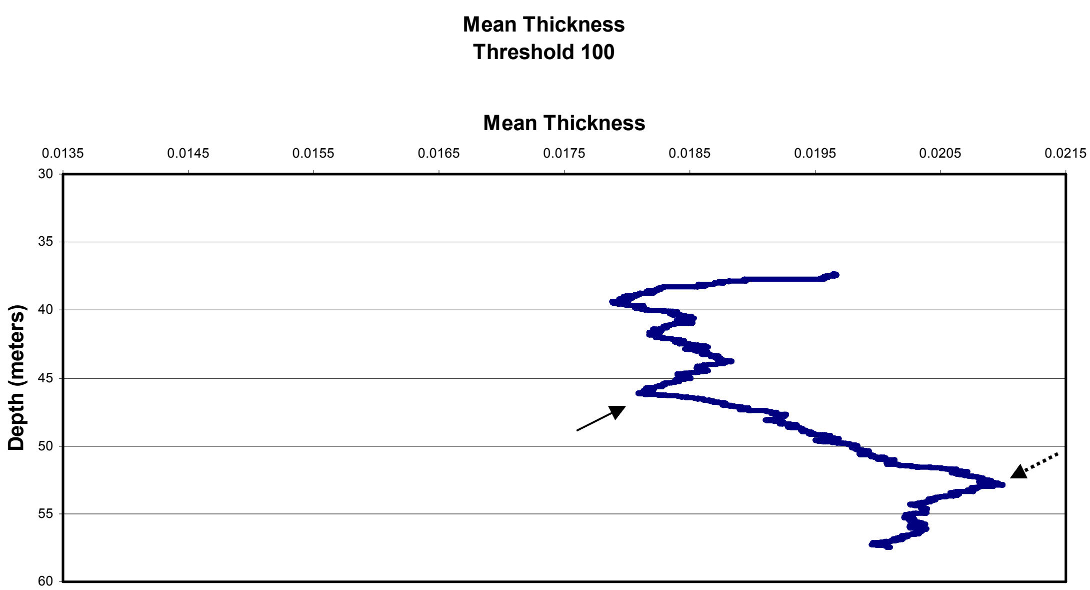

Figure 3.18. Mean thickness plot for threshold 100 illustrating the local minimum (solid arrow) and local maximum (dashed arrow) mean thickness values.

Threshold	Local Minimum Mean Thickness Value (meters)	Depth for Local Minimum Mean Thickness (meters)	Local Maximum Mean Thickness Value (meters)	Depth for Local Maximum Mean Thickness (meters)
10	0.01417619	46.1772	0.015683629	53.4314
30	0.015045251	46.1696	0.016948538	52.9641
50	0.015711902	46.1493	0.017901227	52.9311
70	0.016656835	46.1493	0.019192683	52.9234
100	0.018113003	46.1493	0.020986292	52.8853

Table 3.3. Local minimum and maximum mean thickness values for corresponding thresholds.

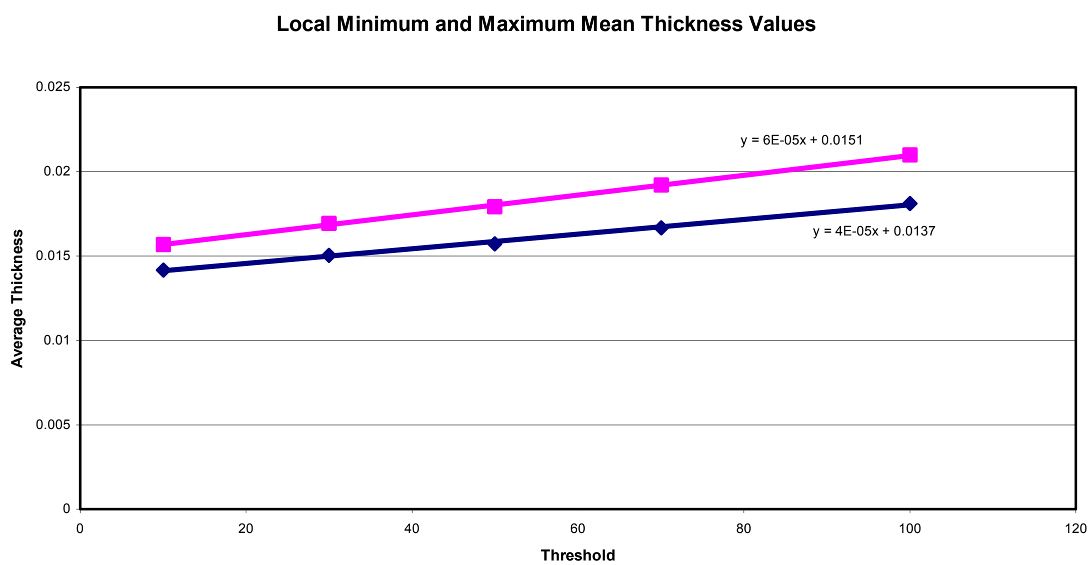

Figure 3.19. Minimum and maximum mean thickness values versus threshold plot. Pink linear trend line indicates maximum mean thickness values and blue linear trend line indicates minimum mean thickness values.

Due to the linear relationship of the local maximum and minimum thickness values, the next step was to extrapolate the mean thickness values back to zero threshold. The lines of best fit with known equations were fit to the minimum and maximum values. These linear equations were used to predict the local minimum and maximum values at the y-axis.

The following equation was used for both the adjusted mean thickness and standard deviation adjusted for threshold techniques by substituting different values for X_t.

$$\frac{Max_0 - X_0}{Max_0 - Min_0} = \frac{Max_t - X_t}{Max_t - Min_t} \tag{3.3}$$

For this equation it is necessary to solve for X_0 where:

$$X_0 = -\{((Max_t - X_t)/(Max_t - Min_t) \times (Max_0 - Min_0)) - Max_0\} \tag{3.4}$$

The following variables are the parameters used for the adjusted mean thickness calculations:

Max_0 = maximum value at the y-intercept for zero threshold
Min_0 = minimum value at the y-intercept for zero threshold
X_t = mean cycle thickness or bed boundary thickness
Max_t = maximum thickness value at particular threshold
Min_t = minimum thickness value at particular threshold
X_0 = mean cycle thickness or bed boundary thickness value adjusted to zero threshold

The first calculation of the equation was to substitute X_t with the mean cycle thickness value for each threshold result. The second substitution was to use bed boundary thickness values for X_t. The recalculated mean cycle thickness and bed boundary thicknesses were used to generate new Modified Fischer Plots for given thresholds (Figures 3.20, 3.21, 3.22, 3.23, 3.24).

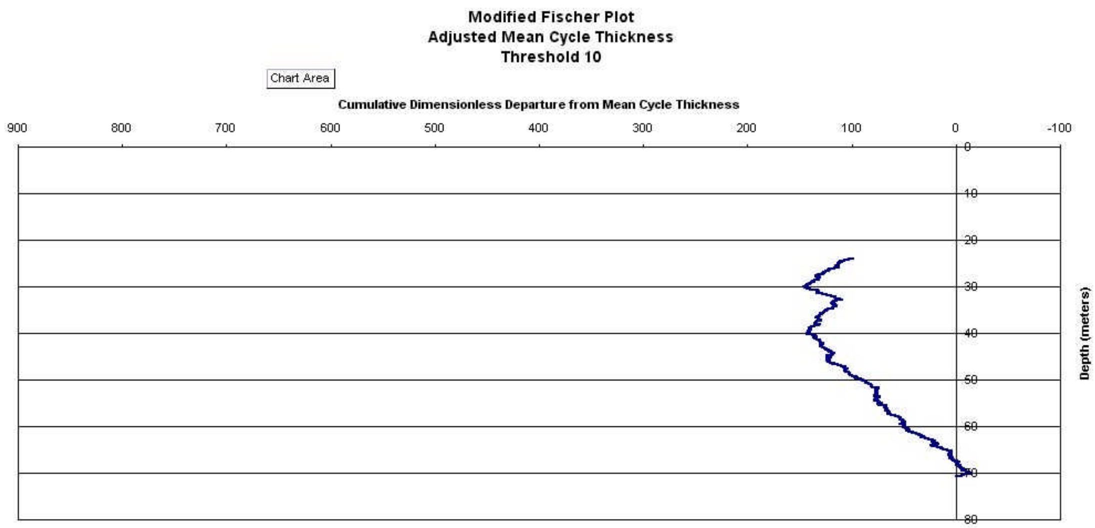

Figure 3.20. Modified Fischer Plot using an adjusted mean cycle thickness for threshold 10.

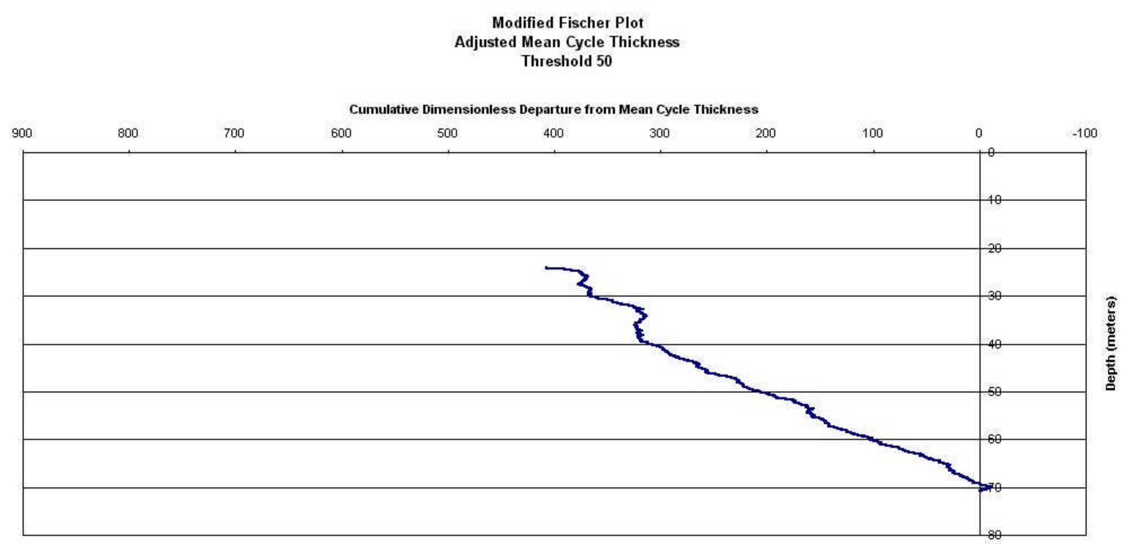

Figure 3.21. Modified Fischer Plot using an adjusted mean cycle thickness for threshold 50.

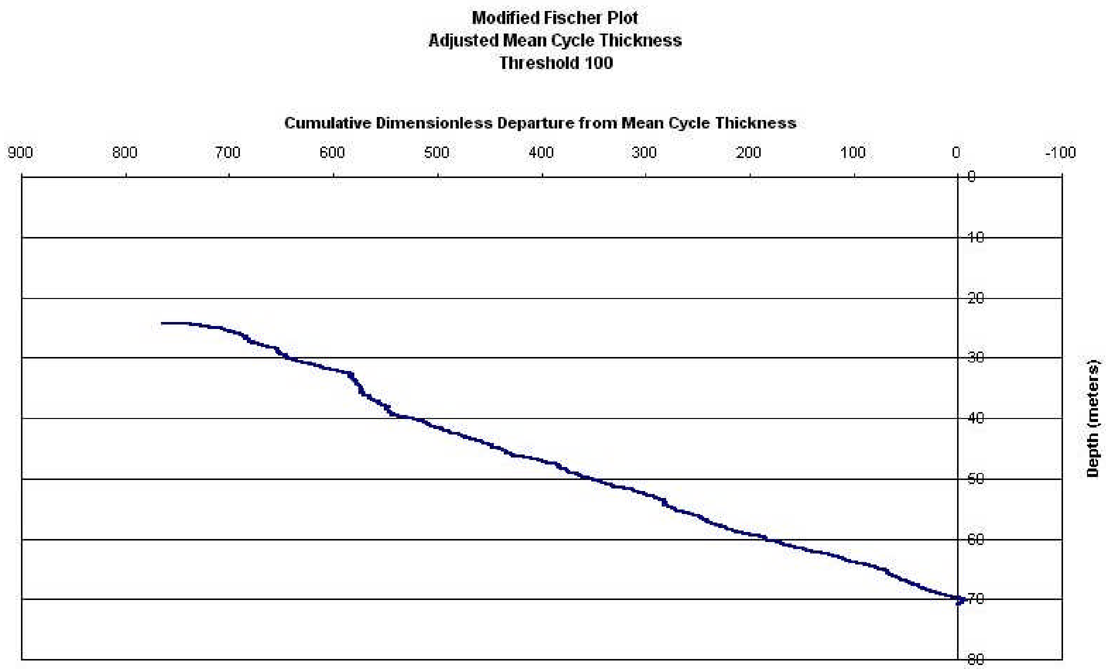

Figure 3.22. Modified Fischer Plot using an adjusted mean cycle thickness for threshold 100.

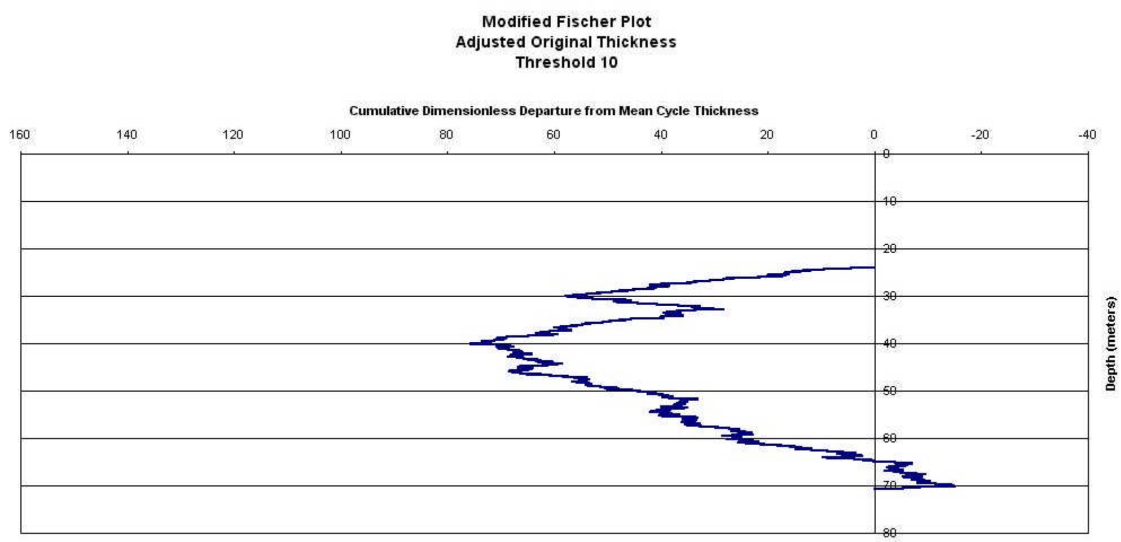

Figure 3.23. Modified Fischer Plot using adjusted bed boundary thicknesses for threshold 10.

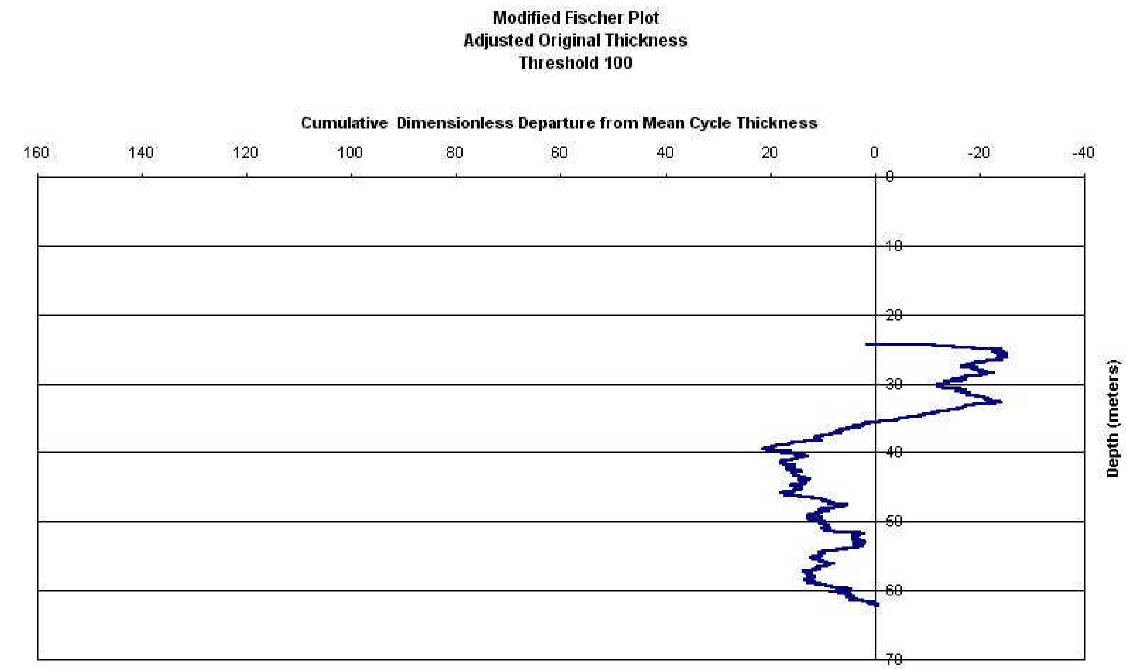

Figure 3.24. Modified Fischer Plot using adjusted bed boundary thicknesses for threshold 100.

The standard deviation adjusted for threshold technique substituted bed boundary thicknesses for X_t (Figures 3.25, 3.26, 3.27, 3.28, 3.29). These plots were generated to determine if there was a variation among the standard deviation values for each threshold.

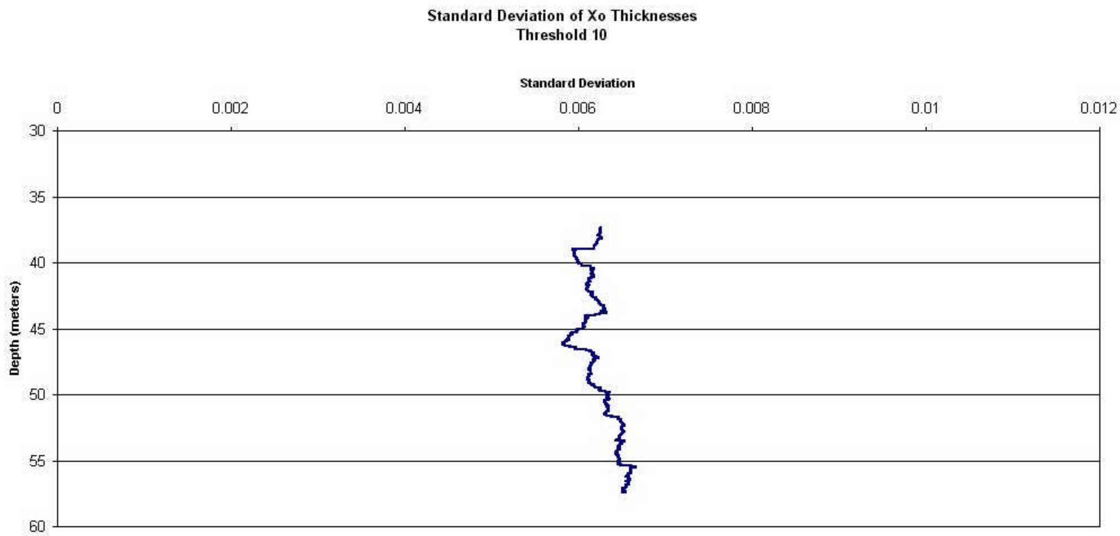

Figure 3.25. Standard deviation plot using adjusted bed boundary thicknesses for threshold 10.

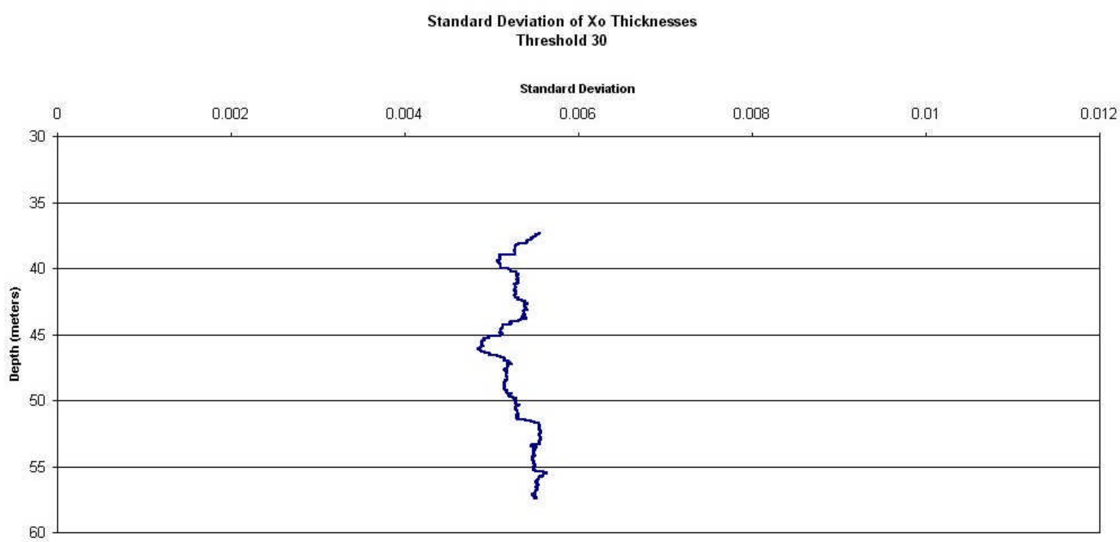

Figure 3.26. Standard deviation plot using adjusted bed boundary thicknesses for threshold 30.

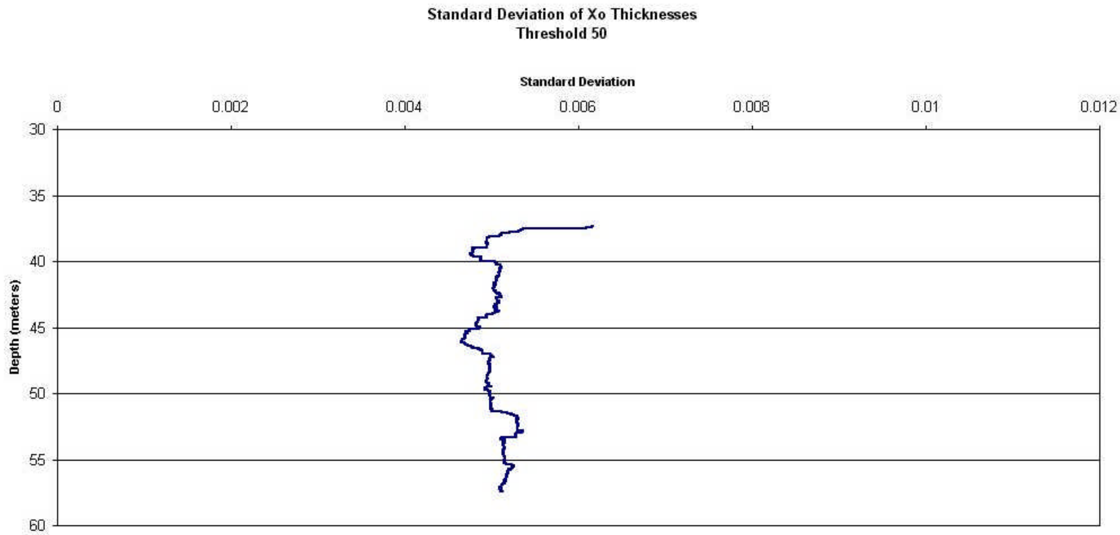

Figure 3.27. Standard deviation plot using adjusted bed boundary thicknesses for threshold 50.

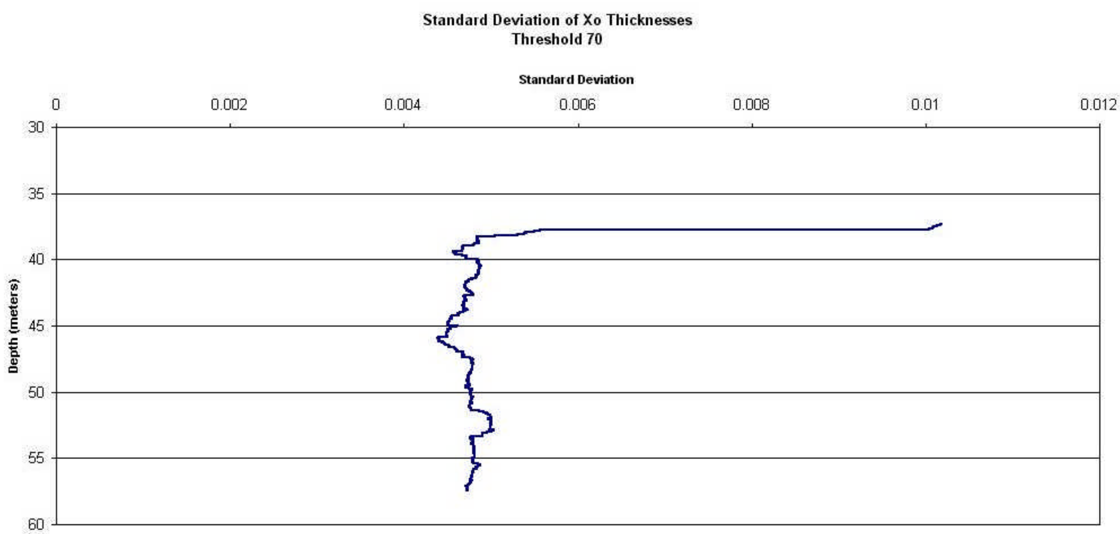

Figure 3.28. Standard deviation plot using adjusted bed boundary thicknesses for threshold 70.

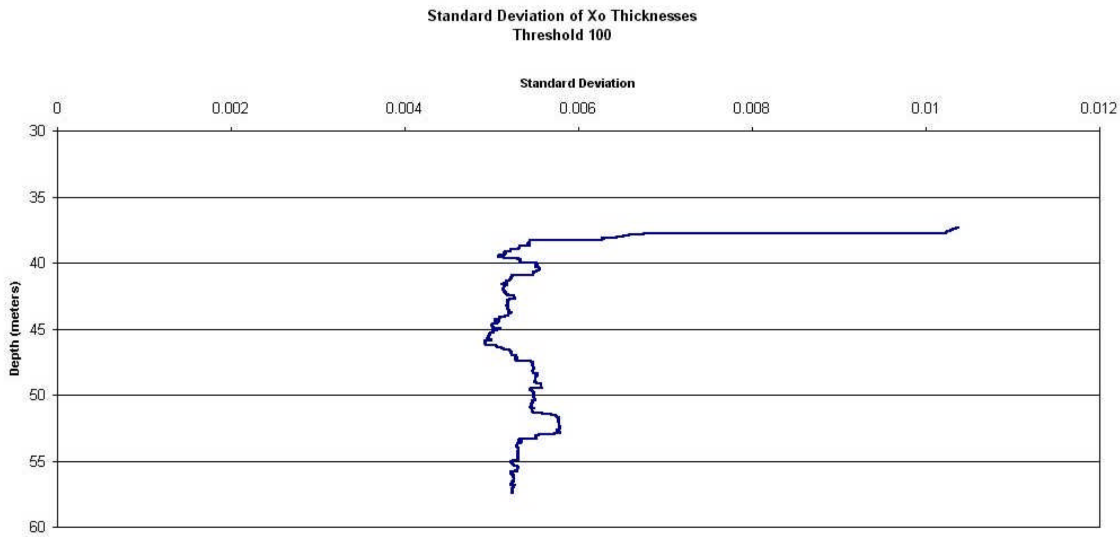

Figure 3.29. Standard deviation plot using adjusted bed boundary thicknesses for threshold 100.

ADJUSTED MEAN THICKNESS AND STANDARD DEVIATION PLOTS ADJUSTED FOR THRESHOLD: RESULTS

The Modified Fischer Plots using recalculated mean cycle thickness values were not similar to the unadjusted Modified Fischer Plots (Figures 3.8, 3.10, 3.12) for each threshold. The Modified Fischer Plots with the recalculated bed boundary thicknesses closely resembled the unadjusted Modified Fischer Plots (Figures 3.8, 3.12) for each threshold. The standard deviation adjusted for threshold plots illustrate that within each threshold, most of the values fell within a given standard deviation.

MODIFIED FISCHER PLOT WITH ZERO THRESHOLD

Because the results of the adjusted mean thickness and adjusted standard deviation did not provide the expected solution, it was necessary to test other means for removing the threshold effect from the Modified Fischer Plots. The technique employed to remove the threshold effect was to rewrite the logic and threshold statements in Excel™. The logic statements were the same logic statements that were used in the bed boundary picking algorithm technique. The logic statements were rewritten to include a zero threshold to analyze the sliding window difference outputs without imposing a threshold. The logic statements analyze each sliding window difference value and evaluate if the value is a bed boundary. Using a zero threshold allowed all of the sliding difference output values to be analyzed. This technique resulted in a Modified Fischer Plot (Figure 3.30) closely resembling Spang's (Figure 3.13).

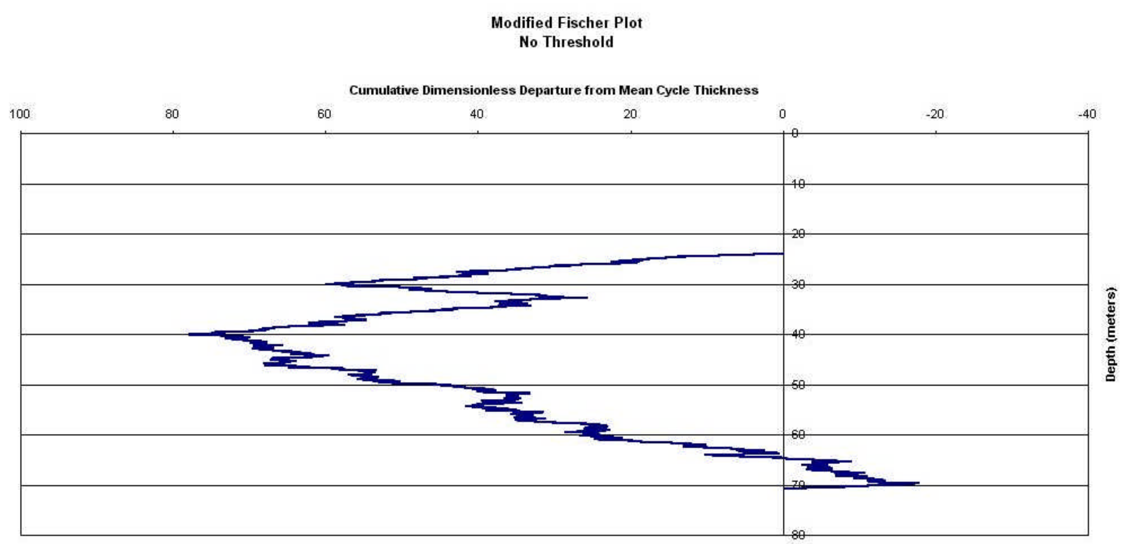

Figure 3.30. Modified Fischer Plot for threshold zero.

SUMMARY OF RESULTS

The sliding windowed difference technique helped to reduce the noise and smooth the microresistivity data. The bed boundary detection algorithm effectively picked bed boundaries. Threshold values were initially used with the bed boundary detection algorithm to further filter the microresistivity data. However, it was determined that bed boundaries could be picked with a threshold of zero.

The final equations used in the bed boundary detection algorithm are the sliding windowed difference (equation 3.1) and a logic tree:

$$\sum_{j=n-1}^{j=n-4} b_j - \sum_{j=n+1}^{j=n+4} b_j \qquad (3.1)$$

The logic tree is:

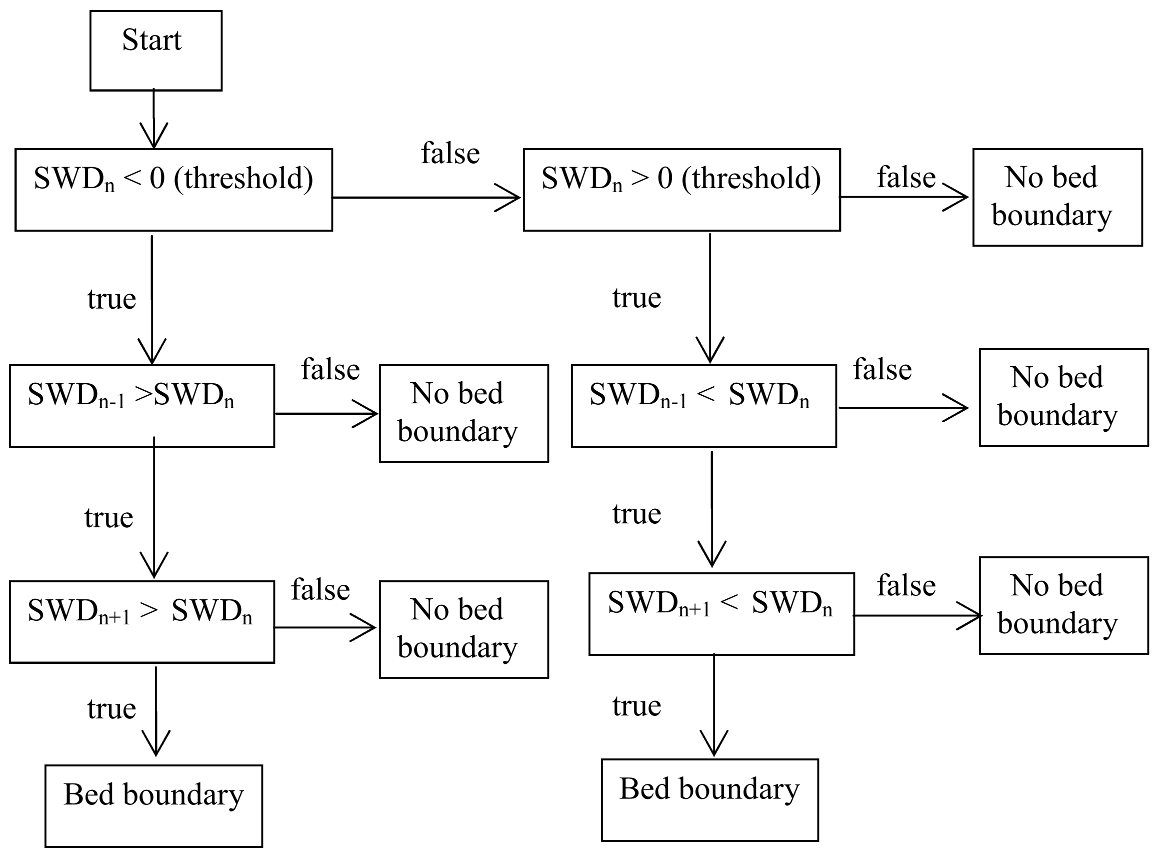

where SWD is the sliding windowed difference result, SWD_n is the sliding windowed difference result at the depth step being investigated, SWD_{n-1} is the sliding windowed difference result above the depth step being investigated, and SWD_{n+1} is the sliding windowed difference below the depth step being investigated.

The automated bed boundary picking technique provides a simple means of upscaling for reservoir geologic modeling. The upscaling process is defined by Stephen et al. (2001) as "grid coarsening, enabled by the calculation of effective flow properties using analytical (e.g., arithmetic, geometric or harmonic averages, streamlines, etc.) and numerical (single- and two-phase flow) simulation." An upscaled reservoir characterization is then used in reservoir simulation modeling. For reservoir characterization, it would be ideal to incorporate all geological and petrophysical data at the scale at which the data are available. However, computing time, costs, and capabilities all limit one's ability to build a data-rich characterization that can be used for reservoir fluid-flow simulation. Therefore, it is necessary to group data into a smaller set of attributes that are intended to portray the most significant aspects of the reservoir.

In this particular instance, bed thicknesses can be automatically grouped in two ways. (1) The Modified Fischer Plots actually provided an upscaled grouping of rock sequences into those with regular bed thickness trends such as thickening- or thinning-upward, or uniform stratigraphic thickness. (2) The ability to change the threshold values for defining a bed boundary provides the second means of upscaling. For example, the threshold value may be set to only record a bed boundary with a major change in resistivity across that boundary. In this case, many beds with only slightly different resistivities bounded on the top and base by beds with large differences in resistivity could be merged into a single bed. An example might be an interval of thin interbeds of coarse silt and fine sand bounded on the top and base by thick, organic rich claystones.

After using the bed boundary detection algorithm results to investigate several geological parameters, the next step in the dissertation research was to use the bed boundary detection algorithm results to investigate a geophysical parameter, anisotropy. The anisotropy analysis was conducted to 1) determine if proximal and distal levee packages could be distinguished using the anisotropic elastic constants and velocities and 2) to determine how thin beds affect anisotropy.

CHAPTER 4. GEOPHYSICAL BOREHOLE IMAGE LOG ANALYSIS

Having characterized the thin-bedding, one can predict seismic anisotropy and thus investigate whether it could be a useful diagnostic tool. This chapter discusses the geophysical methods and results used in the analyses of the borehole image log data in this research, including (1) estimating transverse isotropy and (2) well log spectral analyses. The analyses in this chapter use uncalibrated microresistivity data.

ANISOTROPY

Seismic anisotropy is defined as the variation of seismic velocity depending on either the direction of travel for P- and S- waves or the direction of polarization for S-waves (Sheriff 1991). Seismic waves are used to study the *in situ* physical properties of the Earth's interior.

Seismological methods are based on the theory of elasticity which was in place before scientists discovered that the Earth was a quasi perfect elastic body for short time constants (Babuska and Cara, 1991). The mechanical behavior of a linear elastic material depends on Hooke's law. Hooke's law relates stress (σ_{ij}) to strain (ε_{kl}) (Nye,1957). It is written as:

$$\varepsilon_{kl} = s_{ijkl}\,\sigma_{ij} \quad \text{or} \quad \sigma_{ij} = c_{ijkl}\,\varepsilon_{kl} \qquad (4.1)$$

where i, j, k, and l are tensors, s = elastic compliance constant, and c = elastic stiffness constant.

There are 81 possible elastic constants for both s_{ijkl} and c_{ijkl}. Due to the symmetry of s_{ijkl} and c_{ijkl}, there are at most 21 possible independent elastic constants (Nye, 1957). The least possible independent constants are 1 for fluids and 2 for non-fluid isotropic media. The simplest anisotropic case has five independent elastic constants and is referred to as tranverse isotropy or hexagonal symmetry (Thomsen, 1986).

Vertical transverse isotropy is often referred to as anisotropy. Transverse isotropy is one of eight classes of anisotropic symmetry (Crampin, 1986). Transverse isotropy is defined as having an axis of rotational symmetry where the properties are identical for all directions at right angles to the axis (Crampin, 1986).

The five elastic constants for the long-wave equivalent, transversly isotropic medium are (Backus, 1962):

$$\mathrm{L} = \langle 1/\mu \rangle^{-1} \tag{4.2}$$

$$\mathrm{M} = \langle \mu \rangle \tag{4.3}$$

$$\mathrm{R} = \langle \theta/\mu \rangle \tag{4.4}$$

$$\mathrm{S} = \langle \theta * \mu \rangle \tag{4.5}$$

$$\mathrm{T} = \langle \theta \rangle \tag{4.6}$$

$$\text{where } \theta = \mu/(\lambda + 2) \tag{4.7}$$

The $\langle \ \rangle$ indicates an averaging over a given length. For example, if M = $\langle\mu\rangle$, all of the μ values will be averaged over a given length to calculate M.

For a homogeneous transversely isotropic medium to be long-wave equivalent to a stable, layered, isotropic medium with a constant θ, where θ = T, the elastic moduli constants L, M, R, S, and T, must meet the following critierion (Backus, 1962):

$$L \geq 0, \ M \geq 0, \ R \geq 0, \ \tfrac{3}{4} M \geq S \tag{4.8}$$

$$RL = T, \ S = TM, \ 0 \leq T \leq \tfrac{3}{4}; \ L \leq M \tag{4.9}$$

Layers do not become less effective in generating large-scale anisotropy as they become thinner (Backus 1962). It is possible that layers too thin to be observed by conventional well logs are present and could contribute to the large-scale anisotropy of the crust (Backus 1962).

ESTIMATING TRANSVERSE ISOTROPY

The turbidite represented on the borehole images consist of shales and sandstones. It has been noted in a previous experiment that near-surface shales behave approximately transversely isotropic (Robertson and Corrigan 1983).

The purpose of this part of the research is to investigate anisotropy or transverse isotropy using the Mount Messenger Formation thin-bedded strata. The objectives were 1) to use the microresistivity data to investigate the elastic properties over the length of the log, 2) to determine if anisotropy could be used to distinguish between proximal and distal levee packages, and 3) to determine how thin beds affect anisotropy. Three different experiments were conducted, each using different velocity (Vp and Vs) data, to investigate the effect of thin beds on elastic properties.

First experiment:

The elastic moduli constants were calculated from the borehole image log data and velocity information from previous research (Spang, 2000). The dry P-wave velocities (Vp) for shale and sandstone were reported as measured by Amoco Laboratories (Spang, 2000). The dry measurements were 1.956 km/s for shale and 1.807 km/s for sandstone. To calculate the elastic moduli constants it is necessary to have saturated or wet Vp values. The saturated Vp value used for shale was 2.0 km/s and saturated sandstone Vp was 2.750 km/s. The dry shale measurement was close to the saturated shale Vp values thus a slight adjustment was made regarding the shale Vp value. However, the dry sandstone Vp value was recalculated to obtain a saturated sandstone Vp value by using the Castagna-Greenberg equation. The Castagna-Greenberg equation is:

$$Vp = 1.16 * Vs + 1.36 \qquad \text{km/sec}$$

where Vp is the P-wave velocity and Vs is the S-wave velocity.

Since the dry Vp sandstone value was known, the Vs for the sandstone needed to be calculated using the Castagna-Greenberg equation. From Castagna (1999), Vp versus Vs trend curves for sandstones indicate sandstones have a low Vp/Vs ratio (1.5-1.6). Thus, to calculate the Vs for the saturated sandstone, it was necessary to have the Vp/Vs ratio equal 1.5. Dividing the dry Vp sandstone value (1.807 km/s) by the desired Vp/Vs ratio (1.5), the calculated Vs was 1.205 km/s.

The relationship for Vp and resistivity that was used to calculate the elastic moduli constants was:

$$Vp = a * \log(R) + b \tag{4.10}$$

where a is the slope, R is the resistivity taken from the borehole image log, and b is the value of Vp when the log(R) is zero.

The shale parameters used to solve the equation were: the Vp of shale was 2.0 km/s, the shale conductivity was 1406.280, and the shale resistivity was calculated as 0.000711. The sand parameters used to solve the equation were: the Vp of sandstone was 2.750 km/s, the sandstone conductivity was 24.177, and the sandstone resistivity was calculated as 0.041362. The shale and sandstone resistivities are from the borehole image log data. The conductivity values were the extreme shale and sandstone conductivities. Once the conductivity values were located, the reciprocal of the conductivities provided the resistivity values.

Equation (4.10) was used with the listed shale and sandstone parameters to set up a system of equations. The equations used were:

Shale $$2.0 = a * \log (0.000711) + b \quad (4.11)$$

Sandstone $$2.750 = a * \log (0.041362) + b \quad (4.12)$$

By manipulating these equations and solving for both a and b variables, the resulting equation was:

$$Vp = 0.4249 * \log (R) + 3.3376 \quad (km/s) \quad (4.13)$$

This equation was used to calculate Vp for each depth and the inverse of each was taken.

Five threshold values (10, 30, 50, 70, and 100) were used in the bed boundary detection algorithm (Chapter 3) and the results were used in analyzing the elastic properties. The inverse Vp values were grouped for each bed using the detected bed boundaries from each of the tested thresholds. The average inverse Vp was calculated for each group. The inverse of the average inverse Vp was taken to obtain the average Vp of each group.

Vs was then calculated using the following equation (Castagna et al, 1999):

$$Vs = .770 * Vp - 0.867 \quad (km/s) \quad (4.14)$$

where Vp is the average Vp of each group

To calculate the bulk density for each group, Gardner's equation (Castagna et al., 1999) was used:

$$\rho = 1.741 \ Vp^{.25} \qquad \text{(gm/cc)} \qquad (4.15)$$

To calculate the elastic moduli constants (Backus 1962), the Lame parameters (λ, μ) were essential to know. If Vp, Vs, and density are known, then λ and μ can be calculated using the following formulas:

$$Vp = \left((\lambda + 2 * \mu)/\rho\right)^{1/2} \qquad (4.16)$$

$$Vs = (\mu/\rho)^{1/2} \qquad (4.17)$$

By algebraically manipulating the Vp and Vs equations that contain μ and λ:

$$\mu = \rho * Vs^2 \qquad (4.18)$$

$$\lambda = \rho * Vp^2 - 2\mu \qquad (4.19)$$

where μ and λ are in $g/cm^3 * (km/sec)^2$.

The elastic constants were then calculated for the entire length of the log and plotted on a graph of elastic constants versus threshold (Figure 4.1). In addition, the elastic constants were calculated for both the proximal and distal levee packages (North well) and plotted versus threshold (Figure 4.2 and 4.3).

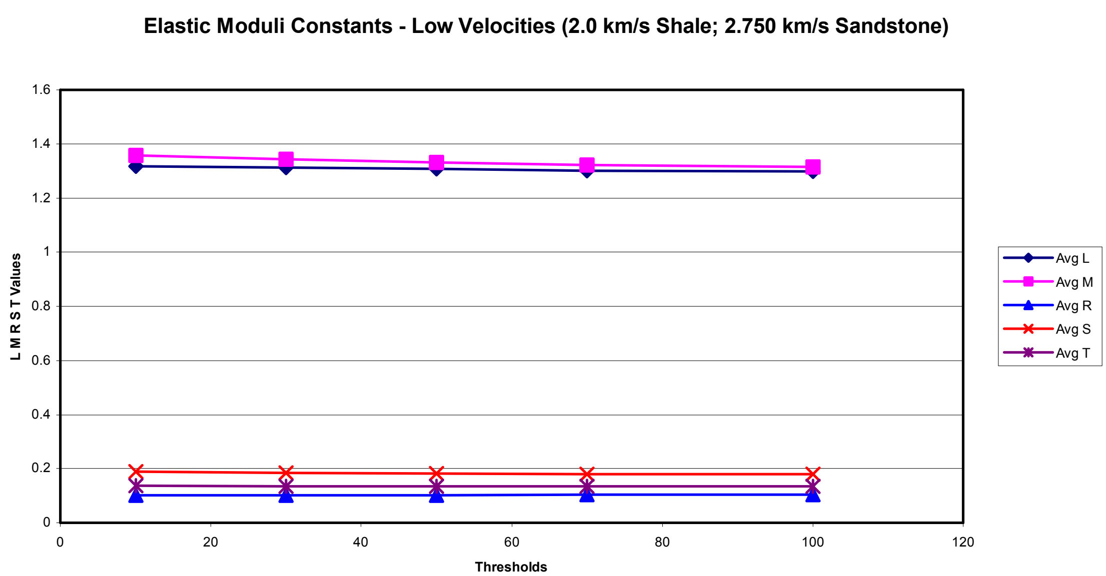

Figure 4.1. Elastic constant results for the entire length of the log for low velocity values. Threshold plotted on the x-axis and elastic constants plotted on the y-axis.

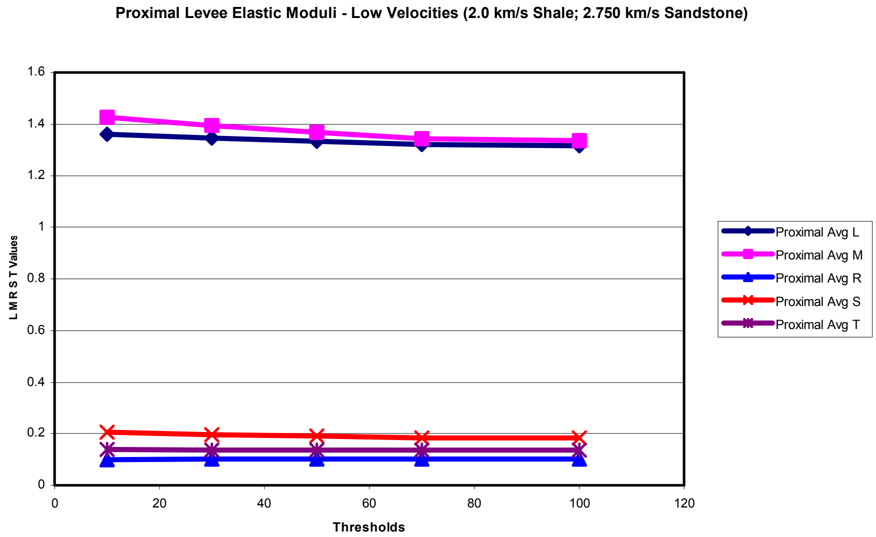

Figure 4.2. Elastic constant results for the proximal levee deposits for low velocity values. Threshold plotted on the x-axis and elastic constants plotted on the y-axis.

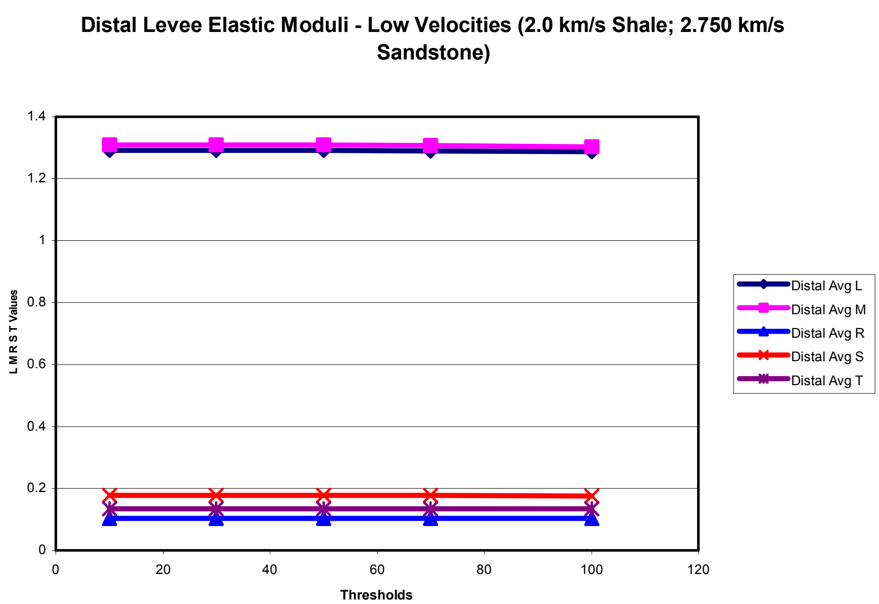

Figure 4.3. Elastic constant results for the distal levee deposits for low velocity values. Threshold plotted on the x-axis and elastic constants plotted on the y-axis.

After the elastic constants were calculated, the P- and S- wave velocities in an effective anisotropic medium were calculated. The formulas are as follows (Mavko et al, 1998):

$$V_{SH,h} = \sqrt{M/\rho} \quad (4.20)$$

$$V_{SH,v} = \sqrt{D/\rho} \quad (4.21)$$

$$V_{P,h} = \sqrt{A/\rho} \quad (4.22)$$

$$V_{P,v} = \sqrt{C/\rho} \quad (4.23)$$

where ρ is the density, $V_{SH,h}$ is the horizontally propagating, horizontally polarized S wave, $V_{SH,v}$ is the horizontally propagating, vertically polarizing S wave, $V_{P,h}$ is the horizontally propagating P wave, and $V_{P,v}$ is the vertically propogating P wave.

M, D, C, and A are:

$$M = \langle \mu \rangle \quad (4.24)$$

$$D = \langle 1/\mu \rangle^{-1} \quad (4.25)$$

$$C = \langle 1/(\lambda + 2 * \mu) \rangle^{-1} \quad (4.26)$$

$$A = \langle 4 * \mu(\lambda + \mu)/(\lambda + 2 * \mu) \rangle + \langle 1/(\lambda + 2 * \mu) \rangle^{-1} * \langle \lambda/(\lambda + 2 * \mu) \rangle^{2} \quad (4.27)$$

The velocity results were plotted versus threshold (Figure 4.4) as well as the proximal and distal levee results (Figure 4.5 and 4.6).

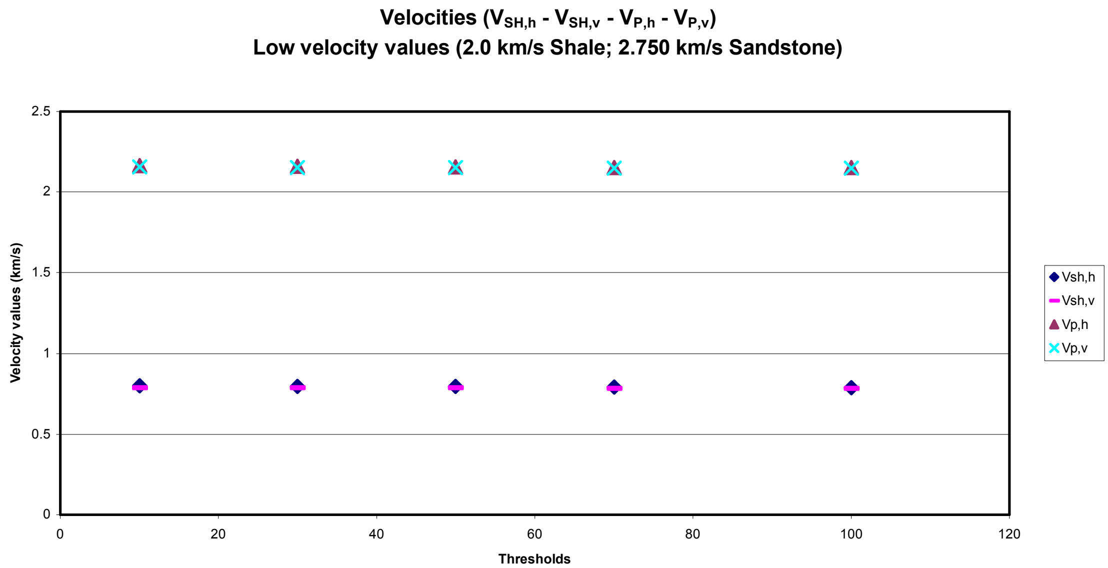

Figure 4.4. Velocity results for the entire length of the log for low velocity values. Threshold plotted on the x-axis and velocity values plotted on the y-axis.

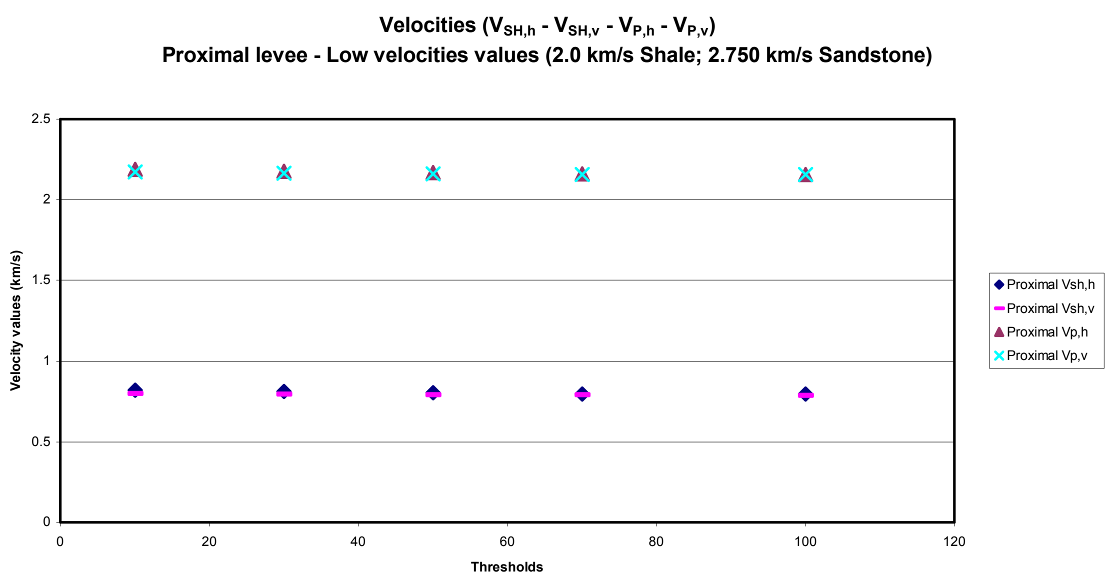

Figure 4.5. Velocity results for the proximal levee deposits for low velocity values. Threshold plotted on the x-axis and velocity values plotted on the y-axis.

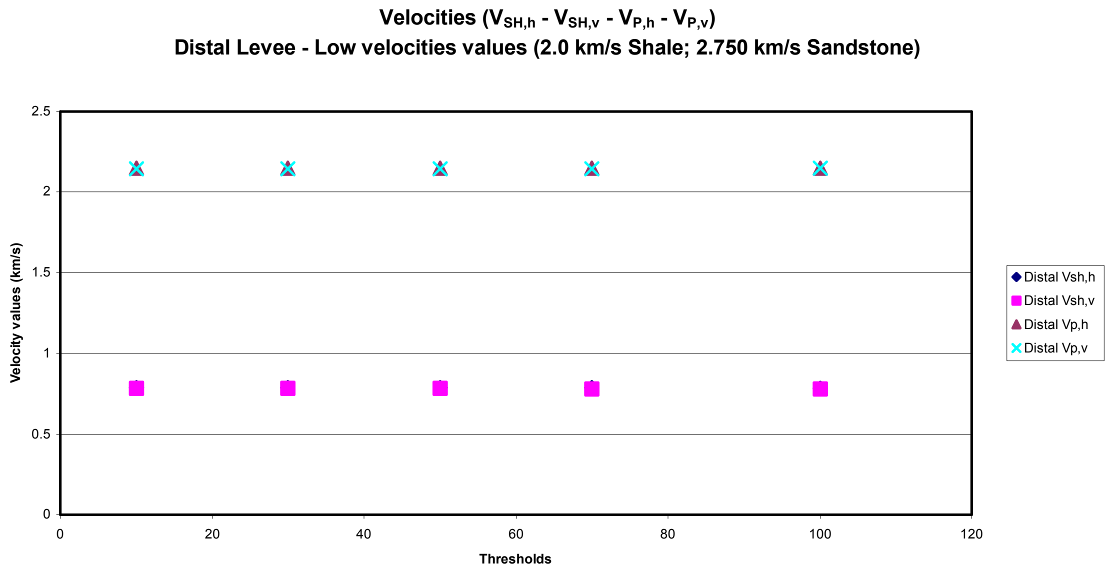

Figure 4.6. Velocity results for the distal levee deposits for low velocity values. Threshold plotted on the x-axis and velocity values plotted on the y-axis.

Second experiment:

The above procedure was repeated with higher velocity values to determine how the higher velocity values would affect the results. The higher velocities were chosen to maximize the difference from the low velocity results. The shale Vp used was 4.0 km/s and the sandstone Vp was 5.5 km/s. These higher velocity values are double the lower velocity values. Using these higher values, equation (4.14) becomes:

$$Vp = .8499 * \log(R) + 6.675 \qquad (km/s) \qquad (4.28)$$

The elastic constants and velocity results from using the higher velocities are shown in Figures 4.7, 4.8, 4.9, 4.10, 4.11, and 4.12.

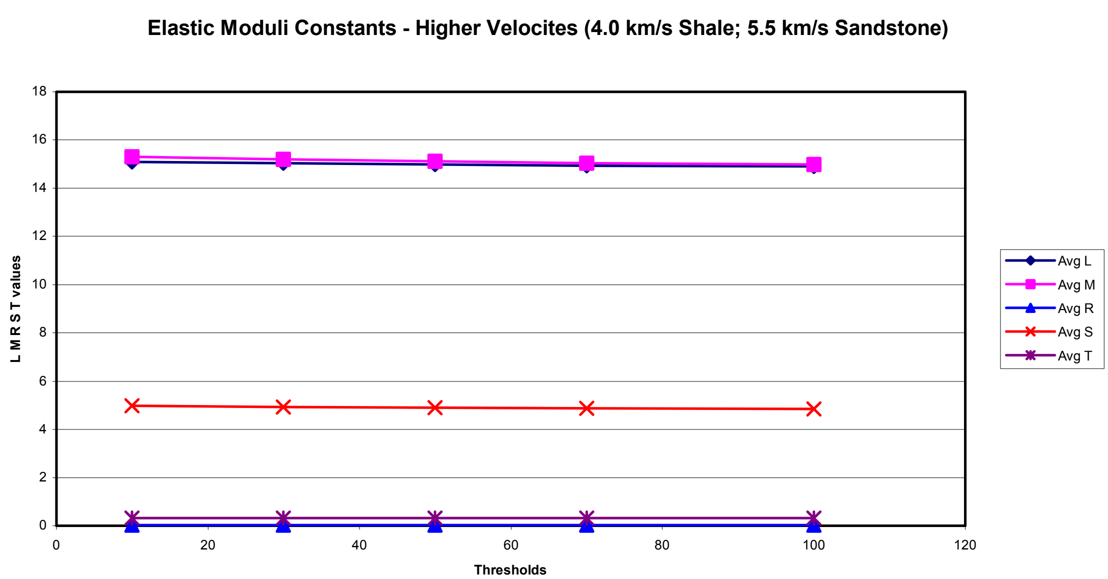

Figure 4.7. Elastic constant results for the entire length of the log for high velocity values. Threshold plotted on the x-axis and elastic constants plotted on the y-axis.

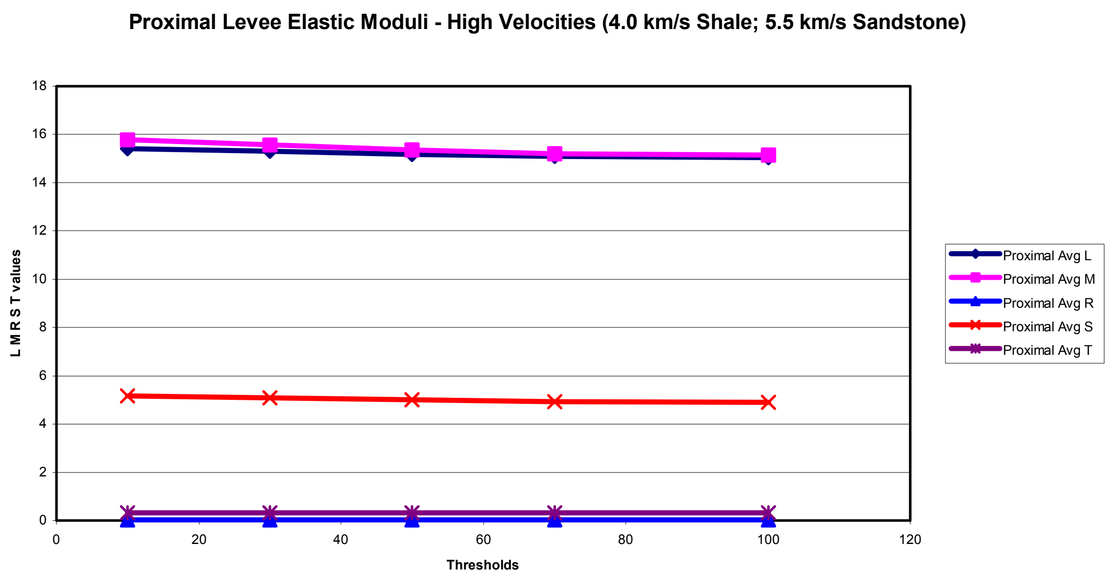

Figure 4.8. Elastic constant results for the proximal levee deposits for high velocity values. Threshold plotted on the x-axis and elastic constants plotted on the y-axis.

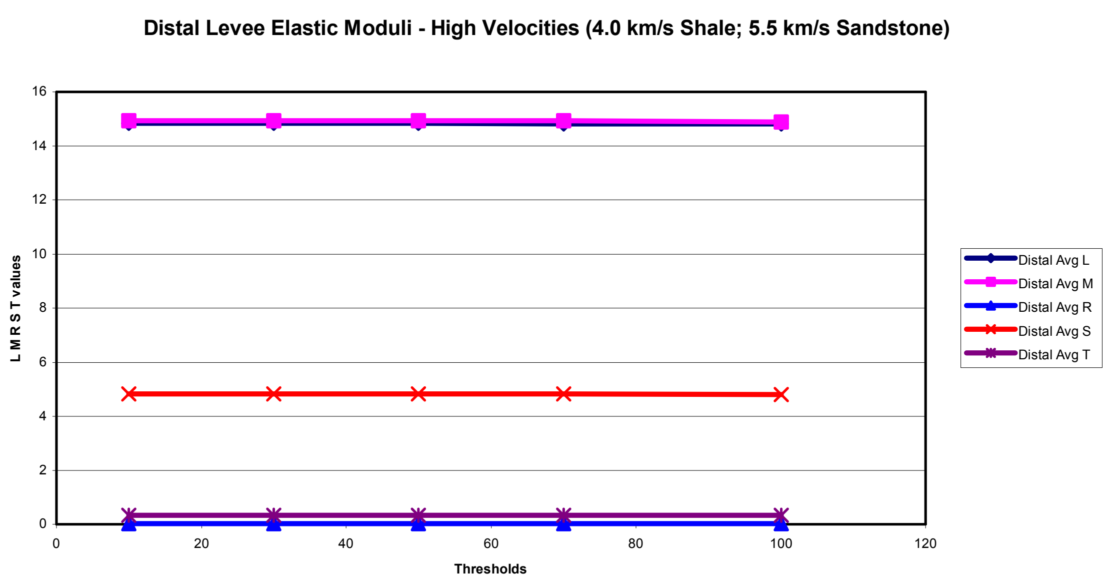

Figure 4.9. Elastic constant results for the distal levee deposits for high velocity values. Threshold plotted on the x-axis and elastic constants plotted on the y-axis.

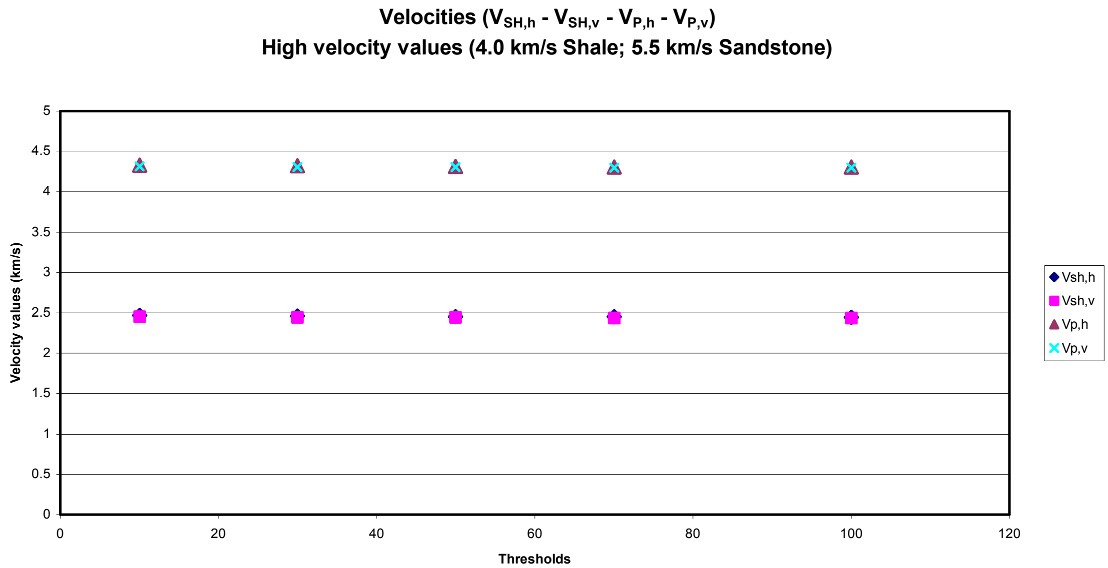

Figure 4.10. Velocity results for the entire length of the log for high velocity values. Threshold plotted on the x-axis and velocity values plotted on the y-axis.

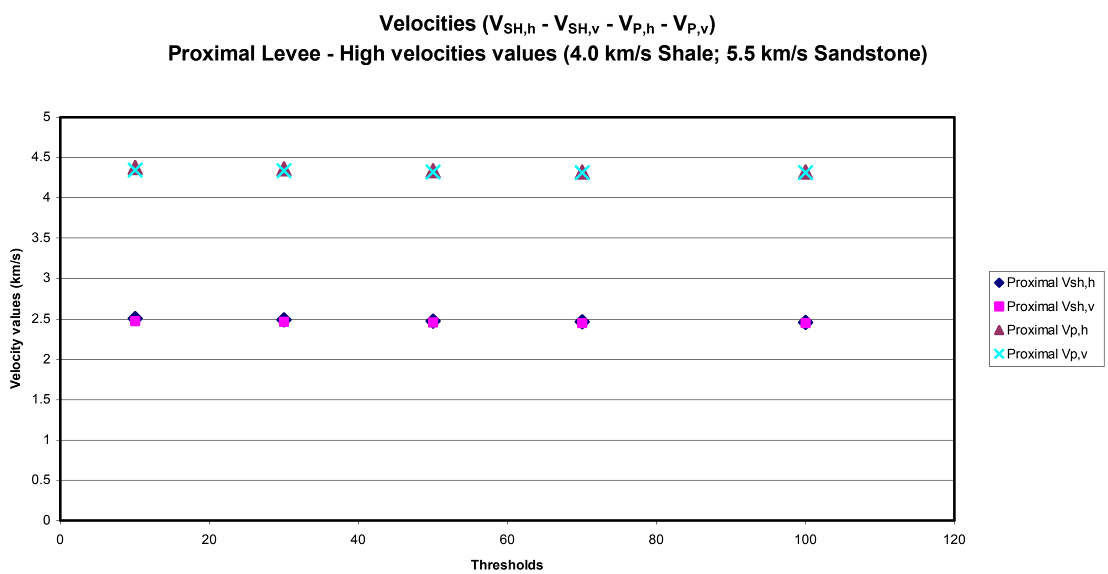

Figure 4.11. Velocity results for the proximal levee deposits for high velocity values. Threshold plotted on the x-axis and velocity values plotted on the y-axis.

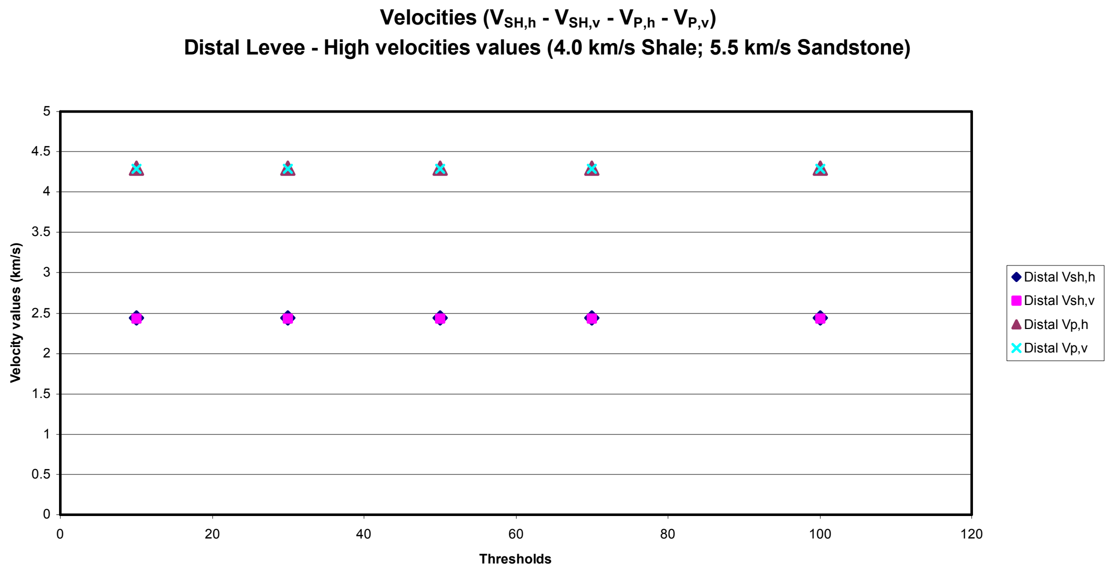

Figure 4.12. Velocity results for the distal levee deposits for high velocity values. Threshold plotted on the x-axis and velocity values plotted on the y-axis.

Third experiment:

There was additional laboratory data containing Vp and Vs values versus effective pressure (Appendix B) that was assimilated to evaluate the elastic constants and velocities from this study area. Vp versus Vs crossplots were generated from the laboratory velocity (m/s) and effective pressure (psi) data (Figures 4.13, 4.14, 4.15, and 4.16) for the dry mudstone, saturated mudstone, dry sandstone, and saturated sandstone. The mudrock (Castagna et al, 1985) and sandstone (Castagna et al, 1999) lines were plotted on the saturated mudstone and sandstone Vp/Vs crossplots, respectively.

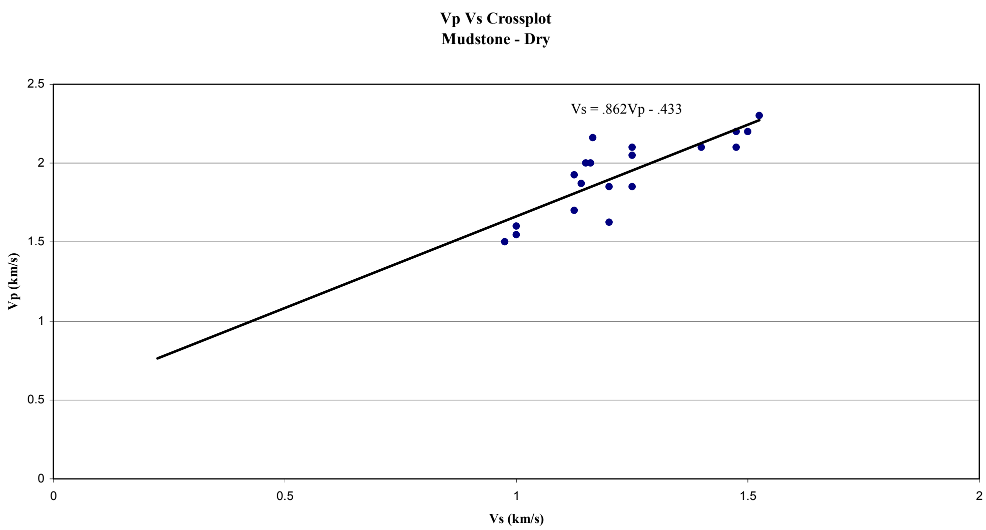

Figure 4.13. Vp Vs crossplot of the dry mudstone samples. The included equation represents the line of best fit. Vs (km/s) is plotted on x-axis and Vp (km/s) is plotted on the y-axis.

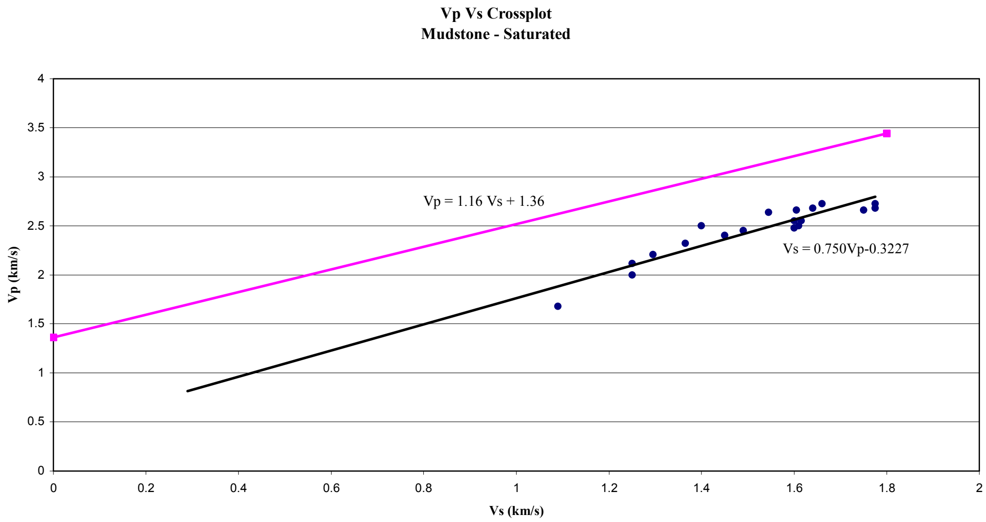

Figure 4.14. Vp Vs crossplot of the saturated mudstone samples. The included equation represents the line of best fit (black line). Equation of mudrock line (Castagna et al, 1985). Vs (km/s) is plotted on x-axis and Vp (km/s) is plotted on the y-axis.

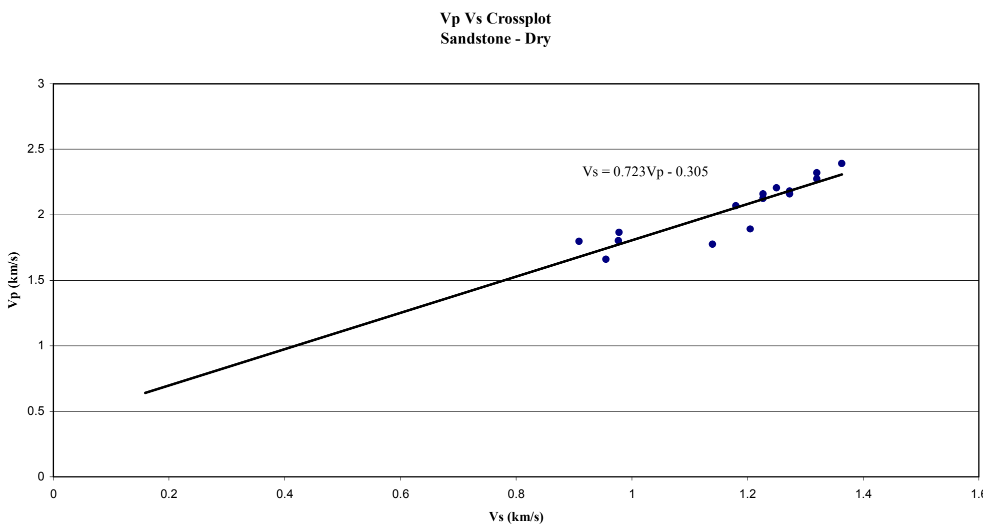

Figure 4.15. Vp Vs crossplot of the dry sandstone samples. The included equation represents the line of best fit. Vs (km/s) is plotted on x-axis and Vp (km/s) is plotted on the y-axis.

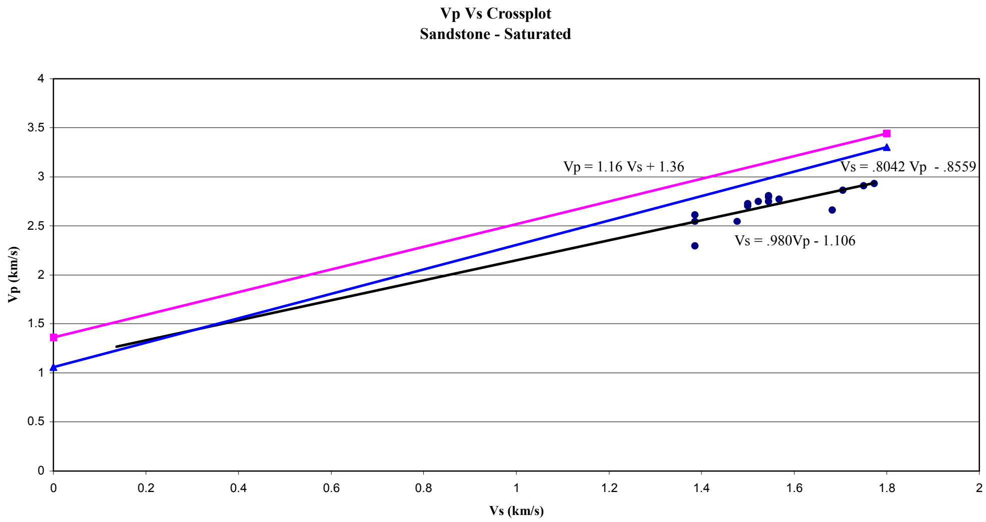

Figure 4.16. Vp Vs crossplot of the saturated sandstone samples. The included equation represents the line of best fit (black line). Equation of mudrock line (Castagna et al, 1985). Equation of sandstone Vp/Vs line is Vs = .8042Vp - .8559 (Castagna et al, 1999). Vs (km/s) is plotted on x-axis and Vp (km/s) is plotted on the y-axis.

The laboratory Vp and Vs data from the saturated mudstone and sandstone (Figures 4.14 and 4.16) fall below the published mudrock and sandstone lines. Some reasons for the difference between the published mudrock and sandstone lines from the laboratory data could be variation in lithology, cementation, composition, and saturation. Castagna et al (1985) report that clean porous brine sands fall slightly below the mudrock line. The authors also state Vp/Vs is less sensitive to variation of clay content than the variation of porosity. Jordan et al (1994) provide petrographical information regarding the Mount Messenger samples. The authors state that the samples are poorly consolidated, silty to very fine-grained, clay-free, moderately well to well-sorted sandstones (lithic arenites to feldspathic litharenites). These rocks have good to excellent porosity (approximately 25% to 30%) due to the absence of cements and matrix clays (Jordan et al, 1994). With this particular data set, amount of cementation, porosity, and composition of the rocks could have caused the difference between the published mudrock and sandstone lines from the laboratory data.

An average Vp value was calculated from both the saturated mudstone and sandstone. The average Vp for the saturated mudstone is 2.45 km/s and the average Vp for the saturated sandstone is 2.71 km/s. Using these values for Vp resulted in the new equation:

$$Vp = .01473 * \log(R) + 2.914 \quad (km/s) \quad (4.29)$$

A line of best fit was used to obtain the relationship between Vp and Vs (Figure 4.17).

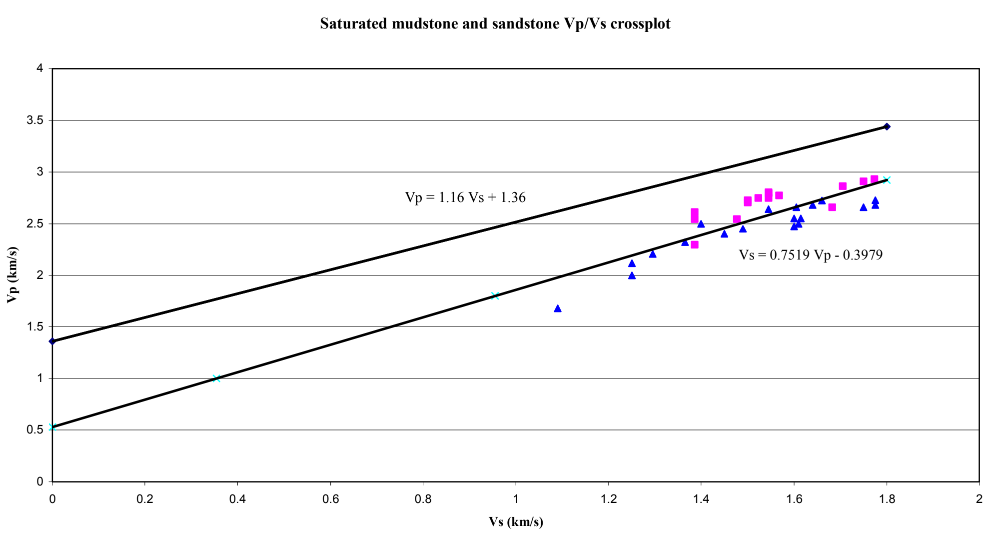

Figure 4.17. Vp Vs crossplot of the satuated mudstone and sandstone samples. The included equation represents the line of best fit. Equation of mudrock line (Castagna et al, 1985). Vs (km/s) is plotted on x-axis and Vp (km/s) is plotted on the y-axis.

The equation for the line of best fit is:

$$Vs = 0.7519 * Vp - 0.3979 \qquad \text{(km/s)} \qquad (4.30)$$

The rest of the calculations were the same as experiments one and two. The results are shown in Figures 4.18, 4.19, 4.20, 4.21, 4.22, and 4.23.

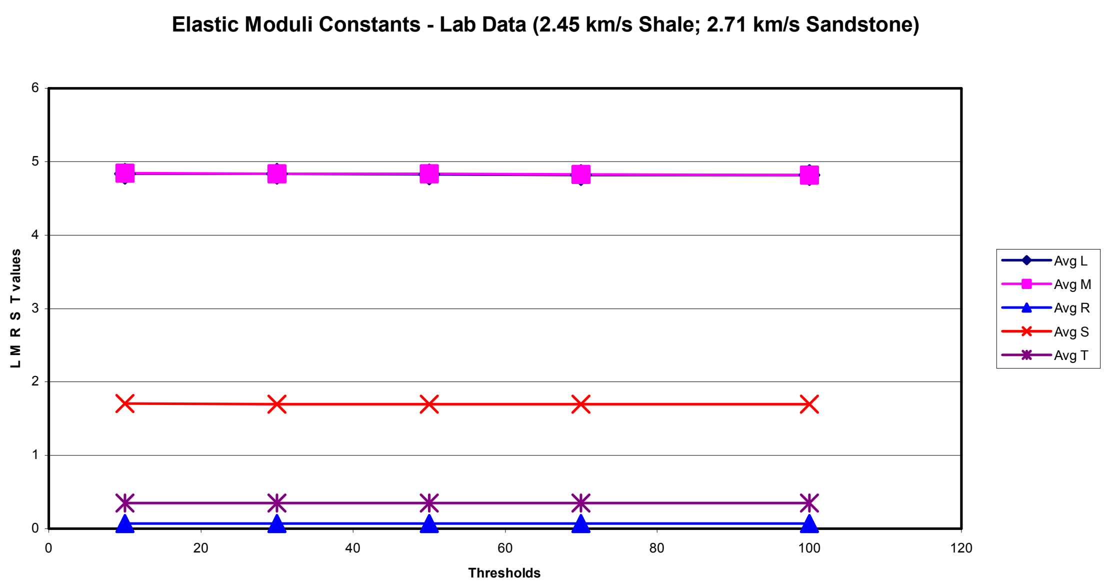

Figure 4.18. Elastic constant results for the entire length of the log for lab velocity values. Threshold plotted on the x-axis and elastic constants plotted on the y-axis.

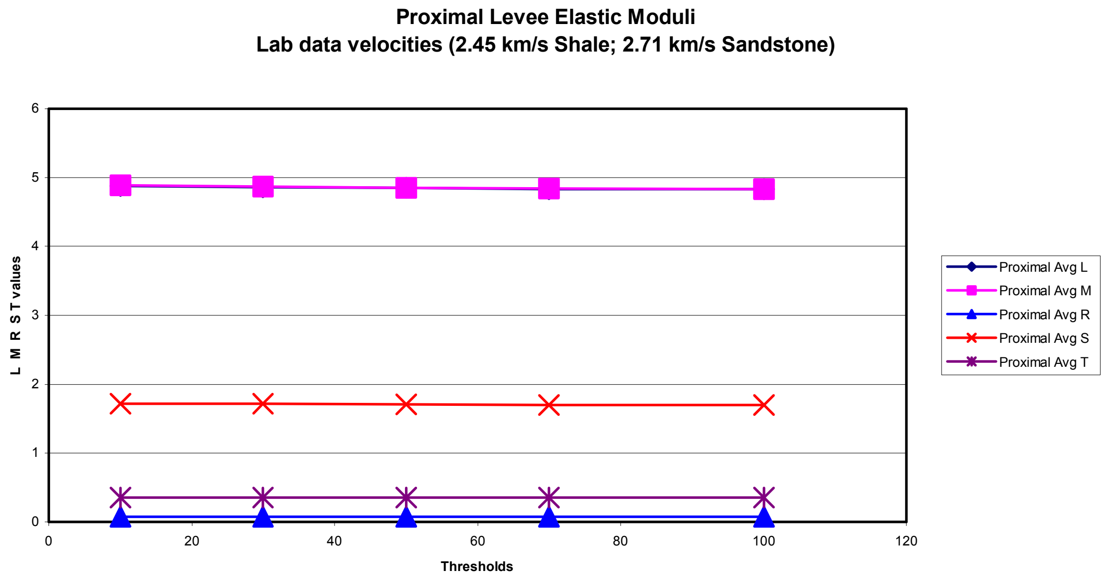

Figure 4.19. Elastic constant results for the proximal levee deposits for lab velocity values. Threshold plotted on the x-axis and elastic constants plotted on the y-axis.

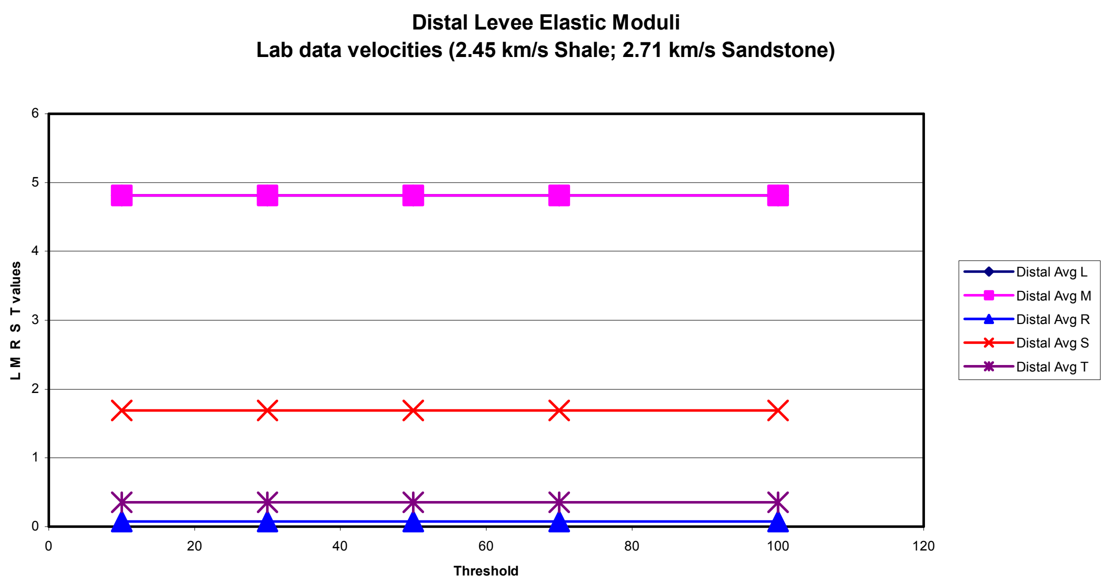

Figure 4.20. Elastic constant results for the distal levee deposits for lab velocity values. Threshold plotted on the x-axis and elastic constants plotted on the y-axis.

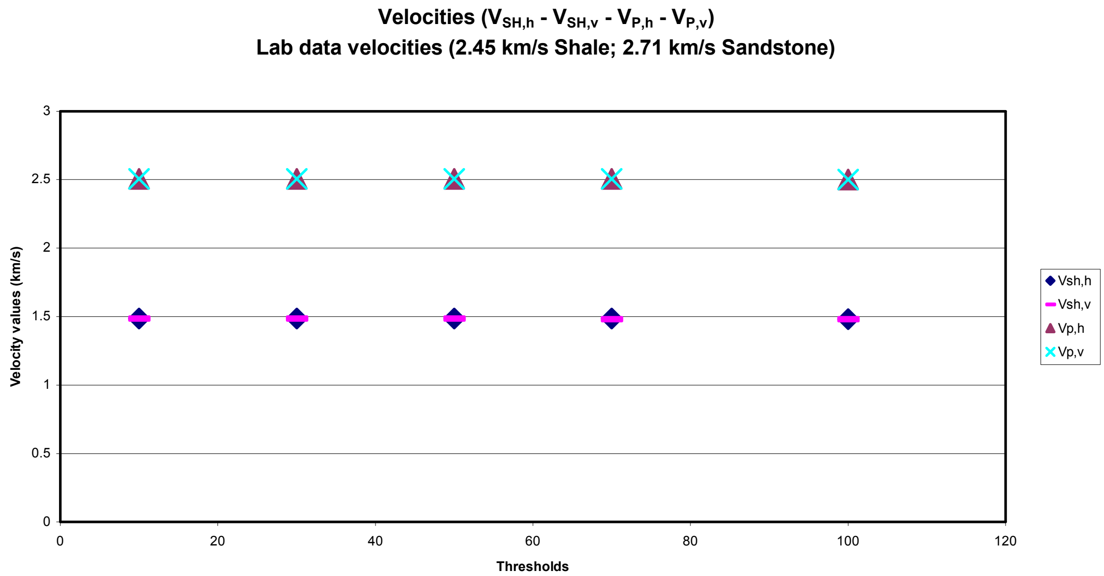

Figure 4.21. Velocity results for the entire length of the log for lab velocity values. Threshold plotted on the x-axis and velocity values plotted on the y-axis.

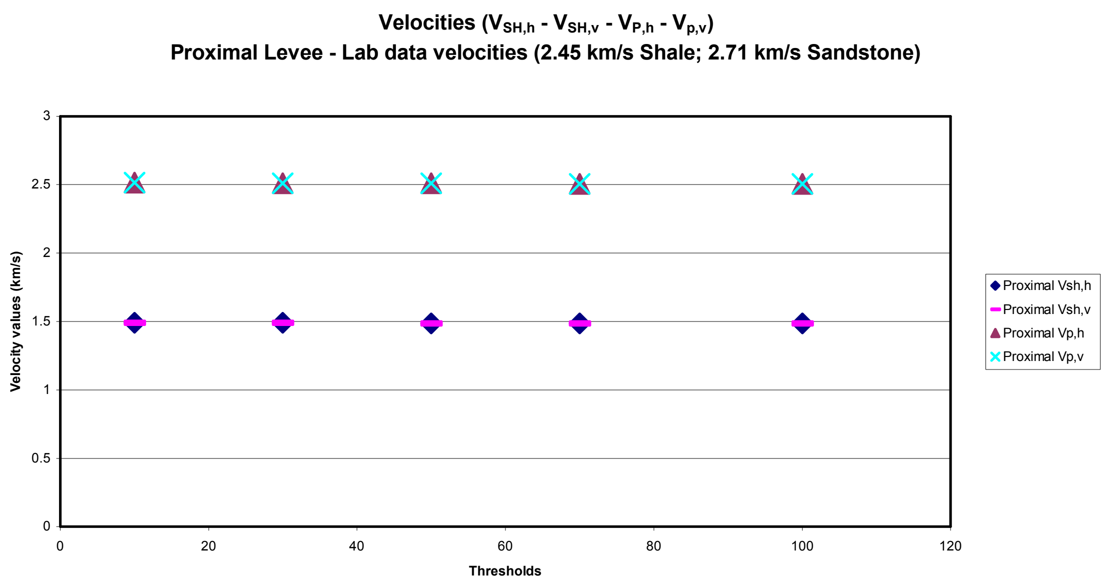

Figure 4.22. Velocity results for the proximal levee deposits for lab velocity values. Threshold plotted on the x-axis and velocity values plotted on the y-axis.

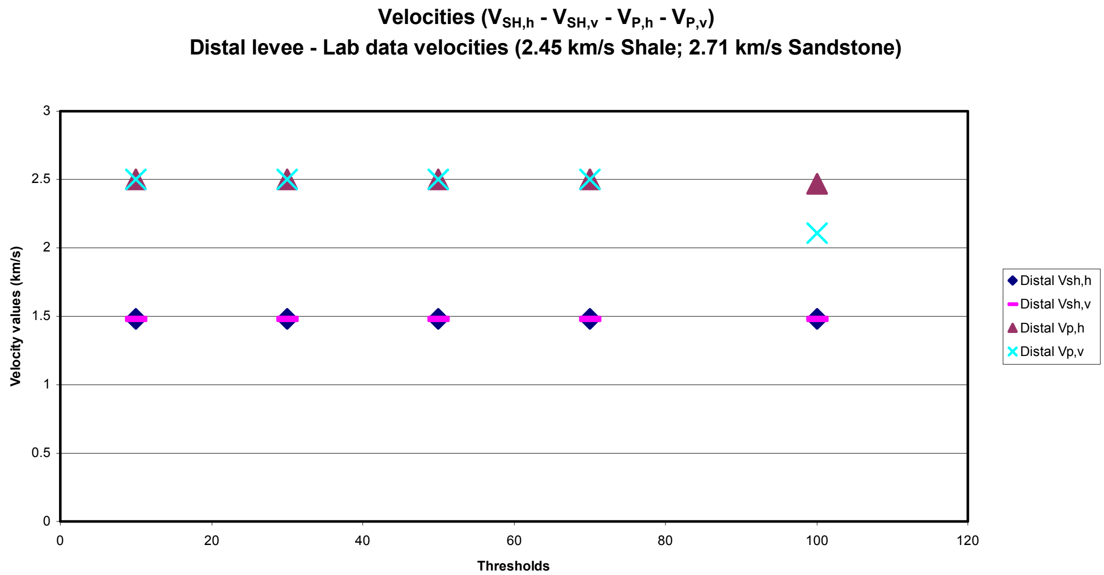

Figure 4.23. Velocity results for the distal levee deposits for lab velocity values. Threshold plotted on the x-axis and velocity values plotted on the y-axis.

ESTIMATING TRANSVERSE ISOTROPY: RESULTS

The elastic moduli constants for the low velocity values show that elastic constants R and T do not change with threshold (Figure 4.1). Elastic constants L, M, and S change slightly across the range of thresholds (2%, 3%, and 5% respectively). The proximal and distal levee (North well) elastic constants R and T do not show a change with threshold (Figures 4.2 and 4.3). The elastic moduli constants L, M, and S exhibit a small change (3%, 6%, and 11% respectively) in the proximal levee deposits, whereas for the distal levee deposits there is no change in these elastic constants. For the $V_{SH,h}$, $V_{SH,v}$, $V_{P,h}$, and $V_{P,v}$ velocity values for the low velocities, there appears to be no change with threshold (Figures 4.4, 4.5, and 4.6).

The elastic moduli constants for the high velocity values exhibit no change for the elastic moduli constant R and T versus threshold (Figure 4.7). The elastic moduli constants L, M, and S change a small percentage (1%, 2%, and 2% respectively) across the range of thresholds. For the proximal levee case, elastic moduli constants L, M, and S vary 2%, 4%, and 5% respectively from the lowest to the highest threshold value and R and T stay constant across the threshold values (Figure 4.8). For the distal levee deposits for the higher velocity values, all of the elastic moduli constants are the same with the threshold value (Figure 4.9). There appears to be no change of the $V_{SH,h}$, $V_{SH,v}$, $V_{P,h}$, and $V_{P,v}$ velocity values for the high velocities with threshold (Figures 4.10, 4.11, and 4.12).

The lab data velocities for the elastic constants exhibit no change in the elastic moduli across the thresholds (Figure 4.18). The proximal levee (North well) deposits show a slight change of 1% across the range of thresholds in L, M, and S but no change in R and T with threshold. The distal levee deposits exhibit no change of elastic moduli constants with threshold. The $V_{SH,h}$, $V_{SH,v}$, $V_{P,h}$, and $V_{P,v}$ velocity values for the entire length of the log and the proximal levee case do not show any signs of change with threshold (Figures 4.21 and 4.22). However, the distal levee case indicates change of the $V_{P,v}$ value at threshold 100 (Figure 4.23).

There was no significant indication that anisotropy analyses could distinguish between proximal and distal levee packages.

Overall, the calculated anisotropy was small. This is a consequence of the overall high Poisson's ratios and the similar Poisson's ratios for sandstones and shales. These results were not expected. In prior literature**,** Backus (1962) states that layers do not become less effective in generating large-scale anisotropy as they become thinner. Backus (1962) also states that it is possible that layers too thin to be observed by conventional well logs are present and could contribute to the large-scale anisotropy of the crust. In this dissertation, the anisotropy of thresholds with known thin beds did not appreciably differ from the anisotropy of thresholds with fewer thin beds. This indicates that the presence of thin beds does not greatly affect anisotropy.

WELL LOG SPECTRAL ANALYSIS

Fourier analysis is widely used in many disciplines. The Fourier Transform breaks a signal or waveform into its sinusoid components with different frequencies that sum to the original waveform (Hoffman, 2004). It uses exponential and complex components (Fourier Transforms, DFTs, and FFTs, 2004). Cooley and Tukey introduced the Fast Fourier Transform in 1965 (Doveton, 1994). The Fast Fourier Transform identifies the complex coefficients of all the wavelengths up to the Nyquist frequency (Doveton, 1994).

PREVIOUS WORK ON CYCLICITY OF LOGS

In previous years researchers have studied the cyclicity of geologic features from log data through various mathematical techniques. Rampino et al. (1999) used Fast Fourier Transform and wavelet time series analysis of the cyclic components from density and natural gamma ray logs along with the carbon-isotopic ratios of bulk samples to study the Permian/Triassic boundary. Wavelet analysis was applied to gamma ray logs, sonic logs, lithology and biostratigraphy data to detect high-frequency cycles, discontinuities, and gradual sediment changes of the Late Albian cyclostratigraphy of the Western Canada sedimentary basin (Prokoph and Agterberg, 1999). Propkoph and Agterberg (2000) applied wavelet analysis to sixteen gamma ray logs from an oil source rock from the Egret Member, offshore eastern Canada. These authors show that wavelet analysis can detect sedimentary cycles and stratigraphic discontinuities. Fast Fourier Transform and discrete Fourier transform were used in deep-water depositional facies to improve stratigraphic well log evaluations and obtain dominant bed-set thickness data (Fillon and Lawless 2002).

FAST FOURIER TRANSFORM ANALYSES

Fast Fourier Transform (FFT) analysis was applied to the microresistivity data. The purpose of testing this technique was to identify potential cycles in the well data and to determine if the FFT analysis would aid in distinguishing between the proximal and distal levee deposits (North well).

There were two different techniques employed to run the FFT analysis. The first technique was to analyze the microresistivity data and the second was to take the reflection coefficient using calculated Vp and ρ values from the microresistivity data. FFT analysis using Microsoft Excel™ requires the number of values in the input data to be a power of two. Because of this limitation, a sample size of 2,048 values was chosen which is equivalent to approximately five meters of microresistivity data. For all of the analyses in this research, the FFT results were broken into the real and imaginary component. The amplitude of the FFT was calculated using:

$$\text{Amplitude} = \sqrt{\left(r_r^{\,2} + r_i^{\,2}\right)} \qquad (4.31)$$

where r_r is the real component of the FFT and r_i is the imaginary component of the FFT. The frequency was calculated using:

$$\text{Spatial Frequency} = (2^{*}\ \text{Nyquist}) / \text{SR} \qquad (4.32)$$

where the Nyquist was 200 cycles/m and SR is the sample rate.

The FFT analysis for the bedding spectra was conducted by taking the FFT of the microresistivity data. Three FFT graphs were plotted from these results. Two graphs are from the proximal levee deposits (Figures 4.24 and 4.25) and one is from the distal levee deposits (Figure 4.26). The FFT analysis graphs plot frequency (x-axis) versus amplitude (y-axis).

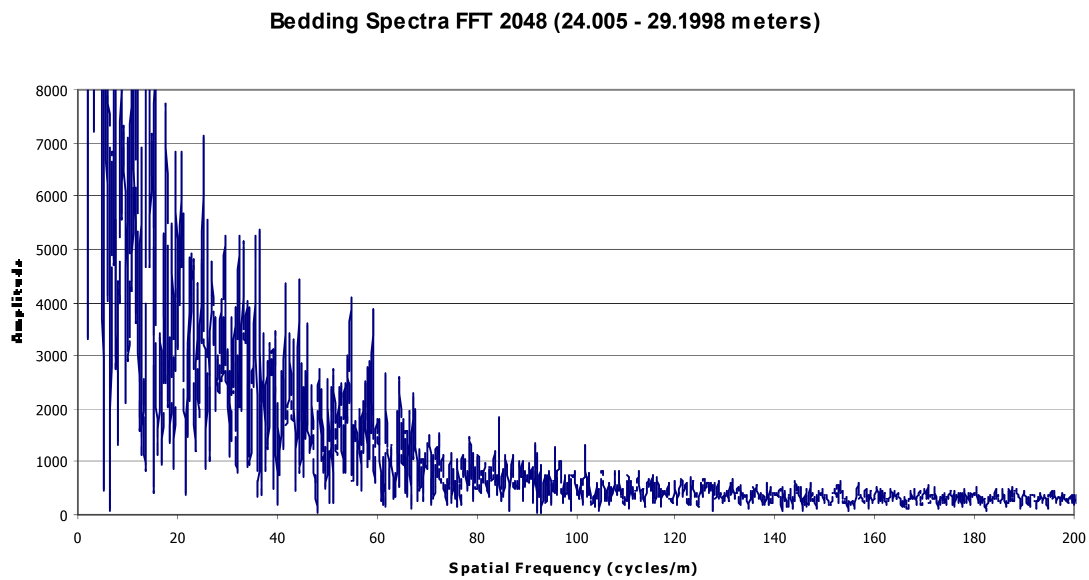

Figure 4.24. Graph of FFT bedding spectra from proximal levee deposits for 5 meters of the log. Spatial frequency plotted on the x-axis and amplitude on the y-axis.

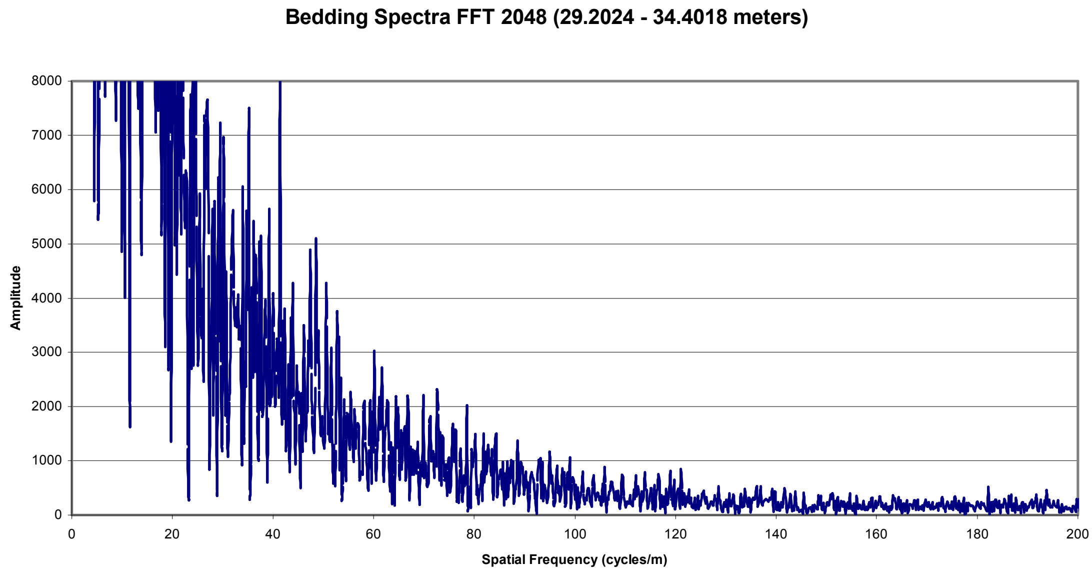

Figure 4.25. Graph of FFT bedding spectra from proximal levee deposits for 5 meters of the log. Spatial frequency plotted on the x-axis and amplitude on the y-axis.

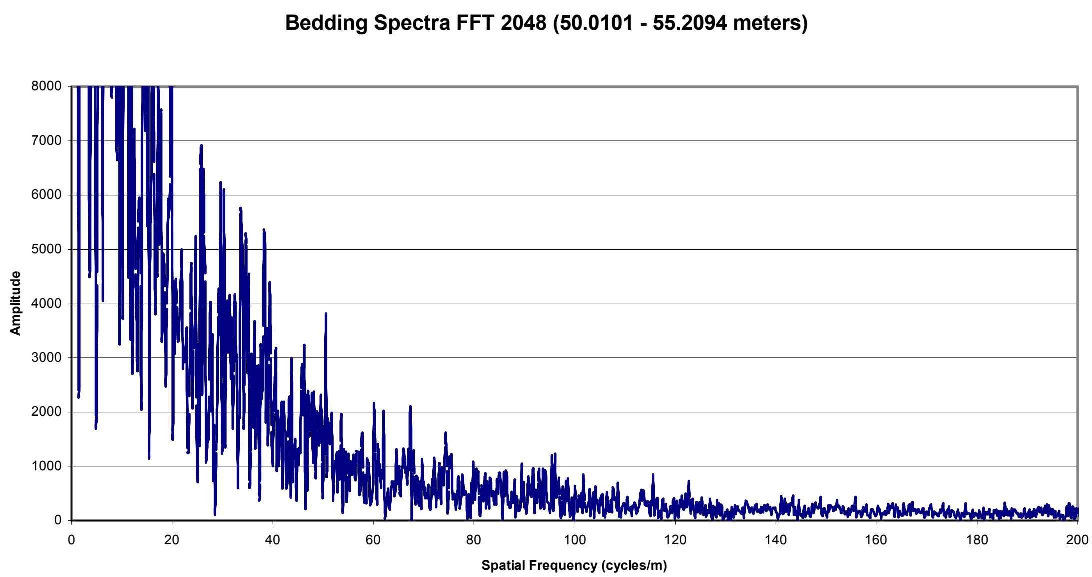

Figure 4.26. Graph of FFT bedding spectra from distal levee deposits for 5 meters of the log. Spatial frequency plotted on the x-axis and amplitude on the y-axis.

The FFT analysis of the reflection coefficient series is from the velocity values of 2.0 km/s for shale and 2.750 km/s for sandstone. There were five groups of 2048 samples plotted from this analysis, two from the proximal levee deposits (Figures 4.27 and 4.28) and three from the distal levee deposits (Figures 4.29, 4.30 and 4.31). Geologic information for each group is included below each figure.

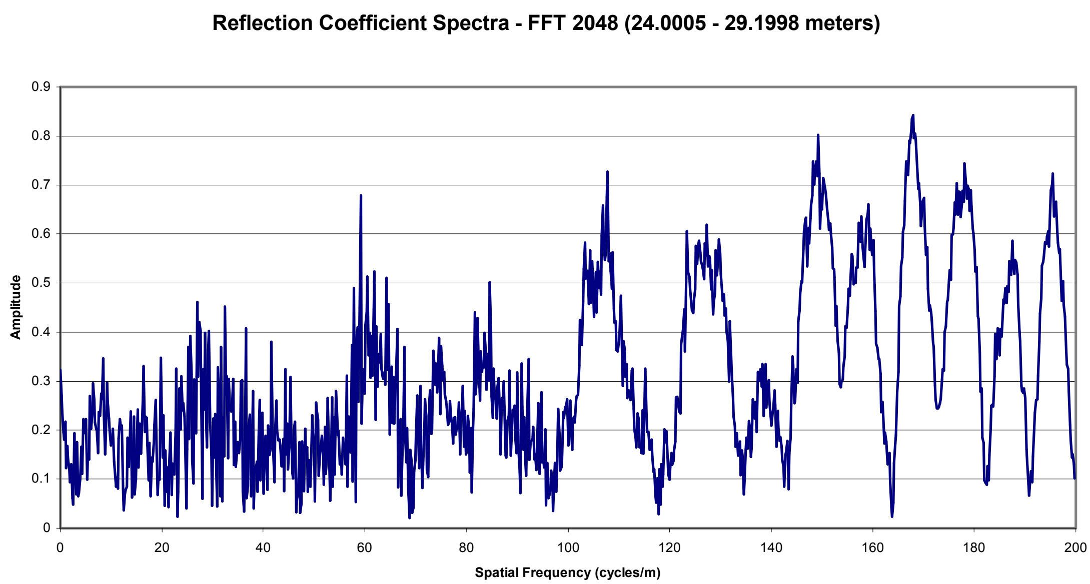

Figure 4.27. Graph of FFT reflection coefficient spectra from proximal levee deposits for 5 meters of the log. Spatial frequency plotted on the x-axis and amplitude on the y-axis. This interval contains 13.5 centimeters of total sandstone and 453 centimeters of total mudstone. The sandstone bed thickness varies from 1 to 7 centimeters. There is bioturbation of the mudstone, some of the sandstones are carbonaceous, and horizontal lamination occurs in this interval.

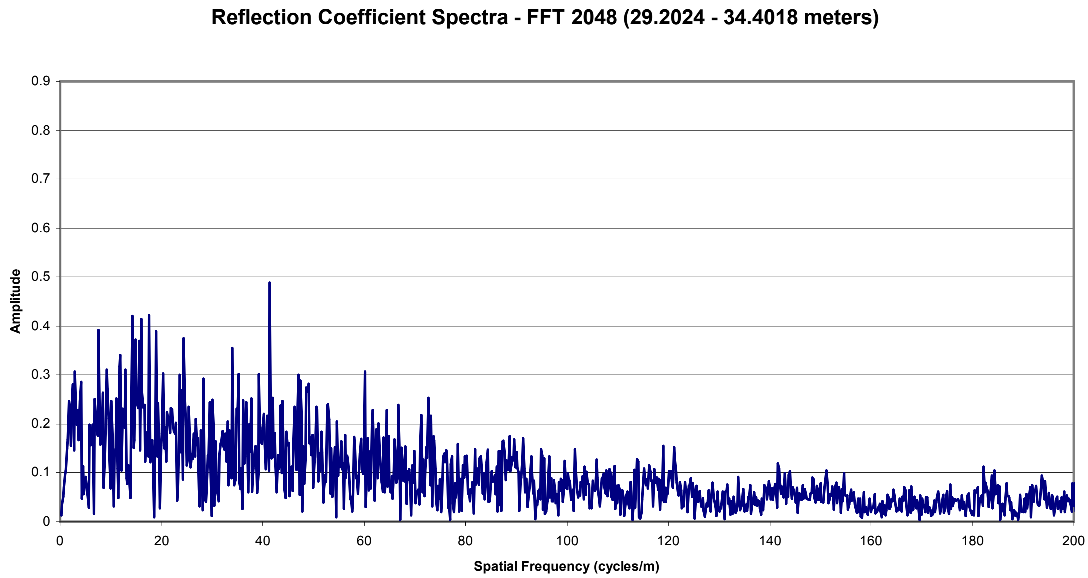

Figure 4.28. Graph of FFT reflection coefficient spectra from proximal levee deposits for 5 meters of the log. Spatial frequency plotted on the x-axis and amplitude on the y-axis. The total thickness of sandstone in this interval is 10.5 centimeters. The thinnest sandstone bed is 1 centimeter and the thickest bed is 4 centimeters. Bioturbation, calcareous concretions, horizontal laminations, ripple laminations, a siderite nodule, and an interval of both carbonaceous sandstone and mudstone are found in this interval of the proximal levee deposit.

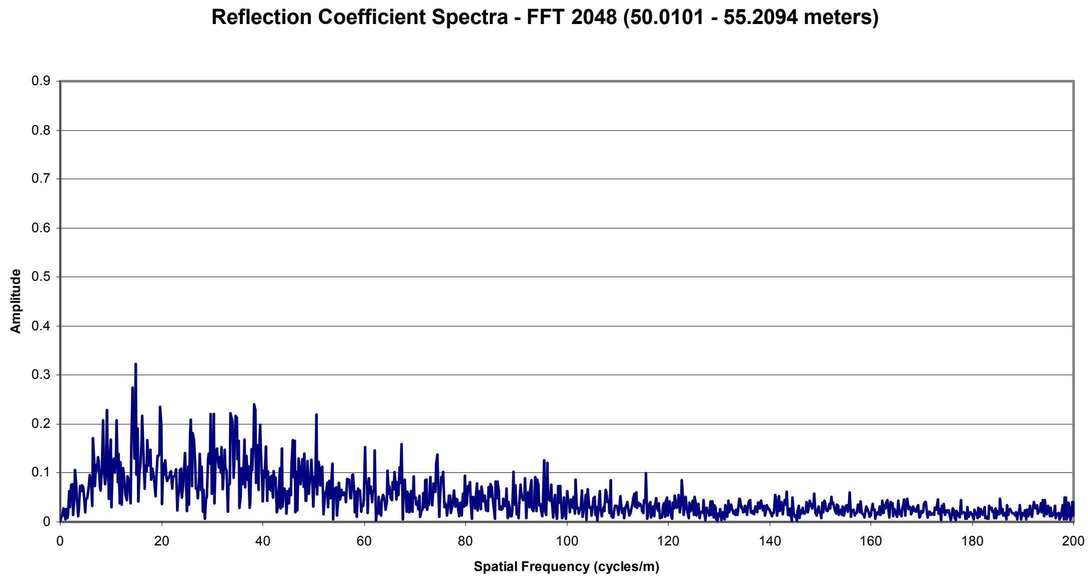

Figure 4.29. Graph of FFT reflection coefficient spectra from distal levee deposits for 5 meters of the log. Spatial frequency plotted on the x-axis and amplitude on the y-axis. Five centimeters of total sandstone are represented in this interval. These beds vary from 1 to 2 centimeters in thickness. The geologic features found are bioturbation, siderite nodules, calcareous concretions, horizontal lamination in one thin sandstone bed, and a lenticular bed.

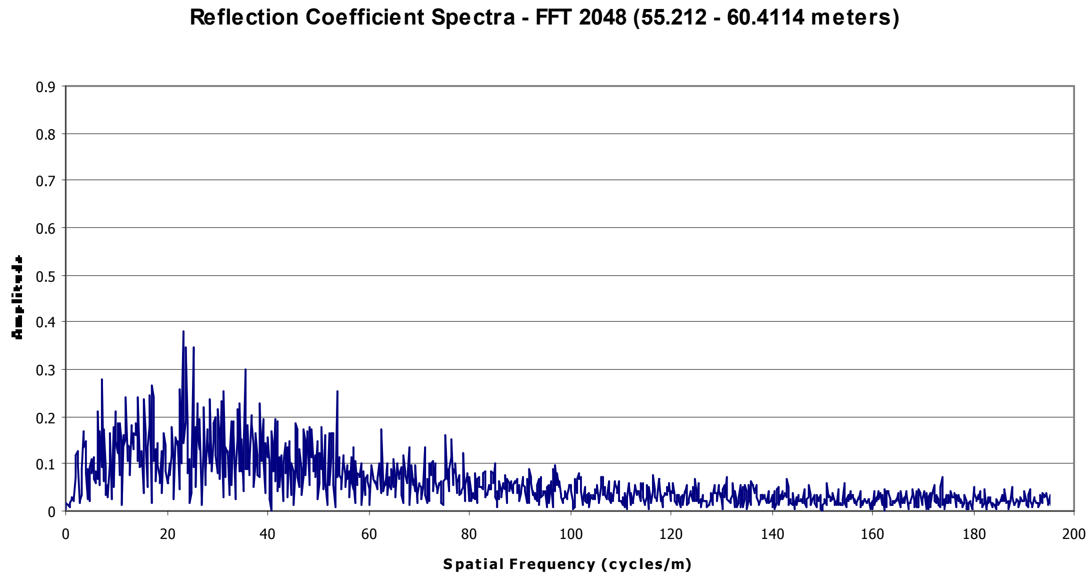

Figure 4.30. Graph of FFT reflection coefficient spectra from distal levee deposits for 5 meters of the log. Spatial frequency plotted on the x-axis and amplitude on the y-axis. The total sandstone thickness is 79.5 centimeters. The sandstone thickness variation ranges from 2 to 26 centimeters. Geologic features identified in this interval are bioturbation, horizontal lamination, ripple lamination, and several sandstones are carbonaceous.

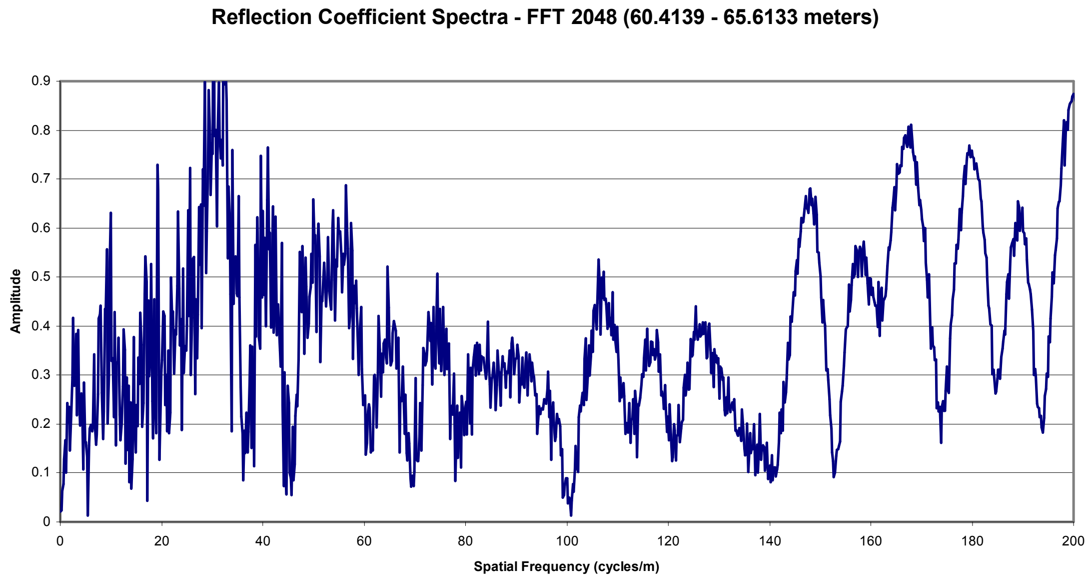

Figure 4.31. Graph of FFT reflection coefficient spectra from distal levee deposits for 5 meters of the log. Spatial frequency plotted on the x-axis and amplitude on the y-axis. The total sandstone thickness is 149 centimeters and the range of sandstone thickness varies from 1 to 22 centimeters. Bioturbation, horizontal lamination, ripple lamination, climbing ripple lamination, carbonaceous sediments, calcareous concretions, and faults are found in this interval.

The question of whether reflectivity is white resulted from the FFT analysis. The equation for a white reflectivity series (Castagna, 2004) is:

$$\frac{\sum r_i(f)^2}{\sum r_r(f)^2} = 1 \qquad (4.33)$$

where r_i is the imaginary component of the FFT, and r_r is the real component of the FFT. This equation was applied to the reflection coefficient FFT with sample rate 2048. The data was broken into three sets of proximal levee groups and four sets of distal levee groups. On average the proximal levee groups were 90% white. The four distal levee groups were more variable but the total distal levee group calculated as one package was white.

WELL LOG SPECTRAL RESULTS

The bedding spectra results do not indicate a change between the proximal and distal levee deposits. Each graph shows the same characteristics and spikes. They all exhibit high amplitudes at lower spatial frequency (Figures 4.24, 4.25, and 4.26).

The reflection coefficient spectra results show variation for each of the five graphs plotted. The proximal levee deposits (Figures 4.27 and 4.28) vary from widely spaced high amplitudes to lower amplitudes. The distal levee deposits (Figures 4.29, 4.30, and 4.31) indicate variation among these three plots. Several of the distal levee plots exhibit tight, low amplitudes and another plot indicates that the amplitudes are high and widely spaced.

The separation of the depositional packages into multiple FFT analyses may have distorted the results. There was not a dominant spatial frequency for both the proximal and distal levee deposits and no definite indication that the FFT analysis could differentiate between the two. The results found in this research do not indicate that the FFT analysis is not a good method to distinguish between proximal and distal levee packages. It only indicates that the analysis conducted did not provide the desired results.

The microresistivity of the borehole image log was used to detect bed boundaries and the bed boundary results were used to investigate various geological and geophysical parameters. The next chapter investigates if there is a relationship between microresistivity and permeability. The chapter correlates the borehole image log to the core and then compares the microresistivity data from the borehole image log to the permeability measurements taken from the core.

CHAPTER 5. RELATIONSHIP OF CORE AND PERMEABILITY TO MICRORESISTIVITY

Microresistivity data can be used to detect bed boundaries and characterize thin-beds. One can acquire permeability measurements from core data and thus investigate whether there is a relationship between microresistivity and permeability measurements. This chapter discusses the procedure of correlating the core description and the permeability data to the borehole image log and identifying rock type through the correlations.

CORRELATION

The objective of this chapter is to evaluate various techniques that could potentially be used to relate the rock type to the microresistivity data on a thin-bed scale using data from the North well. The purpose of this analysis is to generate a quantitative and automated lithology log from the microresistivity values and develop a relationship between permeability and microresistivity of thin-bedded intervals.

This analysis is two fold. The first step is to correlate the core description to the borehole image log with respect to depth in the well bore (i.e. a simple core to log correction). Once that step is completed, then the permeability measurements can be correlated to the borehole image log. The second step is to analyze the microresistivity and permeability data to determine if a relationship exists.

The permeability data was measured from the core using a pressure-decay profile permeameter (Spang, 2000). Permeability is measured by the rate of pressure decay as nitrogen flows into the sample (Spang, 2000). Measurements were taken at ten centimeter intervals on the core.

The correlation of the borehole image log to the core description was done on the North well. Four key markers were identified on the borehole image log and were used to correlate the core description to the borehole image log. The four key markers were three concretions and one unconformity. The top of the concretion key markers are on the North borehole image log at the following depths: 30.56 m, 49.46 m, and 63.48 m. The unconformity is located at a depth of 42.21 m. On the core description, the top of the concretion markers are at the following depths: 30.8 m, 50.05 m, and 64.34 m.

There were some adjustments to the core description to get the core to match the borehole image log (Appendix C - core description with changes). On the core description, there was a 23 cm gap at 30.50 m that was removed. This gap was adjusted to contain more of the upper mudstone and the lower calcareous concretion. The bottom of the concretion and everything below was moved up 5 cm. The above adjustment to the core allowed the first good key marker to match the borehole image log. The next adjustment to the core description was to remove the 14 cm gap at 36.05 m. This allowed all of the sediment packages below this gap to be moved up in depth and then the unconformity on the core matched the borehole image log. The next concretion needed to be matched on the core description and the borehole image log. Only one additional adjustment had to be made to match the core depth of the concretion to that of the borehole image log. A 15 cm mudstone bed at depth 49.80 m was removed. After matching the first three key markers, many more adjustments were made below 50.00 m to match the last concretion at 63.48 m. The first adjustment was to reduce a 22 cm mudstone at 55.10 m to 13 cm in thickness to correspond to the borehole image log. The sandstone at 59.45 m was adjusted to 18 cm from 26 cm. The 6.5 cm mudstone at 59.70 m was adjusted to 9 cm and the sandstone below this mudstone was adjusted from 7 cm to 6 cm. Between 62.0 m and 63.0 m several beds were removed from the core description to match the borehole image log. These beds were a 1cm mudstone, a 2 cm mudstone, 2.5 cm sandstone, a 1 cm sandstone, a 2 cm sandstone, and a 3.5 cm mudstone. Between the same interval, a 15.5 cm mudstone was adjusted to the thickness of 11 cm. The last concretion is at 63.48 m was adjusted from 16 cm to 22 cm to match the borehole image log. To accurately match other beds on the borehole image log including a thick horizontal laminated sandstone, other beds were adjusted. Between the interval of 65 m to 66 m, a 4.0 cm sandstone was removed. Between 67 m and 68 m, a 2.5 cm sandstone, 2.0 cm sandstone, 5.5 cm mudstone, 5.0 cm sandstone, and a 1.0 cm mudstone was removed. In this interval, a 21.5 cm mudstone was adjusted to 19 cm and a 39 cm sandstone was adjusted to 44 cm. From 68 m to the bottom of the core description a 1.0 cm sandstone and a 3.0 cm mudstone was removed to allow the correlation to match.

Since permeability measurements were made on the core, the same adjustments core-to-log were made to the permeability measurements. Once the core description and the permeability measurements matched the borehole image log, the relationship between the microresistivity values and permeability values was analyzed.

PERMEABILITY ANALYSES

Several experiments were conducted once the permeability and borehole image log data were correlated. The processed microresistivity data from the borehole image log was used in all of the following analyses. There were analyses conducted using the uncalibrated and calibrated processed microresistivity data. There were two sets of permeability measurements made on the North core, the Colorado School of Mines (CSM) and the University of Oklahoma (OU) measurements. In the following three experiments, the CSM permeability measurements were used.

First experiment:

The uncalibrated microresistivity values were used in this experiment. Each microresistivity value that had a corresponding permeability value was used to generate a crossplot of microresistivity versus permeability. Graphs were generated to evaluate the data for each lithologic type. The lithologic types evaluated were shale (Figure 5.1), massive sandstone (Figure 5.2), horizontal laminated sandstones (Figure 5.3), and climbing ripple laminated sandstones (Figure 5.4).

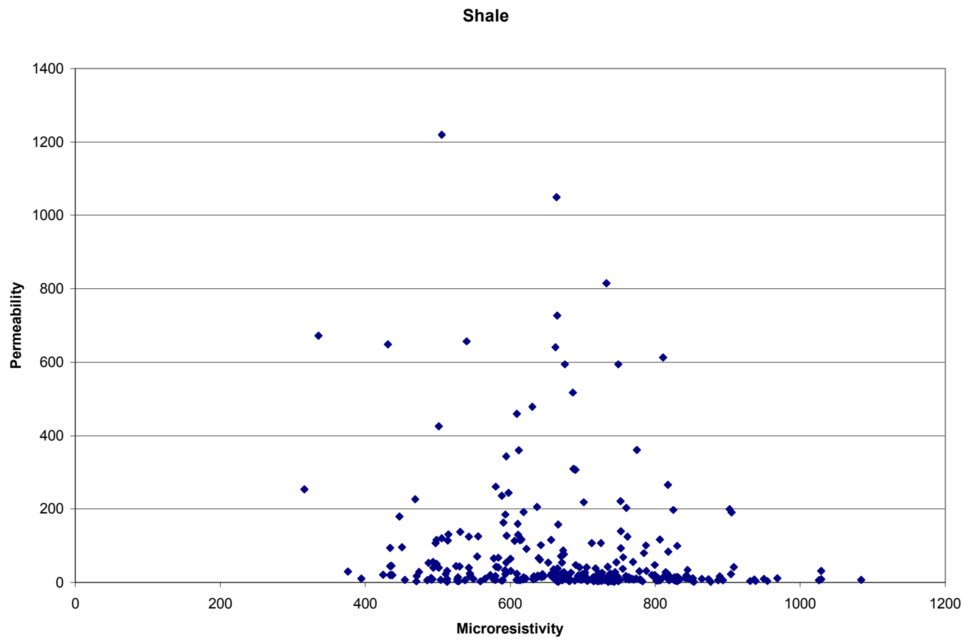

Figure 5.1. Uncalibrated microresistivity versus CSM permeability crossplot for shale.

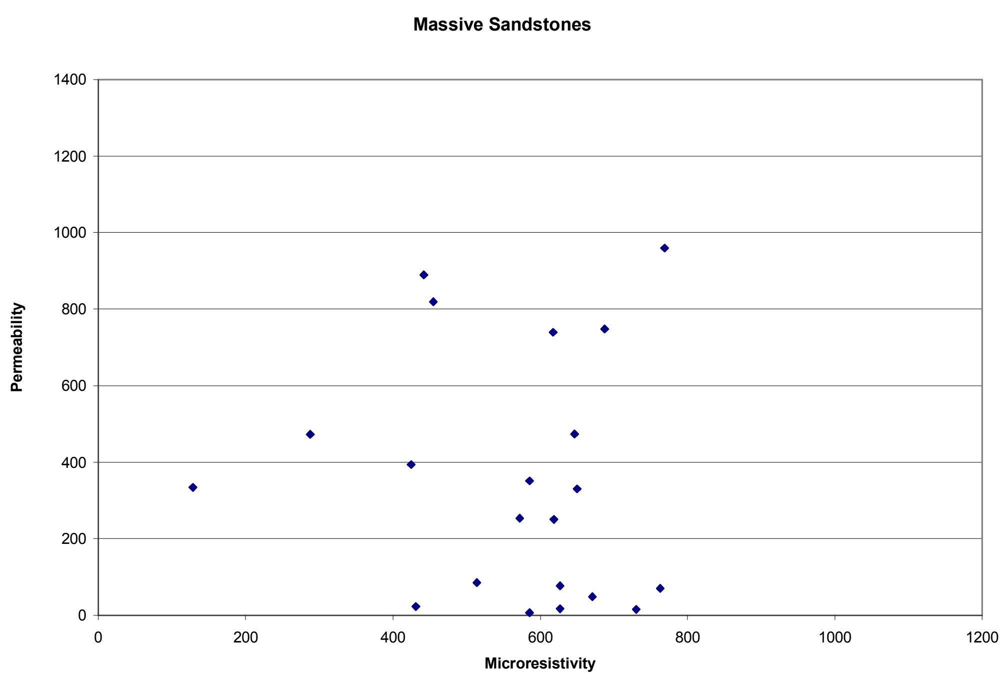

Figure 5.2. Uncalibrated microresistivity versus CSM permeability crossplot for massive sandstones.

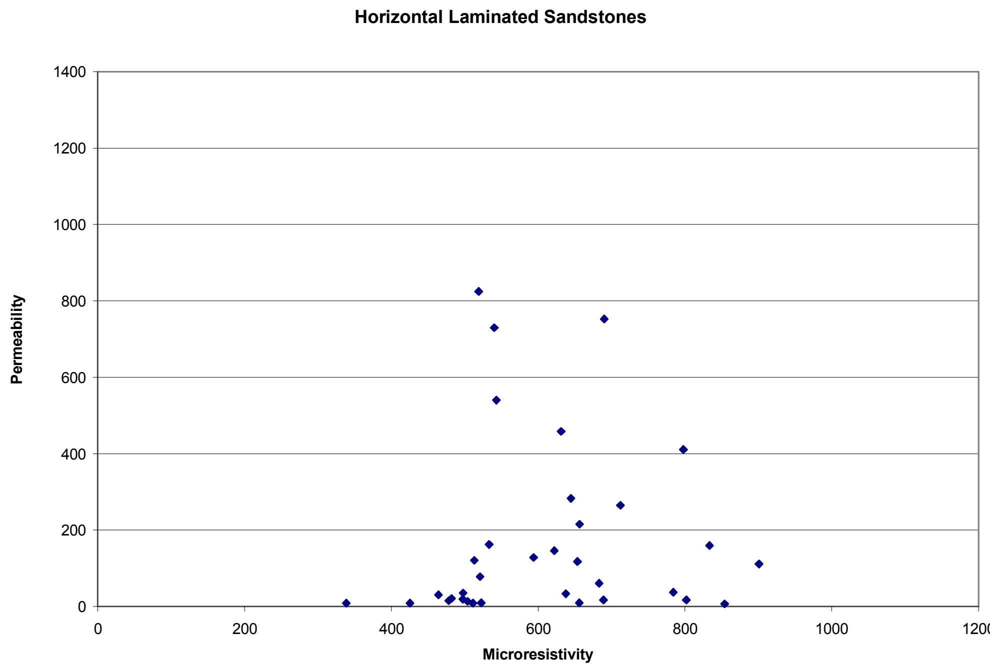

Figure 5.3. Uncalibrated microresistivity versus CSM permeability crossplot for horizontal laminated sandstones.

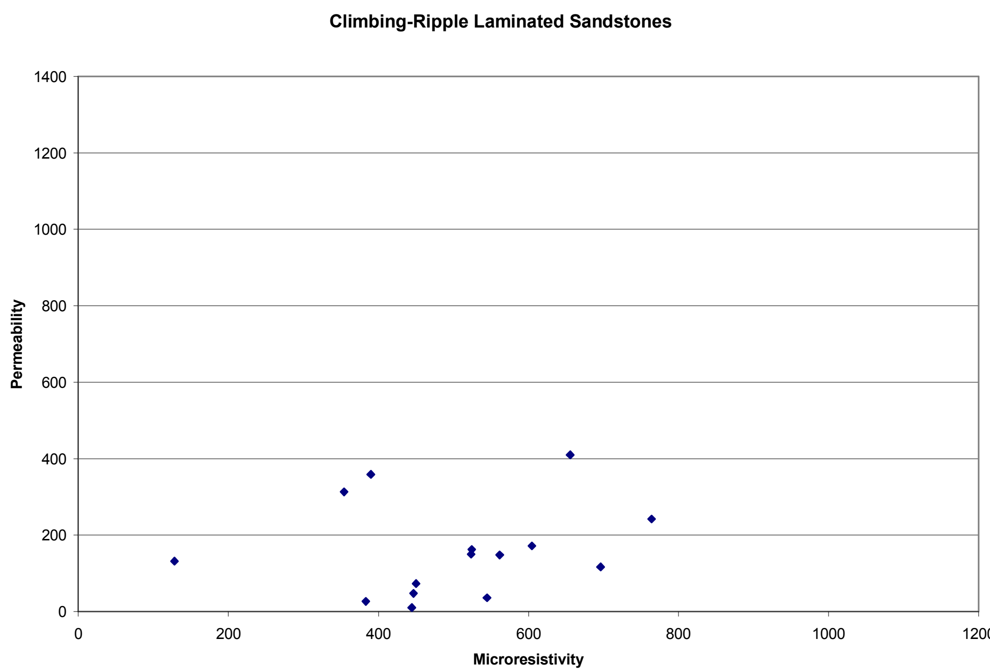

Figure 5.4. Uncalibrated microresistivity versus CSM permeability crossplot for climbing ripple laminated sandstones.

The figures show that there is an overlap of microresistivity values for the shale and sandstones. These figures do not indicate a correlation between permeability and microresistivity.

Two bar graphs were generated using the average and standard deviation of the microresistivity and permeability values. To create the graphs, the average and standard deviation of the microresistivity and permeability values were calculated for each individual lithologic type. Each lithologic type is plotted as an individual bar. The minimum value for each bar is calculated by subtracting the standard deviation value from the average. The maximum value for each bar is calculated by adding the standard deviation value to the average. Each bar represents the statistical spread or range of the values for each lithologic type. Figure 5.5 is a bar graph using the microresistivity values. This figure demonstrates that there is overlap of microresistivity values and suggests no clear indication that particular microresistivity values belong to a certain lithology. The permeability values for each lithology are plotted on Figure 5.6. This figure shows an overlap of permeability values for all lithologic types.

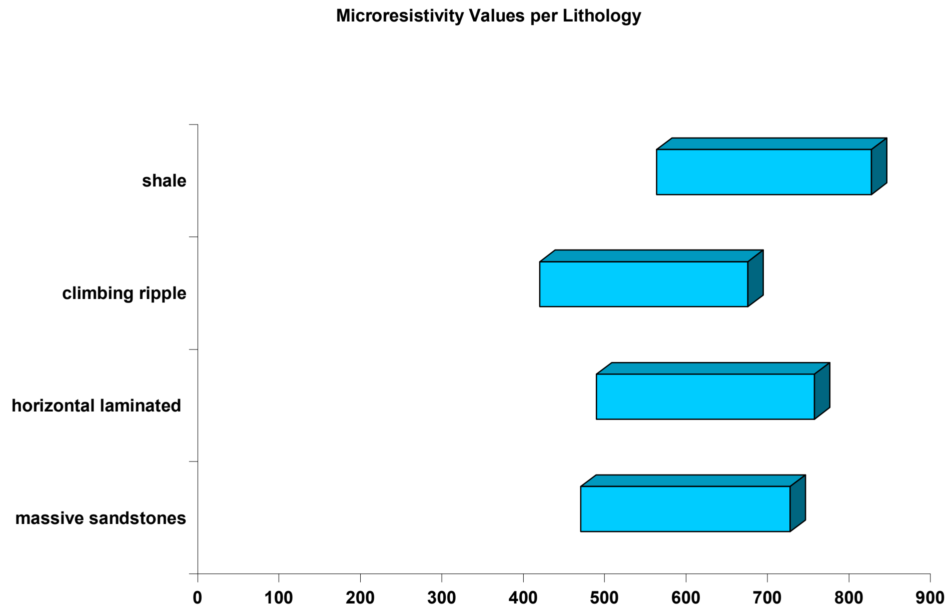

Figure 5.5. Bar graph of uncalibrated microresistivity per lithology. Each bar represents the statistical spread or range of the values for each lithologic type.

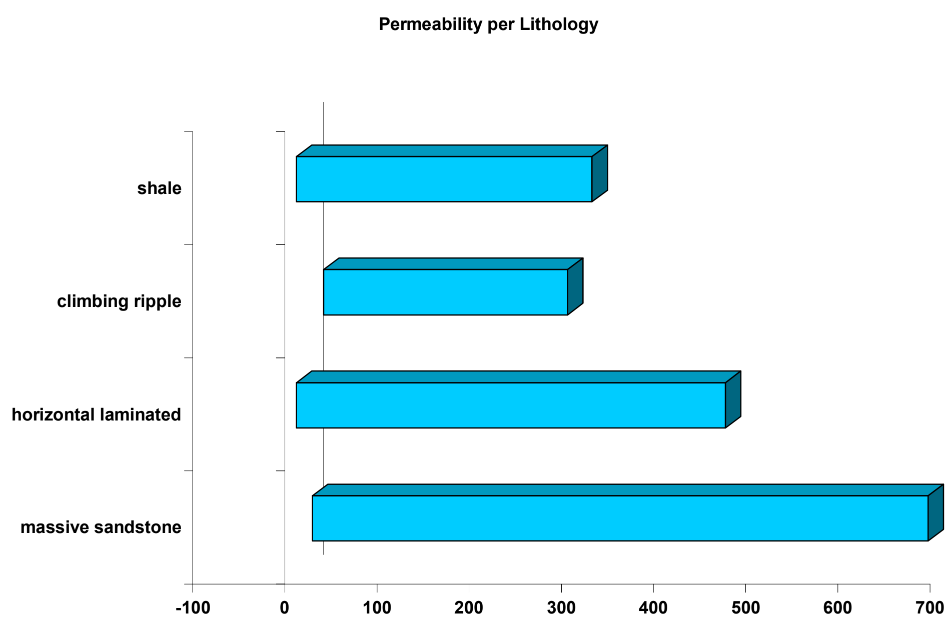

Figure 5.6. Bar graph of CSM permeability per lithology. Each bar represents the statistical spread or range of the values for each lithologic type.

Second experiment:

Due to the inconclusive results from the first experiment, a second experiment using the uncalibrated microresistivity data was conducted. This experiment was done by using a sliding windowed average over a given length (1 cm, 10 cm, and 20 cm). A window length of 1 cm was chosen since this was the smallest bed thickness on the core. Many beds on the core were between 1 cm and 10 cm in thickness; therefore, a 10 cm window was used. To encompass larger beds a 20 cm window was chosen.

The sliding windowed average results were plotted versus the permeability according to shale and sandstone lithologies (Figures 5.7, 5.8, 5.9, 5.10, 5.11, and 5.12). There is no indication that lithology can be differentiated from this technique. There is overlap of average microresistivity values for both shales and sandstones.

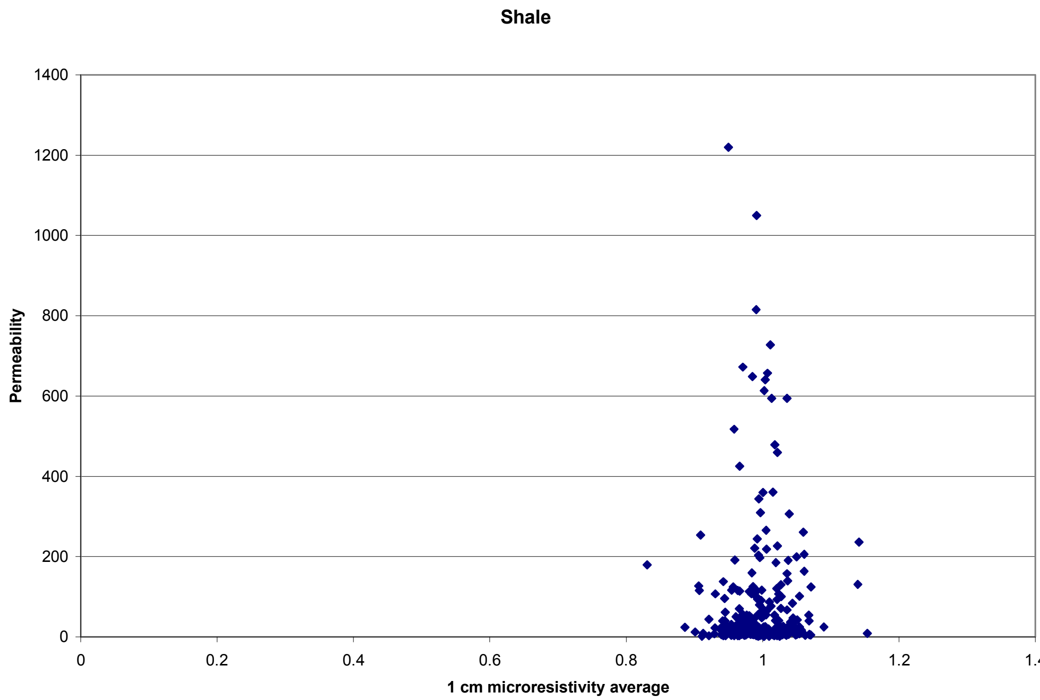

Figure 5.7. Sliding windowed average of 1 cm using the uncalibrated microresistivity values for shale.

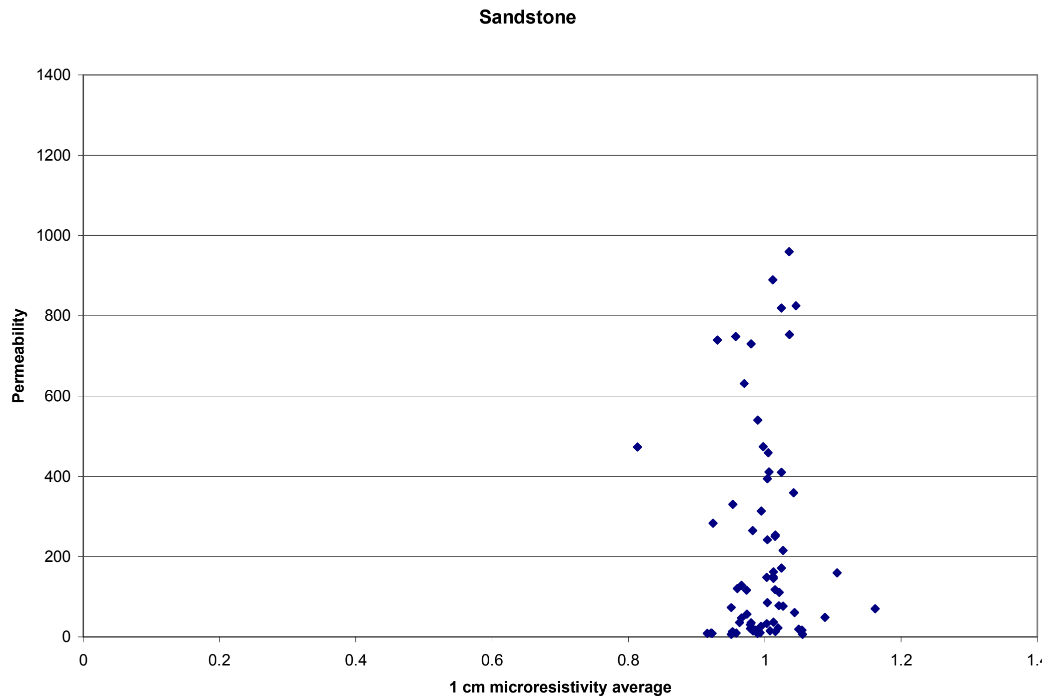

Figure 5.8. Sliding windowed average of 1 cm using the uncalibrated microresistivity values for sandstone.

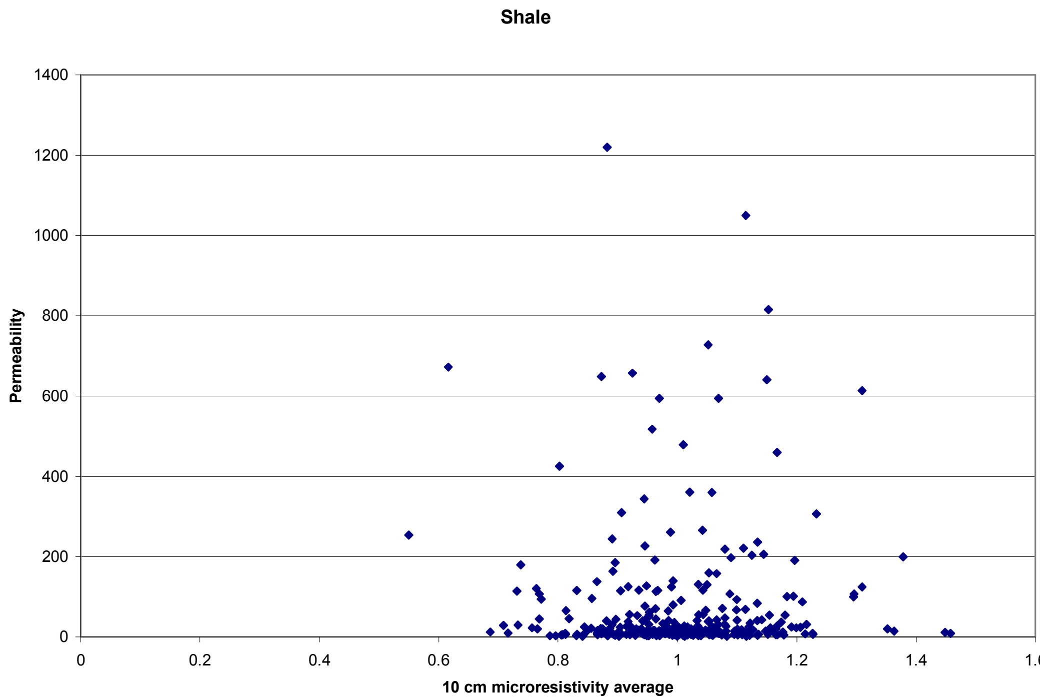

Figure 5.9. Sliding windowed average of 10 cm using the uncalibrated microresistivity values for shale.

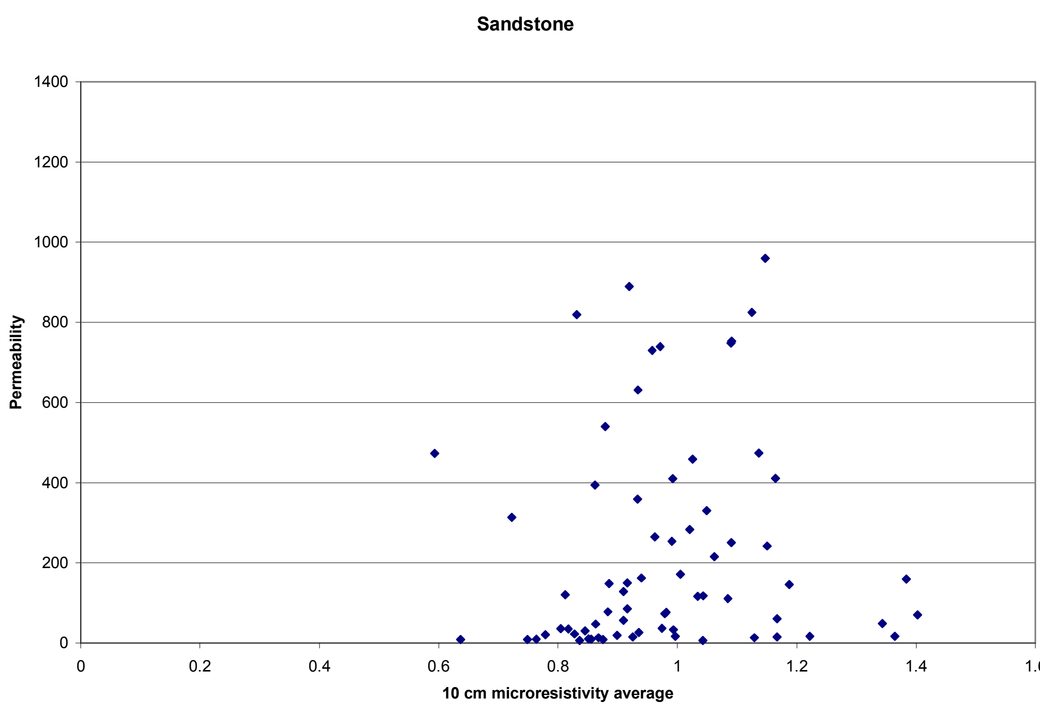

Figure 5.10. Sliding windowed average of 10 cm using the uncalibrated microresistivity values for sandstone.

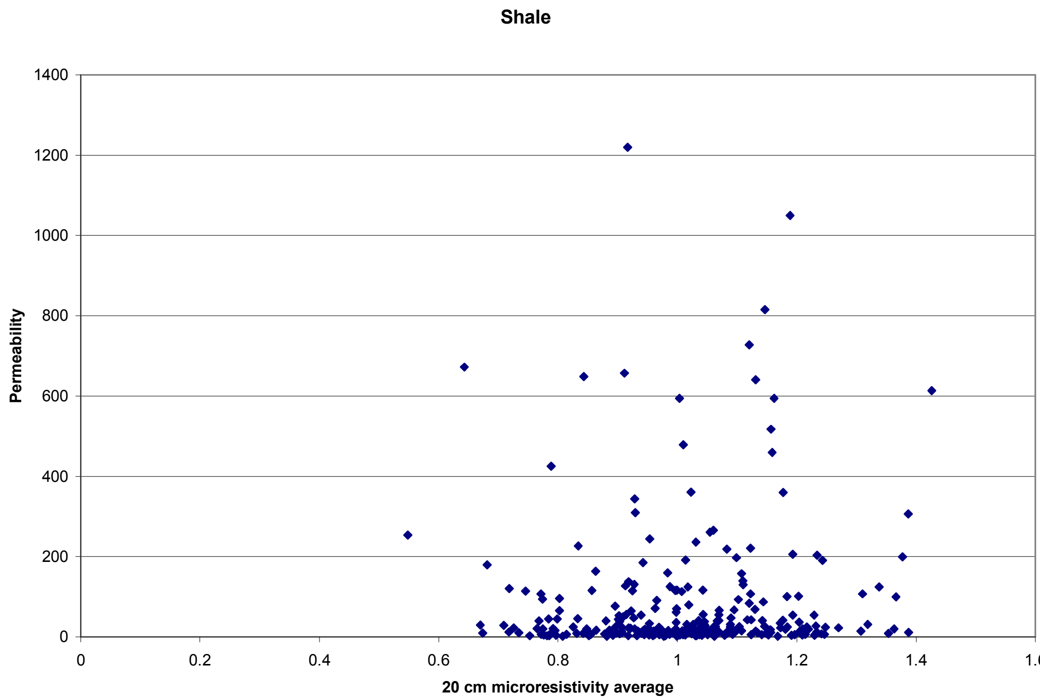

Figure 5.11. Sliding windowed average of 20 cm using the uncalibrated microresistivity values for shale.

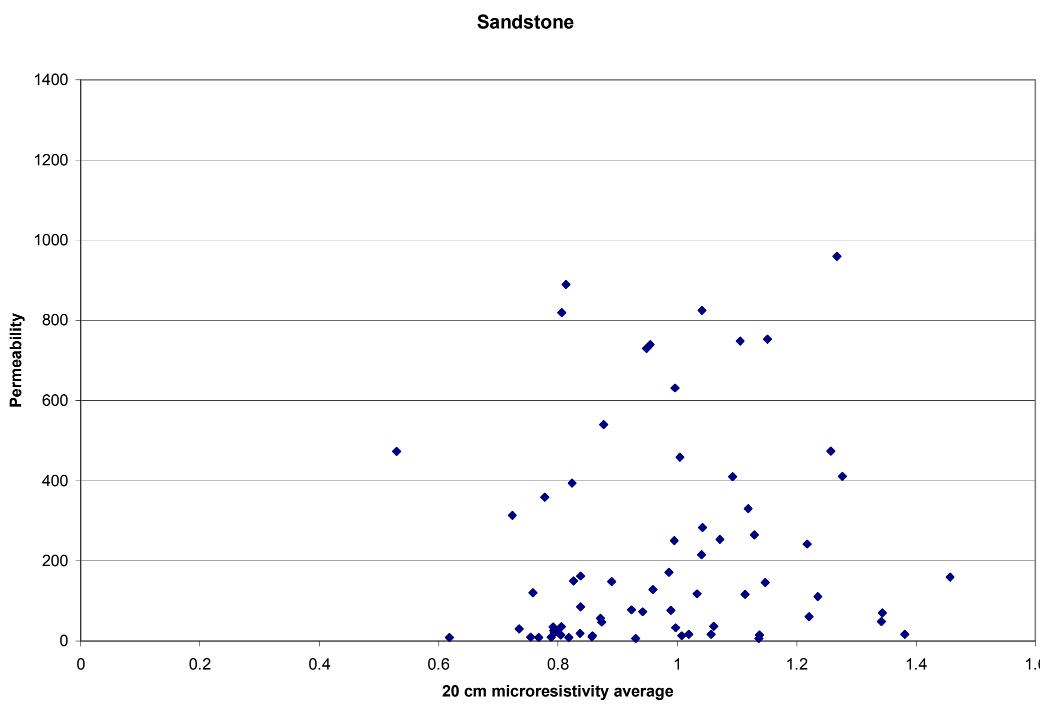

Figure 5.12. Sliding windowed average of 20 cm using the uncalibrated microresistivity values for sandstone.

Third experiment:

The uncalibrated microresistivity values did not provide the results needed to determine lithology from microresistivity values. Thus, the calibrated microresistivity values were used in this experiment to determine if lithology could be distinguished using microresistivity values.

The uncalibrated microresistivity values were calibrated with the high resolution shallow resistivity laterolog (HLLS) to obtain the calibrated microresistivity values. The calibration was done in the Schlumberger processing flow (Chapter 2). It was done in the BorScale™ module. The calibrated microresistivity values were exported out of BorScale™ and a single curve (Pad 1 Curve 6) was chosen for use in the analysis.

For each permeability value, the corresponding calibrated microresistivity value was plotted on a graph (Figures 5.13, 5.14, 5.15, and 5.16). The shale, massive sandstones, horizontal laminated sandstones, and the climbing ripple sandstones overlap for microresistivity values. There is no indication of trends or patterns, thus the calibrated microresistivity values do not indicate lithology types.

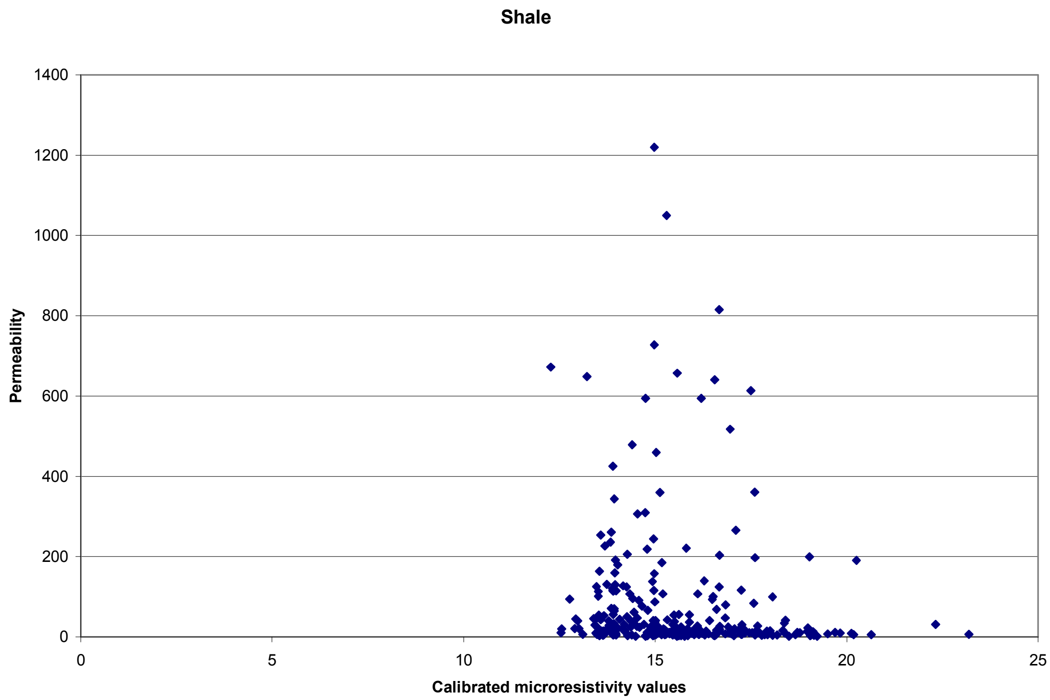

Figure 5.13. Calibrated microresistivity versus CSM permeability crossplot for shale.

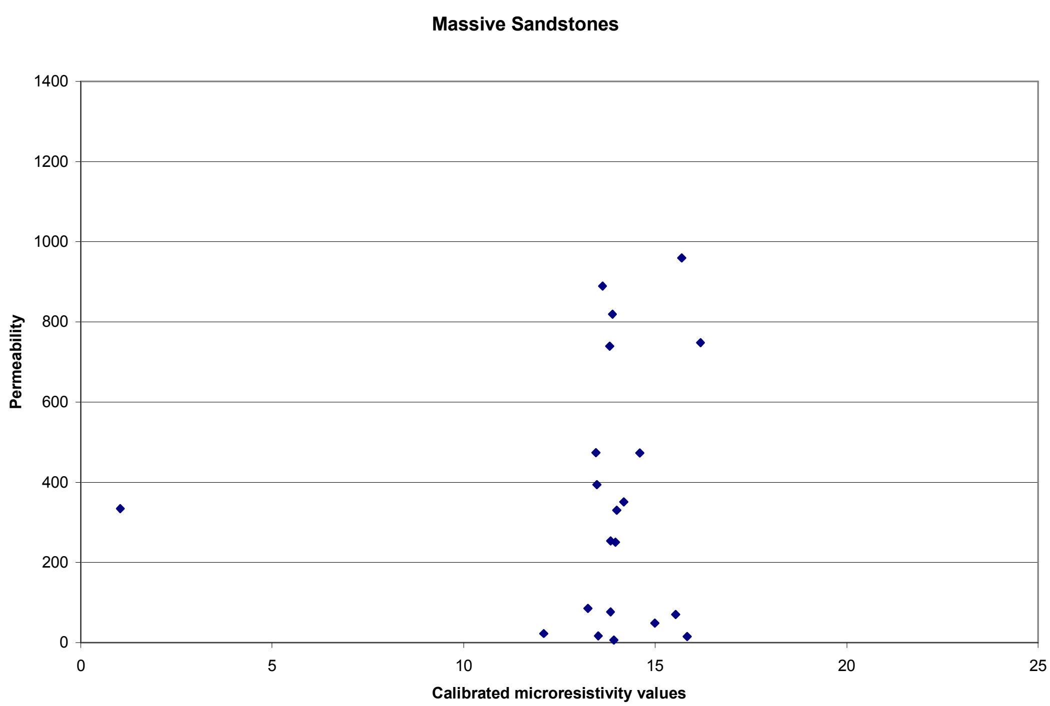

Figure 5.14. Calibrated microresistivity versus CSM permeability crossplot for massive sandstones.

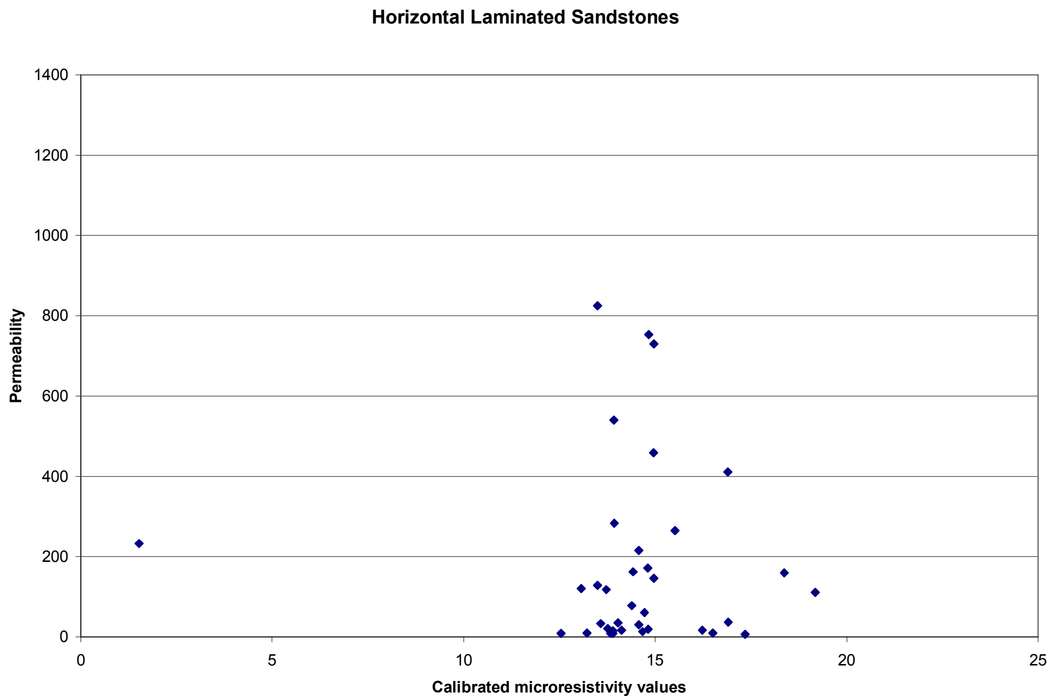

Figure 5.15. Calibrated microresistivity versus CSM permeability crossplot for horizontal laminated sandstones.

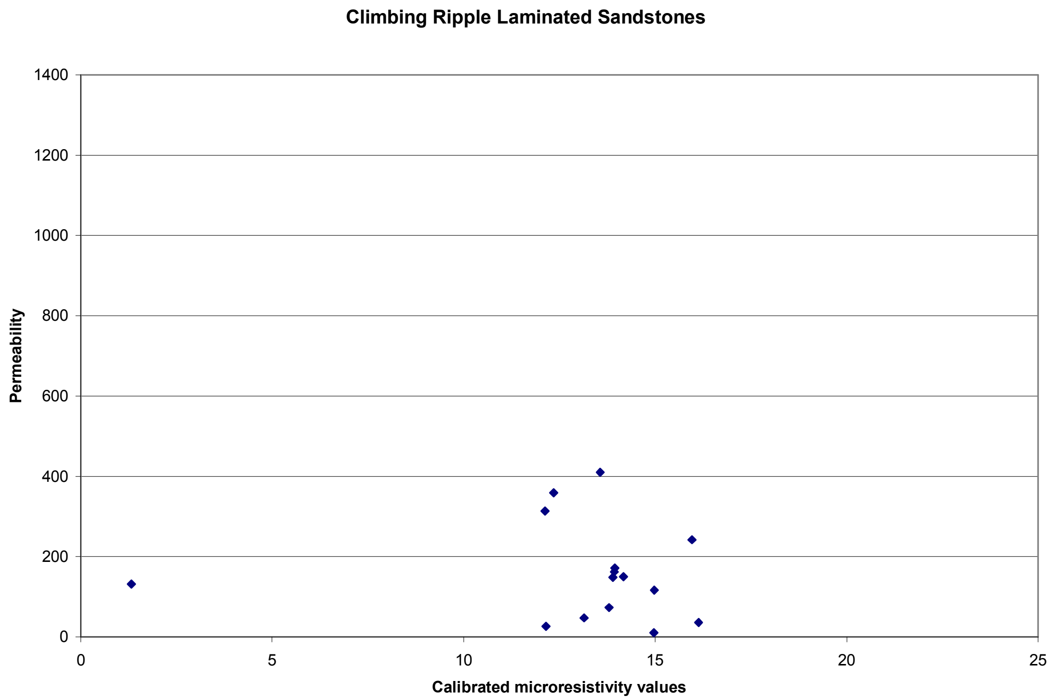

Figure 5.16. Calibrated microresistivity versus CSM permeability crossplot for climbing ripple laminated sandstones.

Figure 5.17 is a bar graph of the calibrated microresistivity for each lithologic type. The plot shows a clear overlap of microresistivity values for the lithologies.

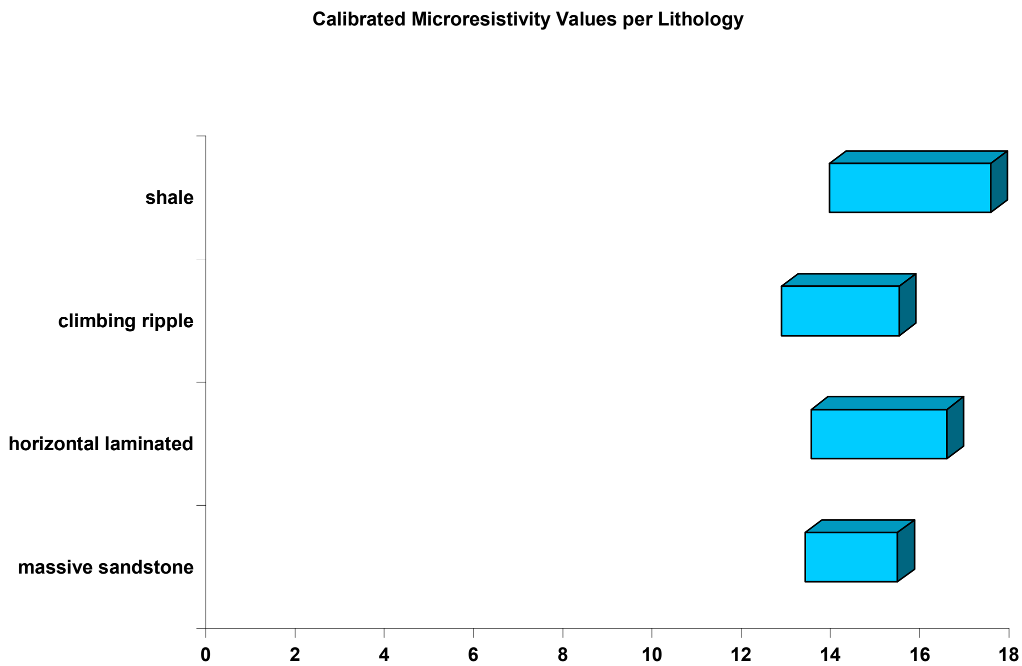

Figure 5.17. Bar graph of the calibrated microresistivity per lithology. Each bar represents the statistical spread or range of the values for each lithologic type.

The CSM permeability measurements were used in the above experiments because it was the first data received in this research. Also, when the data was acquired it was matched up with the appropriate Bouma sequence.

A comparison of the CSM and OU measurements was conducted to see how well the measurements correlated to each other.

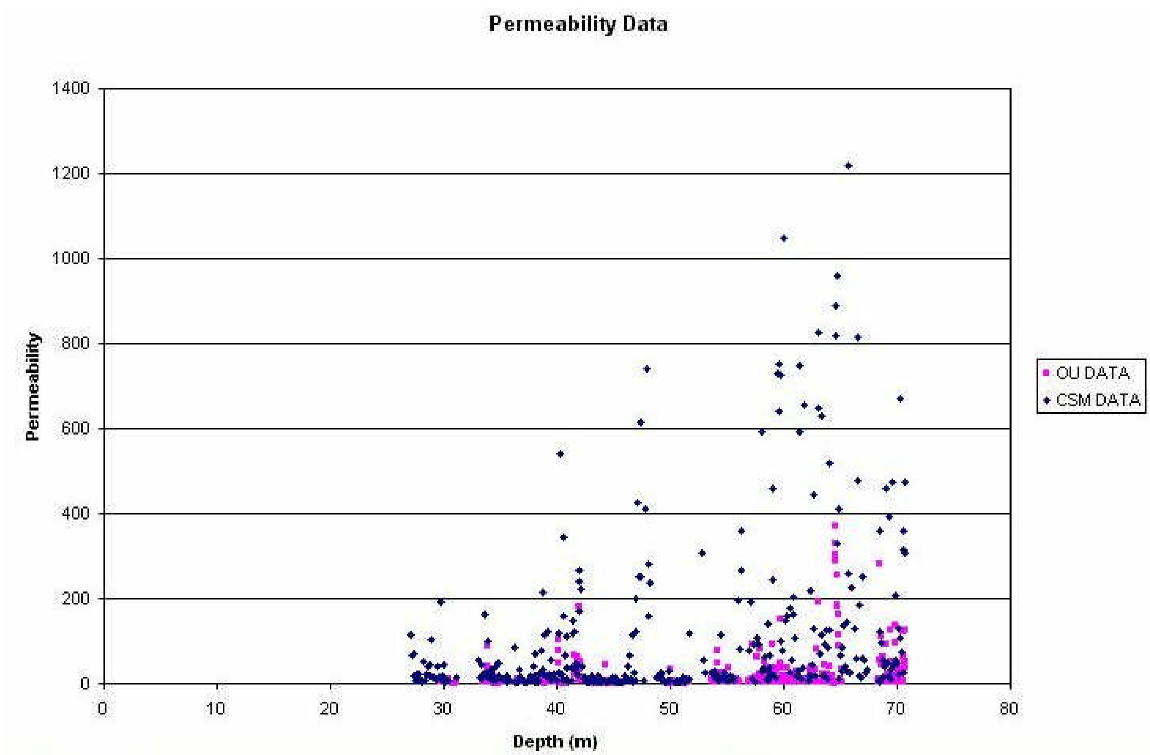

Figure 5.18. Permeability data plotted versus depth for the CSM data (blue diamonds) and OU data (pink squares).

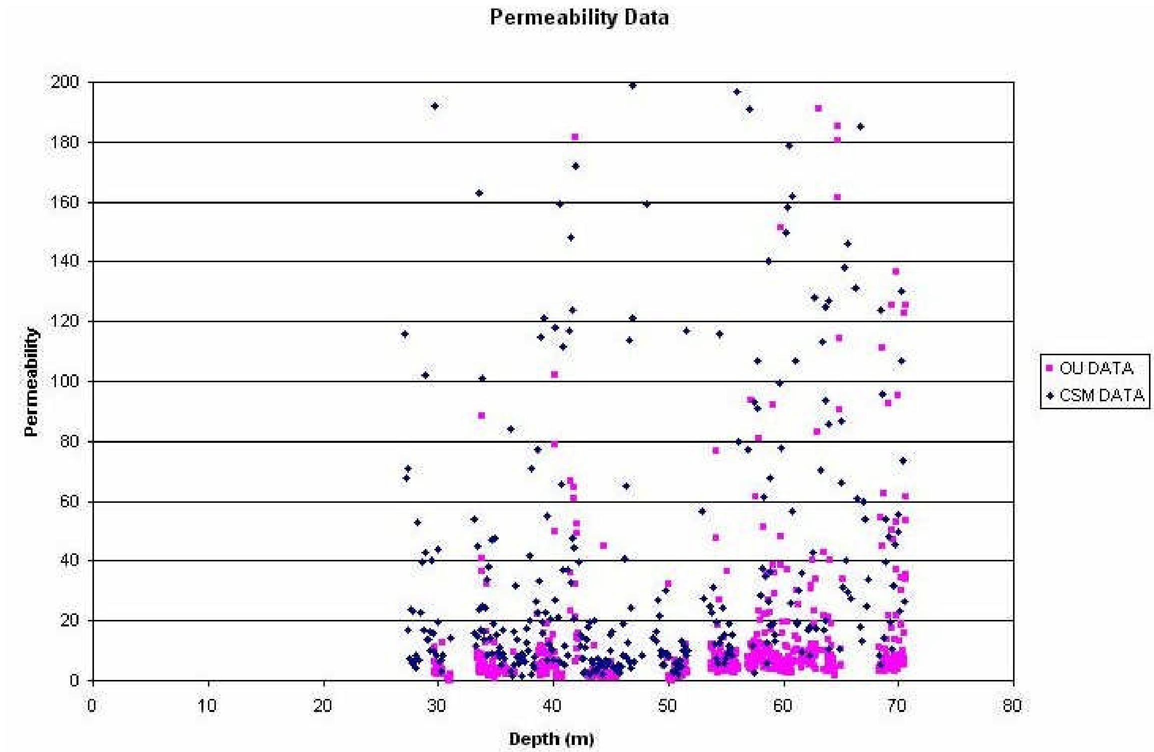

Figure 5.19. Permeability data plotted versus depth for the CSM data (blue diamonds) and OU data (pink squares). Vertical scale expanded to show details.

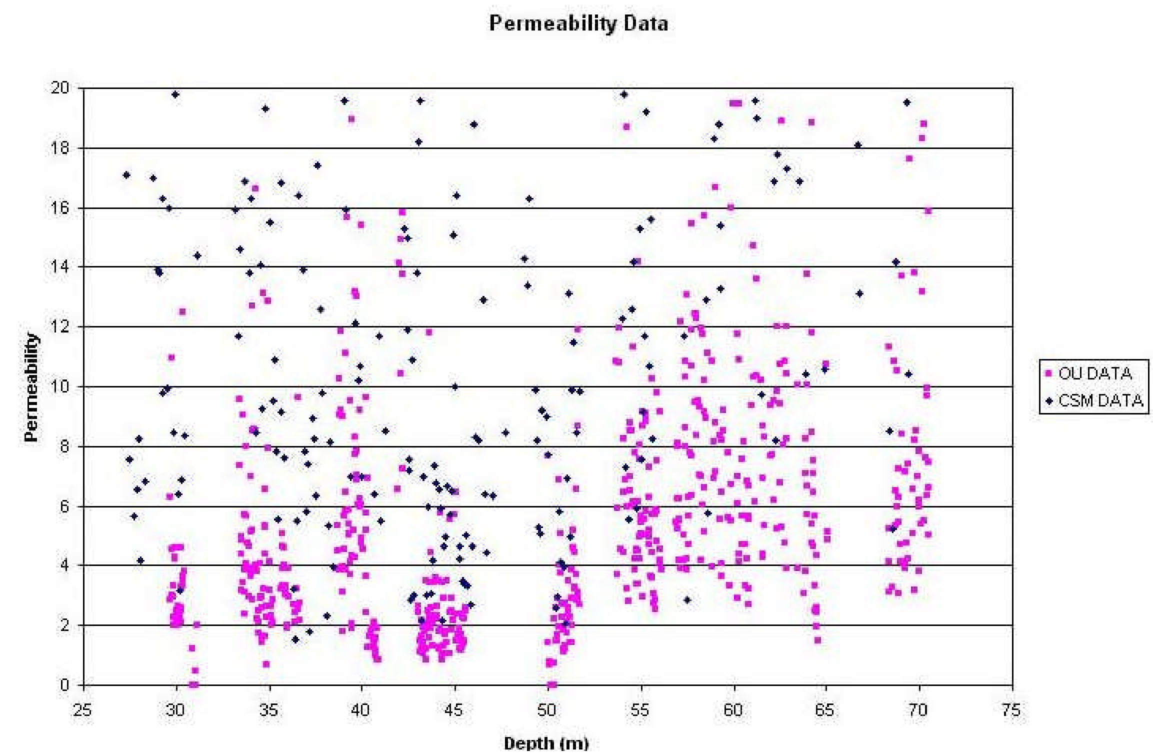

Figure 5.20. Permeability data plotted versus depth for the CSM data (blue diamonds) and OU data (pink squares). Vertical scale expanded to show details.

The permeability plotted versus depth graphs show there is no correlation between the CSM and OU measurements. One reason for this could be because the measurements were not taken at the exact same depths for each dataset. More measurements were taken in the OU dataset than the CSM dataset. In addition, the OU permeability measurements are consistently lower than the CSM measurements.

After the comparison of the two datasets was made and no correlation was indicated, the OU measurements were plotted to see if they would provide a better indication of lithology.

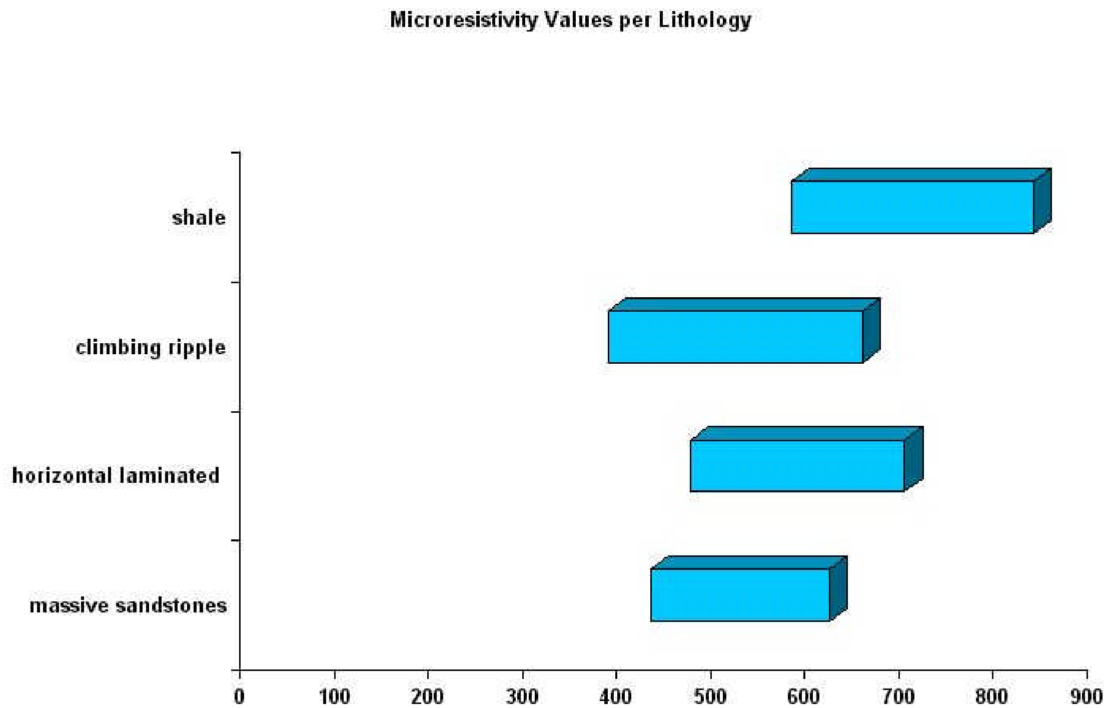

Figure 5.21. Bar graph of uncalibrated microresistivity per lithology. Each bar represents the statistical spread or range of the values for each lithologic type.

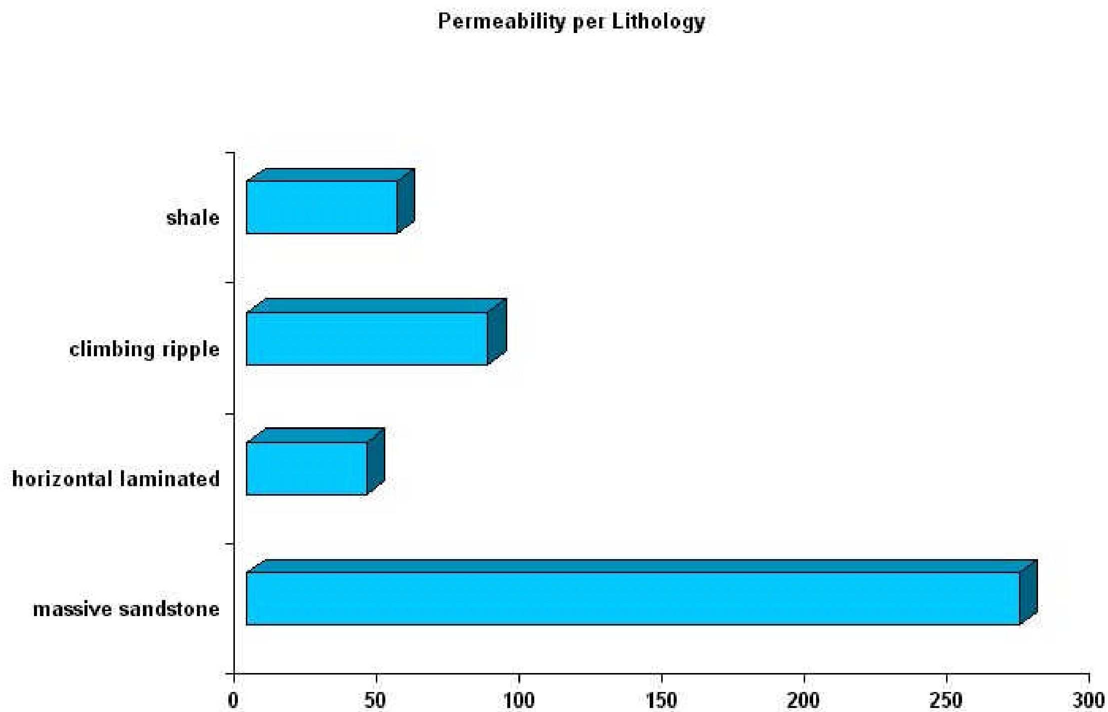

Figure 5.22. Bar graph of OU permeability per lithology. Each bar represents the statistical spread or range of the values for each lithologic type.

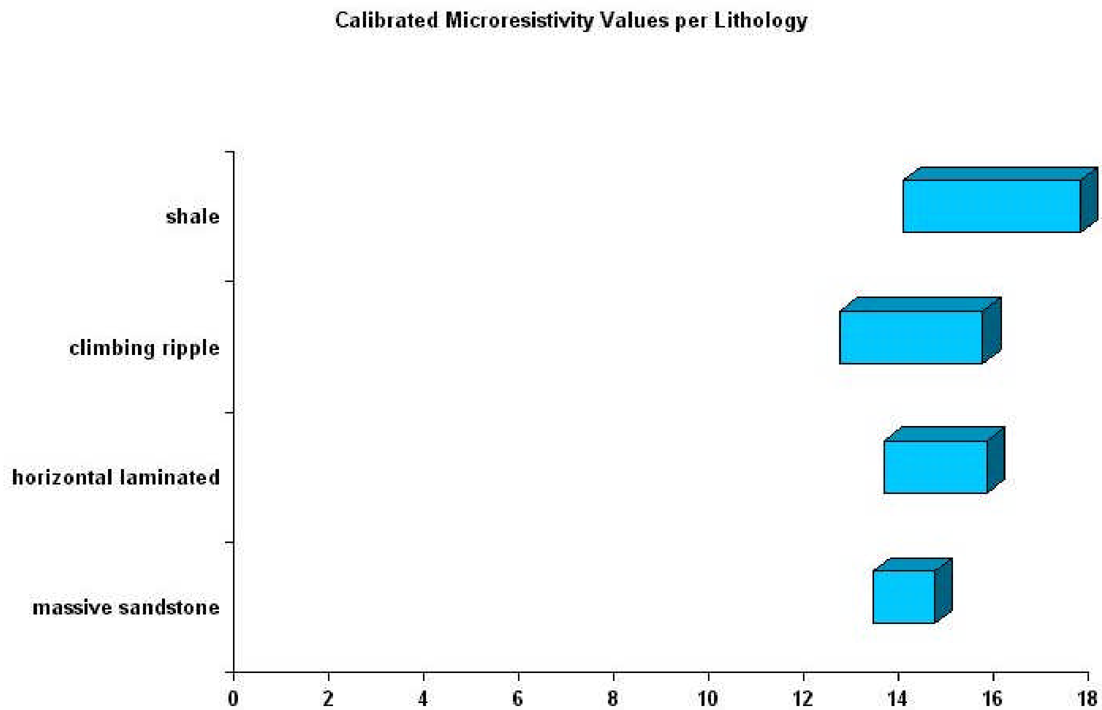

Figure 5.23 Bar graph of the calibrated microresistivity per lithology. Each bar represents the statistical spread or range of the values for each lithologic type.

The OU and CSM permeability measurements indicate that microresistivity, whether it is calibrated or not, is not indicative of lithology. Also, the measurements indicate that permeability is not indicative of lithology.

PERMEABILITY: RESULTS

The experiments with the uncalibrated and calibrated microresistivity values versus permeability did not indicate that lithology type could be identified. The results from the experiments were inconclusive. A recommendation to address the issue of determining lithology from the microresistivity data would be to conduct a detailed analysis of the core. This could be done by doing laser grain size analysis on the core sample to establish a quantifiable relationship between microresistivity and lithology.

After the microresistivity data analyses were completed, the next step was to use the high-resolution seismic line to investigate thin-beds. Spectral decomposition of the high-resolution seismic line was used to determine if the different thin-bedded depositional packages could be identified.

CHAPTER 6. SPECTRAL DECOMPOSITION OF SEISMIC LINE

Thin bedding influences the reflectivity spectrum of surface seismic data; an important question being whether the seismic data has sufficiently high frequency content to allow one to directly make inferences regarding thin-bedding using high-resolution seismic data through spectral decomposition and peak frequency analyses. This chapter discusses the spectral decomposition analysis completed on the 2D high-resolution seismic line. The objective of this analysis was to determine if thin-bed facies such as channel-fill and distal levee packages identified in core and on high resolution borehole image logs could be identified on the high-resolution seismic line. If these facies could be identified and characterized on the seismic line at the known well location, then inferences potentially could be made throughout the seismic line regarding the thin-bed facies.

PREVIOUS STUDIES USING 2D HIGH-RESOLUTION SEISMIC DATA IN DEEP-WATER ENVIRONMENTS

Badalini et al. (2000) used high-resolution seismic data (100-600 hertz) to improve their understanding of deeply buried turbidite systems. Their study was in the late Pleistocene Brazos-Trinity turbidite system on the northern Gulf of Mexico continental slope. The authors found that on the seismic data each onlap-fill succession consisted of alternating chaotic/transparent deposits (debris flows, slumps, and muddy and sandy turbidites) and layered deposits (turbidite fans and a channel levee complex). Beaubouef and Friedmann (2000) studied the late Pleistocene intra-slope basin system in the western Gulf of Mexico. One dataset that the authors used was high-resolution 2D seismic with peak frequency of 145 hertz. The seismic stratigraphy and facies that were found in this basin system were mass transport complexes, distributary channel-lobe complexes, leveed-channel complexes, and hemipelagic drape complexes.

PREVIOUS WORK USING SPECTRAL DECOMPOSITION

Chakraborty and Okaya (1995) discuss several different wavelet-based methods of frequency-time decomposition of seismic data. The methods that the authors investigated were short time Fourier transform (STFT), continuous wavelet transform (CWT), and matching pursuit decomposition (MPD). All of these methods were used to analyze a synthetic seismogram and it was found that the MPD resulted in the best detection of reflections. Spectral decomposition was used along with coherency to image deep (10,000 ft) Pennsylvanian age incised valleys in the Anadarko Basin, Oklahoma (Peyton et al, 1998). The spectral decomposition technique used the discrete Fourier transform to image time thickness variability. The spectral decomposition analysis of the 3-D seismic data helped identify the incised valley edges and internal features. Partyka et al. (1999) used spectral decomposition, specifically discrete Fourier transforms, to map and image bed thickness and lateral geologic discontinuities such as channel sands and complex fault systems over 3-D seismic surveys. Marfurt and Kirlin (2001) investigated thin-bed tuning attribute analysis using seismic spectral decomposition. The authors developed a suite of single and multitrace attributes to better map internal changes in thin-bedded reservoirs. Castagna et al. (2003) discuss the implementations of different spectral decomposition methods. The authors compare instantaneous spectral analysis (ISA) to other spectral decomposition methods as well as provide examples of ISA to detect low-frequency shadows beneath gas reservoirs in the northwest shelf of Australia and the Gulf of Mexico regions.

SPECTRAL DECOMPOSITION ANALYSIS

The objective of the spectral decomposition analysis was to evaluate frequency behavior for different depositional environments such as channel-fill and distal levee deposits using spectral decomposition. The spectral decomposition method used to analyze the 2-D high-resolution seismic line was the instantaneous spectral analysis (ISA) method. The ISA method provides a frequency spectrum for each time sample of a trace (Castagna et al, 2003). This method combines aspects of both Fourier based methods and wavelet based methods such as Mallat's matching pursuit decomposition.

The ISA method requires the seismic data to be migrated and stacked. There are three steps to this method, as outlined in Castagna et al. (2003). The first step is to take the migrated seismic section and decompose it into the constituent wavelets by using matching pursuit decomposition. The second step is to take the Fourier spectra of the individual wavelets in the time-frequency domain and sum them to produce "frequency gathers." These frequency gathers show the spectral behavior of one trace from the migrated section at all the decomposed frequencies. The last step is to sort these gathers into common or constant frequency sections, which produce cubes of spectrally decomposed data for a 2D line. These cubes can then be sliced to create time and horizon slices, and can be navigated just like any conventional 3D survey. The results can then be viewed as animated movies in interpretation software such as Seismic Micro-Technology's 2d/3d Pak™.

The high-resolution seismic line was run using the ISA method and then was imported into Seismic Micro-Technology's 2d/3d Pak™ and set up as a project. There were three files resulting from the ISA analysis: the INSPECT™[1] file, the overlay file, and the residual file. The INSPECT™ file contains the frequency decomposition information. Since this was one 2-D seismic line, there were two possible ways to display the data, either as a frequency gather or frequency panel. A frequency gather takes a single trace from the seismic and shows the frequency characteristics at that given trace. The other display used in the ISA method is to show how the entire seismic section behaves at a single frequency. This type of display is called a frequency panel.

The 2-D high-resolution seismic line had 329 common depth points (CDP) and 1 second of data. The INSPECT™ analysis was decomposed into 400 frequencies from 1 to 400.

Different automatic gain controls (AGC) were tried on the frequency gathers to boost and average the frequencies over the 0.3 millisecond window. The AGC parameters tried were 0.5 ms, 0.75 ms, and 1.0 ms and it was also run without AGC. The AGC used was 1.0 ms because it allowed the best balance of the frequencies throughout the seismic section.

[1]Trademark of Fusion

The Central well (Figure 1.2) was chosen for the spectral decomposition analysis because (1) it had more facies packages than the North well and (2) from previous research (Spang, 2000) it was known exactly where the Central well intersected with the seismic line. In addition, from a previous discussion (Slatt, 2001) it was known where the channel-fill and distal levee packages occurred on the seismic line at the location of the Central well. This particular wellbore was projected to the high-resolution seismic line by Spang (2000). The well location was identified on the seismic line as CDP 80.

The next step in determining if channel-fill and distal levee deposits could be distinguished using this method on a 2D high-resolution seismic line was to transfer the six horizons (two channel fill deposits, and four distal levee deposits) onto the seismic data where the well location is projected onto the seismic (Figure 6.1). Once the interpretation was on the seismic line at the well location, further interpretation was made to all of the CDPs and the other frequency panels.

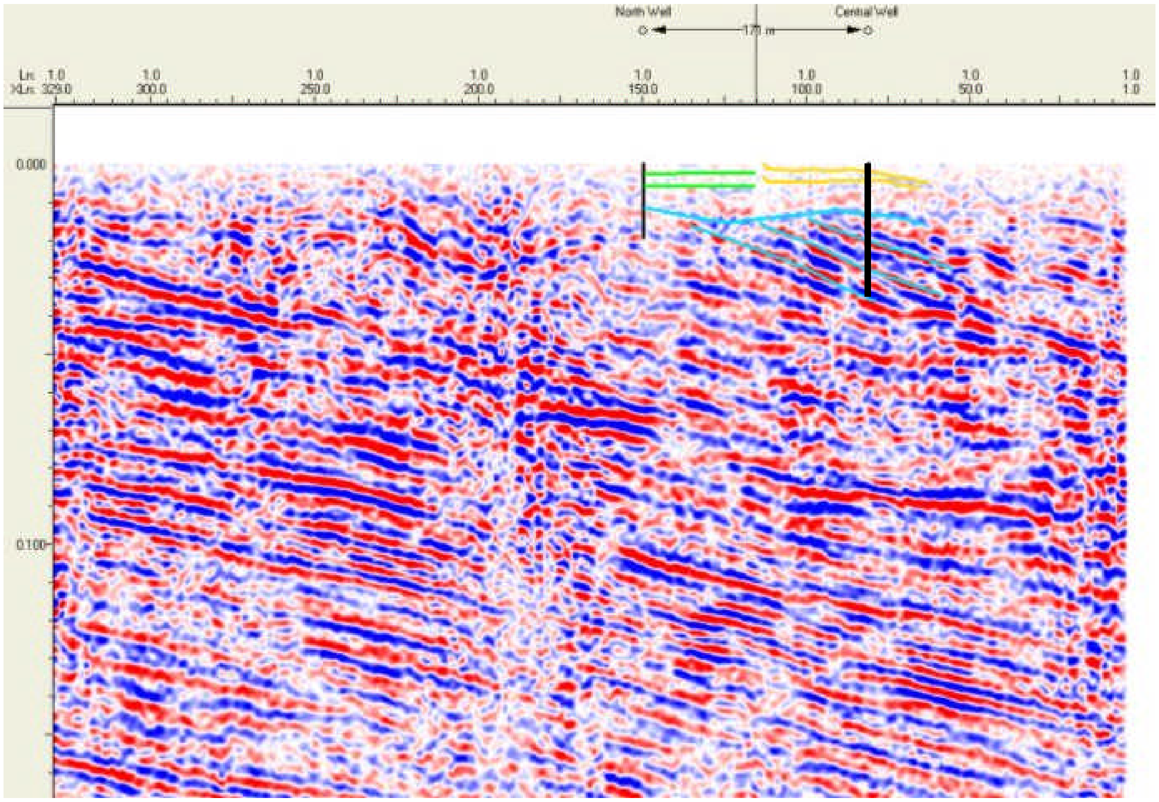

Figure 6.1. Seismic section showing well locations and horizons shown in different colors are proximal levee, channel-fill and distal levee deposits. From the top to the bottom of the figure, the green lines are the proximal levee horizons, the yellow lines are the channel-fill horizon, and the blue lines are the distal levee horizons.

Distinguishing between a frequency pattern of channel-fill and distal levee packages was the objective; however, a comparison of the frequencies at CDP 80 to the other CDPs along the seismic line resulted in inconclusive results (Figures 6.2, 6.3, and 6.4). There were no distinctive frequency signatures for either the channel-fill or the distal levee packages. The figures (6.2, 6.3, and 6.4) show that there is no specific frequency range with high amplitude for each depositional package. The figures show that there is lateral variation in frequency amplitudes among the CDPs which further demonstrates that a particular frequency range is not characteristic of a given depositional package. In this case, a larger volume of seismic data potentially could have been more helpful to distinguish between the two sedimentary packages. There are limitations to the data set since it is a single two-dimensional seismic line which limits the amount of information that can be extracted.

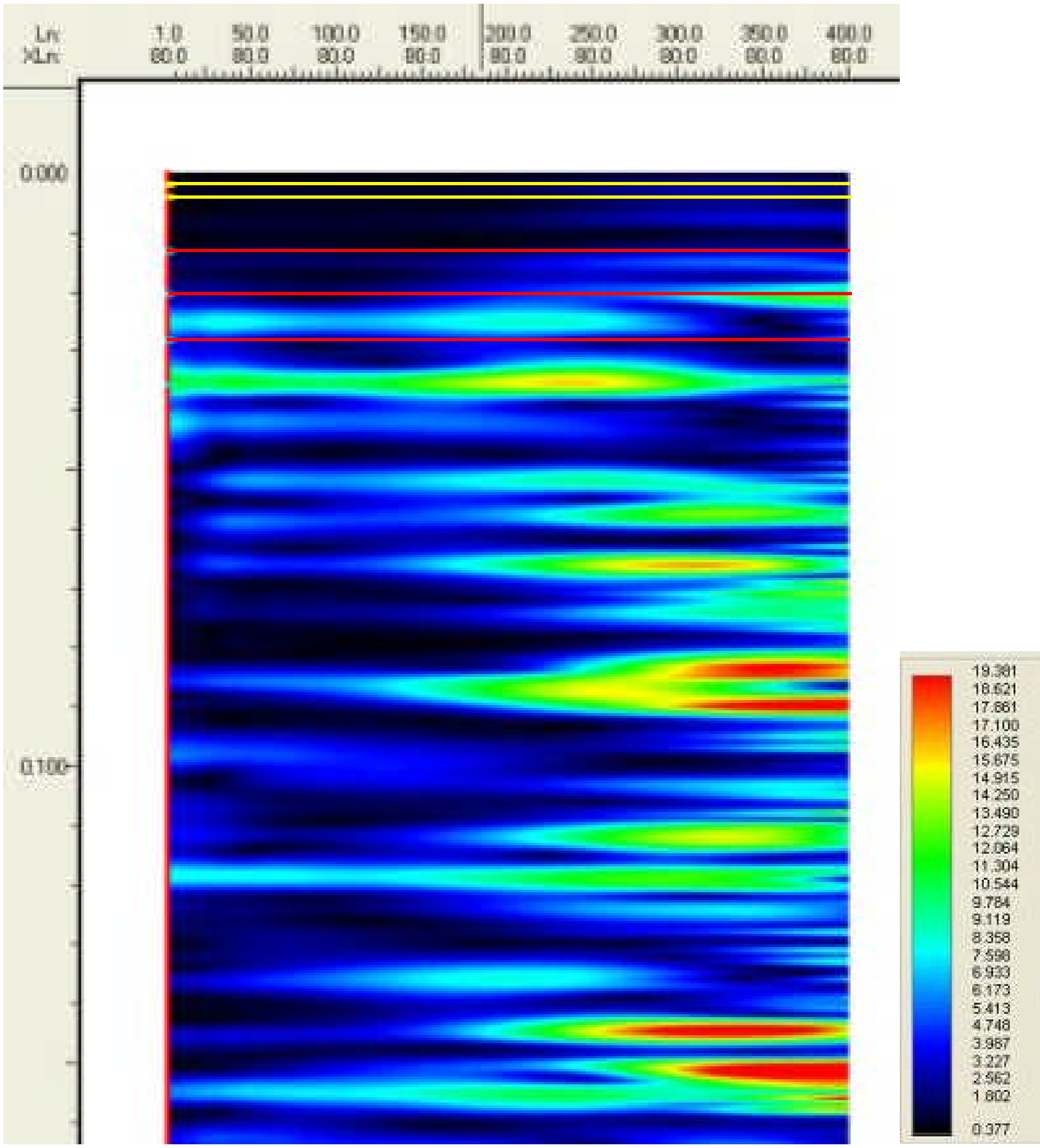

Figure 6.2. Frequency gather at the well location (CDP 80) showing the frequency distribution of the marked horizons (yellow horizontal lines are the channel-fill and the red horizontal lines are the distal levee packages). The horizontal axis is frequency, the vertical axis is time, and the color indicates the amplitude of a specific frequency at a given point.

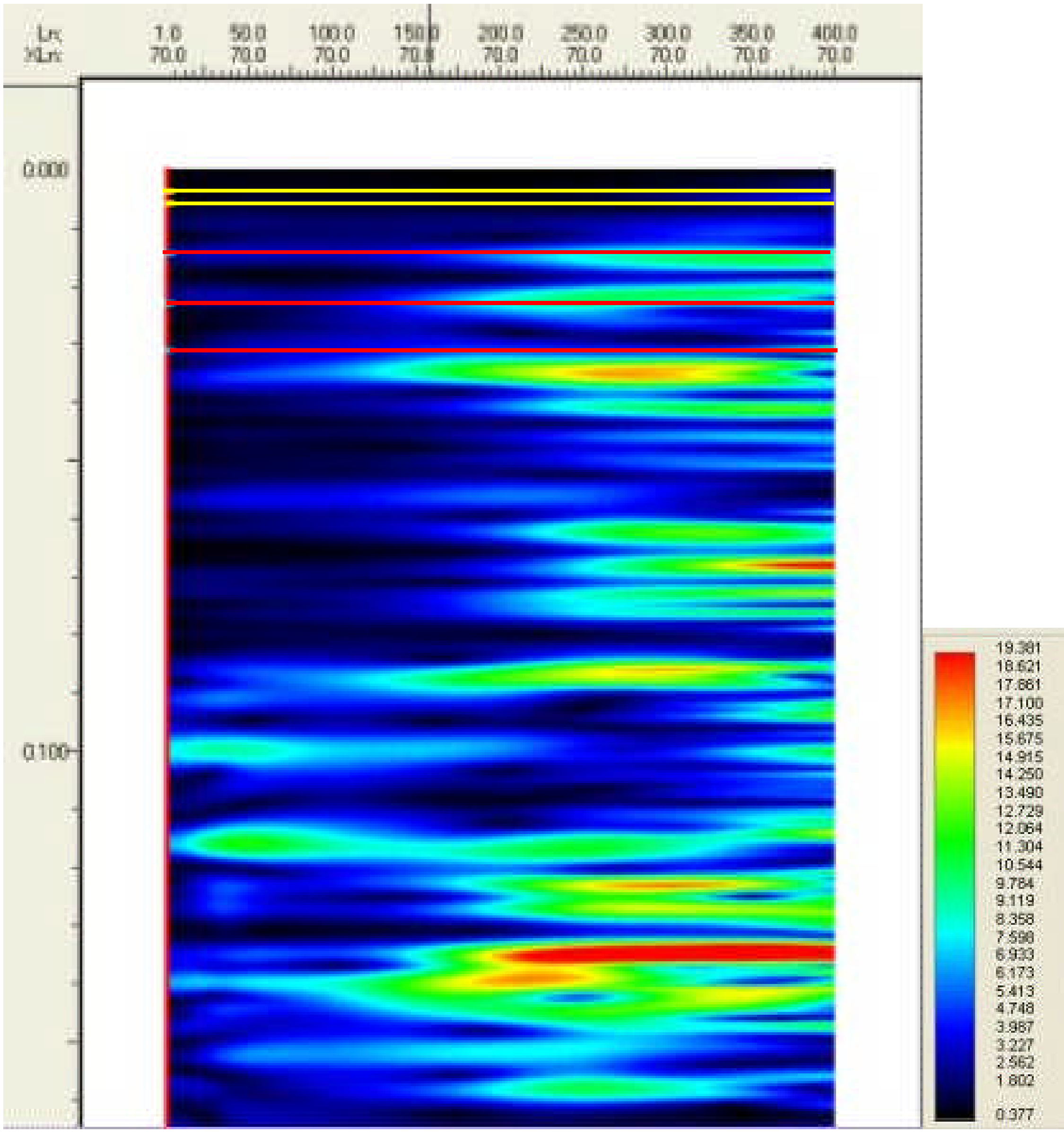

Figure 6.3. Frequency gather at the well location (CDP 70) showing the frequency distribution of the marked horizons (yellow horizontal lines are the channel-fill and the red horizontal lines are the distal levee packages). The horizontal axis is frequency, the vertical axis is time, and the color indicates the amplitude of a specific frequency at a given point.

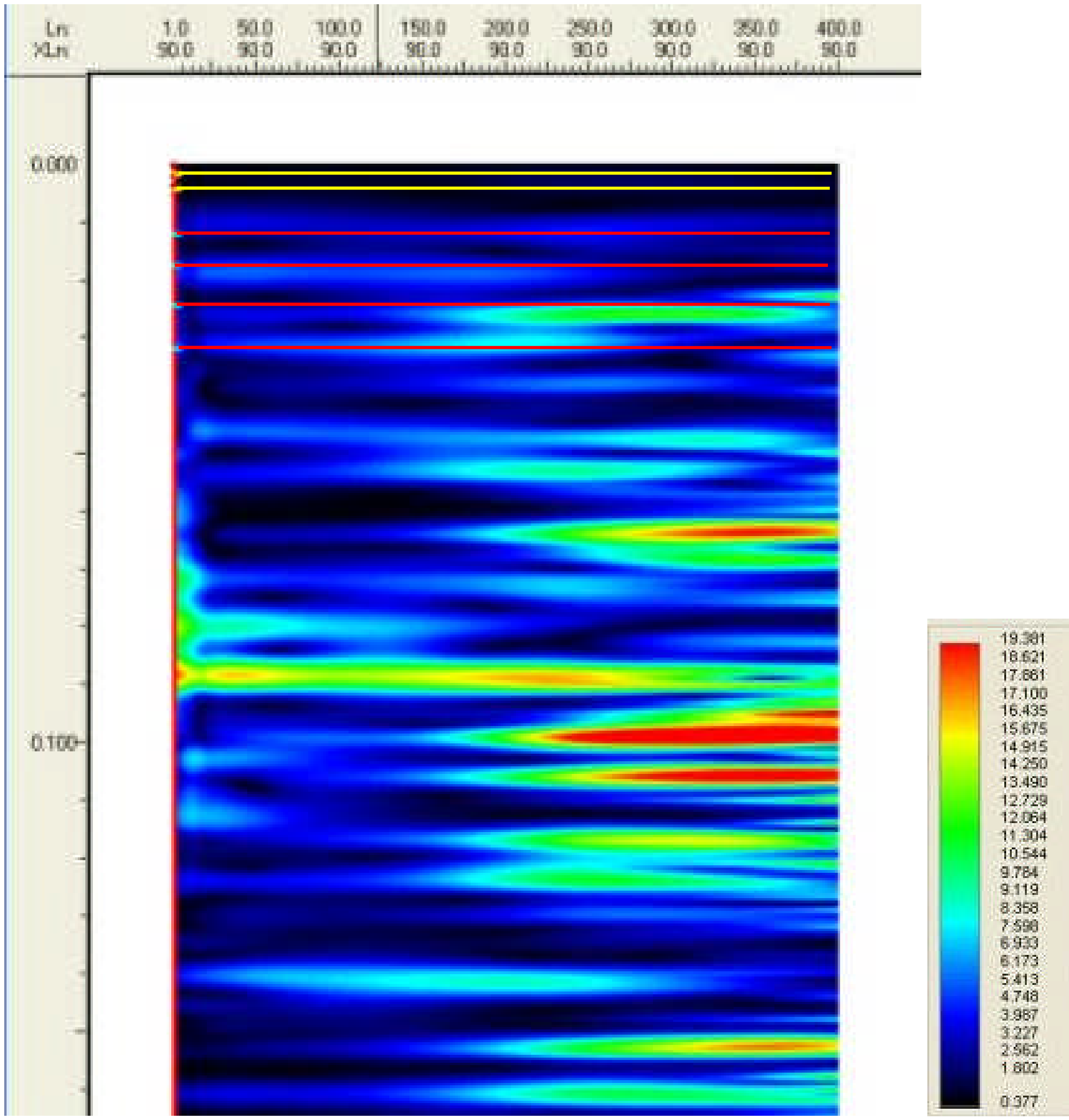

Figure 6.4. Frequency gather at the well location (CDP 90) showing the frequency distribution of the marked horizons (yellow horizontal lines are the channel-fill and the red horizontal lines are the distal levee packages). The horizontal axis is frequency, the vertical axis is time, and the color indicates the amplitude of a specific frequency at a given point.

There is lateral variation in frequency spectra between CDP 70 to CDP 90. The distance from CDP 70 to 90 is 50 meters which could cause the frequency spectra difference. The variation in frequency spectra among the CDPs could be a result of changes in bed thickness (Marfurt and Kirlin, 2001).

After using the high-resolution seismic line to investigate whether the spectral decomposition analysis could distinguish between the thin-bedded depositional packages, further investigation was warranted using the high-resolution seismic line. The next chapter investigates peak frequency versus bed thickness analysis using the high-resolution seismic line.

CHAPTER 7. PEAK FREQUENCY AND BED THICKNESS ANALYSIS OF SEISMIC LINE

This chapter discusses using peak frequency versus bed thickness relationships to analyze the 2D high-resolution seismic line. The objective of this analysis was to enhance the seismic data to determine if thin-bed facies such as channel-fill, proximal, and distal levee packages identified in core and on high resolution borehole image logs could be identified on the high-resolution seismic line.

BACKGROUND ON PEAK FREQUENCY VERSUS BED THICKNESS

Peak frequency versus bed thickness analysis is a new technique used on seismic data that is based on the spectral decomposition methods and results discussed in Chapter 6. This new technique extends the spectral decomposition method to analyze the peak frequencies and peak amplitudes with respect to bed thickness. In the frequency domain, peak frequency is defined as the frequency with the maximum amplitude. Peak frequency information is obtained from the spectral decomposition frequency gathers. Peak frequency and peak amplitude are evaluated versus bed thickness. One criterion for this technique is that thickness of the beds has to be less than the tuning thickness of the bed.

In previous work (Tirado, 2004), two sands were studied using real seismic data and modeling to determine the relationship between peak frequency and bed thickness. The first sand had an average thickness of 40 ft which was less than the tuning thickness of 66 ft for the sand. Most of the individual sand thicknesses were less than the tuning thickness for this sand. The peak frequencies for the sands ranged from 18 to 32 hertz. The sand was modeled as a basic wedge sand. The results from the modeled data indicate that for this sand, the peak frequency increases with bed thickness so long as the bed thickness is less than the tuning thickness. More modeling was done since real seismic and modeled results for this sand were similar. The second sand investigated through real seismic data and modeling had a tuning thickness of 63 ft, however, 8 out of the 9 sands had bed thicknesses greater than the tuning thickness. The real seismic data and the modeling of this sand did not indicate a relationship between peak frequency and bed thickness. The lack of relationship for this particular sand could be a result of the sand thicknesses being greater than the tuning thickness.

Additional modeling using the peak frequency and amplitude spectrums were conducted on the sand where the real seismic and modeled results were similar (Tirado, 2004). The frequency characteristics of the sand were modeled using the frequency domain impulse response of Green's function. Green's function can be written in the frequency domain as:

$$G(f) = [r_1\cos(2\pi f t_1) + r_2\cos(2\pi f t_2)] + i\,[r_1\sin(2\pi f t_1) + r_2\sin(2\pi f t_2)] \qquad (5.1)$$

where r_1 is the reflection coefficient of the top of a bed, r_2 is the reflection coefficient of the bottom of a bed, t_1 is the two-way time to the top of the bed, t_2 is the two-way time to the bottom of the bed, and f is the frequency.

The amplitude spectrum of a wavelet can be found by convolving the amplitude spectrum for the reflectivity series and the amplitude spectrum for a Ricker wavelet (Chung and Lawton, 1995). Thus, using Green's function in the frequency domain, the amplitude spectrum can be written as

$$A(f) = \sqrt{[r_1 \cos(2\pi f t_1) + r_2 \cos(2\pi f t_2)]^2} + \sqrt{[r_1 \sin(2\pi f t_1) + r_2 \sin(2\pi f t_2)]^2} \qquad (5.2)$$

The Ricker wavelet has the amplitude spectrum in terms of peak frequency (f_o) as:

$$A_R(f) = \left(\frac{f}{f_o}\right)^2 e^{-\left(\frac{f}{f_o}\right)^2} \qquad (5.3)$$

In the frequency domain, convolving is done by multiplying the two equations. Multiplying equations 5.2 and 5.3 and setting the derivative equal to 0 would give the peak frequency. The new equation is:

$$F_p = [r_1^2 + r_2^2 + 2\, r_1 r_2 \cos(2p\, f_p T)]^* \ [1-(f_p/f_o)^2] \qquad (5.4)$$

where f_p is the peak frequency, r_1,r_2, T, and f_o are the variables as defined above.

This equation is called the exact equation for peak frequency (Chung and Lawton, 1995). The exact equation (5.4) was used by Tirado (2004) to model the peak frequency response for different Ricker wavelets. The results of this equation were the same for the real seismic and the modeled results. The modeling indicates that with higher initial peak frequencies the distinction between frequencies for each thickness becomes greater. This was also observed by Chung and Lawton (1995). Thus, the higher the input frequency the more likely peak frequency can be used to distinguish bed thickness.

Widess (1973) investigated the reflective behavior of thin beds. He studied a perfectly odd impulse pair and found that thin beds have a thickness less than about one-eighth of a wavelength ($\lambda/8$). In addition, the character of a reflection is indistinguishable for beds less than $\lambda/8$. He found that a bed that is thin for one frequency is not necessarily thin for a higher frequency. Widess states that the amplitude of the reflection is approximately proportional to the thickness of the bed. The reflections for beds about $\lambda/8$ and less in thickness can not be resolved.

Tirado (2004) further explored Widess' work on thin beds. The author modeled a sand from the Gulf of Mexico region and found that peak frequencies changed once the bed thicknesses were less than about one-eighth of a wavelength ($\lambda/8$) which contradicts Widess' previous theory. The reflection coefficient for this sand was decomposed into the even and odd parts of the impulse response. Equation 5.4 was applied to both the even and odd impulse response. The results from this equation are similar to the theoretical values; however, the even part of the impulse response dominates the peak frequency for very thin beds. So, the amplitude of the wavelets for each of the even and odd impulse responses were plotted for each thickness. The odd part of the impulse response for the amplitude goes to zero as the sand decreases in thickness and the even part of the amplitude shows thickness decreases until the tuning thickness. This indicates that the amplitude contribution of the odd part at very thin beds is very small and the even part of the amplitude has more influence over the character of the peak frequency response.

The techniques discussed in Tirado (2004) demonstrate the importance of analyzing peak frequency versus bed thickness. Recently developed technologies for analyzing seismic data in the frequency domain, such as spectral decomposition, have led to advances in stratigraphic interpretation. Applying this technology of evaluating peak frequency versus bed thickness can be used to enhance thin bed detection on seismic reflection data. The result could potentially produce enhanced seismic sections with the potential to show more clearly-defined thin beds.

The research discussed in this section leads to the possibility of investigating thin beds on seismic data using peak frequencies and even reflection coefficient impulse pairs. Due to the improved understanding of the importance of even impulse pairs, thinner beds can be detected than could be detected previously. As higher frequency seismic data becomes available, even thinner beds can be detected.

PEAK FREQUENCY VERSUS BED THICKNESS ANALYSIS AND RESULTS

Peak frequency versus bed thickness analysis was conducted on the 2D high-resolution seismic line to enhance the seismic character of the thin beds. The results of the spectral decomposition of the seismic data were the input data for the peak frequency versus bed thickness analysis. The results of the spectral decomposition analysis are discussed in Chapter 6. The original high-resolution seismic line served as the input data for this analysis (Figure 7.1).

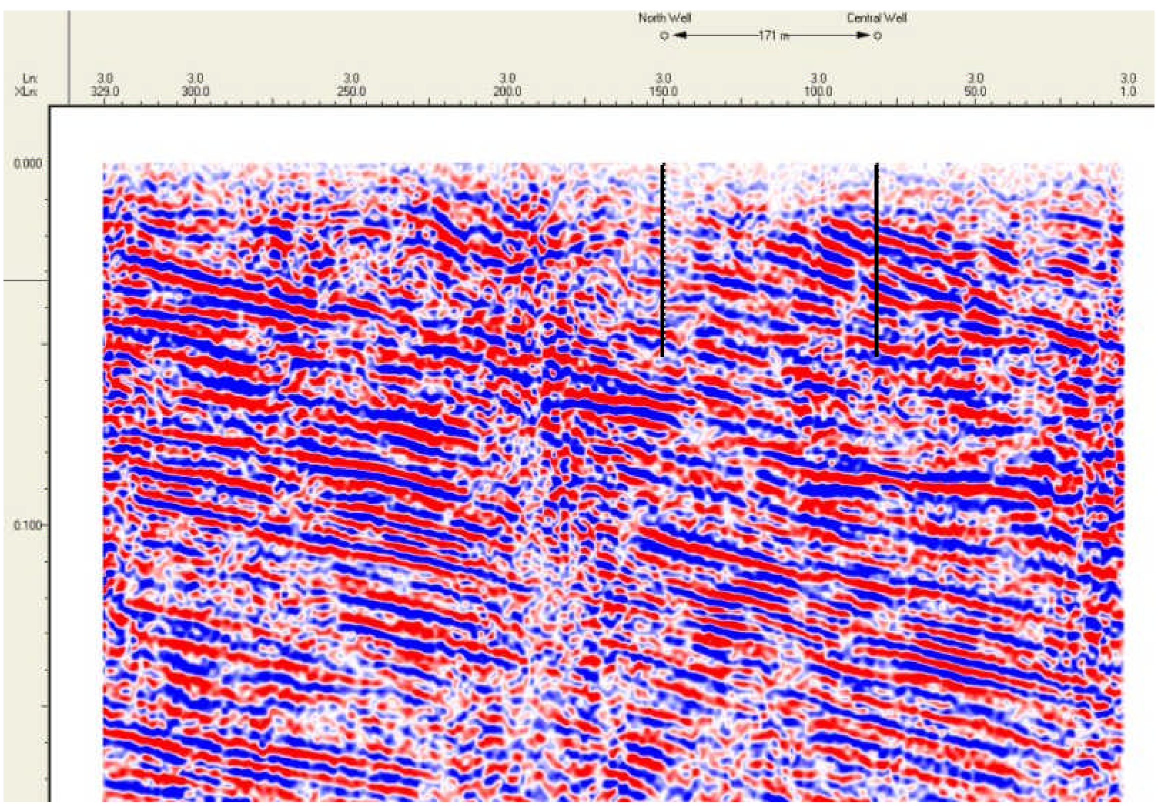

Figure 7.1. The original high-resolution seismic line.

A synthetic seismogram was created to provide a good tie between the original high-resolution seismic line to the North well. A synthetic was created only for the North well since no logs were available for the Central well. No checkshot survey was available for the North well so a time-depth curve was created using the Pukearhue sonic log. The resistivity and density logs from the North well were imported into the Kingdom™[1] software package and used to create the synthetic. A Ricker wavelet with a frequency of 150 hertz was used to tie the synthetic to the seismic (Figure 7.2).

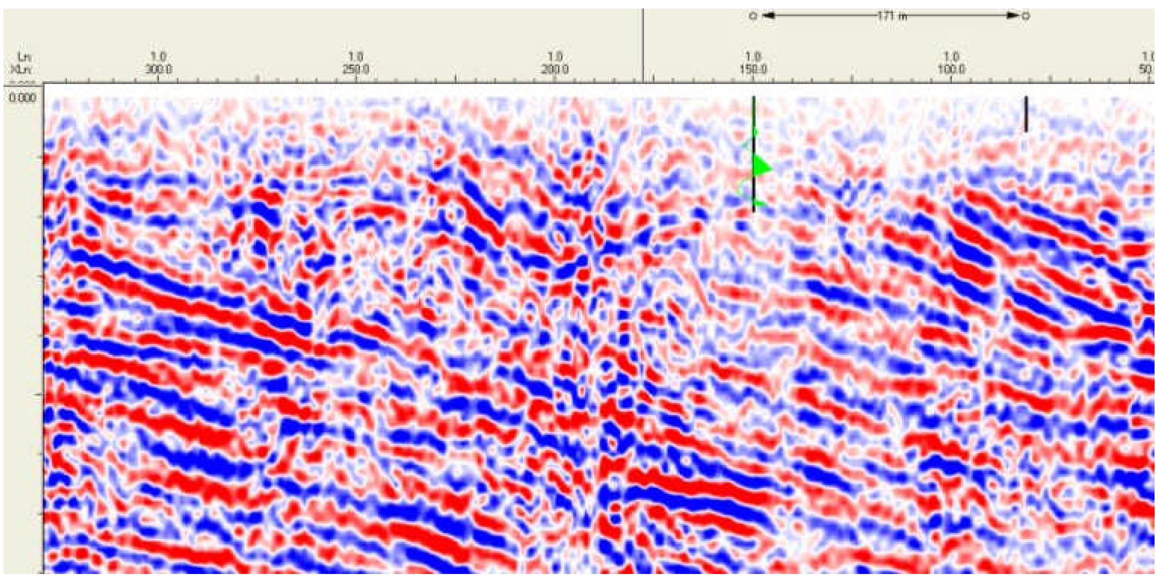

Figure 7.2. High-resolution line with the synthetic superimposed.

The peak frequency versus bed thickness analysis enhanced the original seismic line (Figure 7.3). This analysis provided a clearer picture of the seismic data along with enhancing some reflectors. This enhanced seismic section allowed for a more precise

[1] Trademark of Seismic Micro-Technology

interpretation. Figure 7.4 illustrates the comparison of the original seismic data to the peak frequency versus bed thickness analysis.

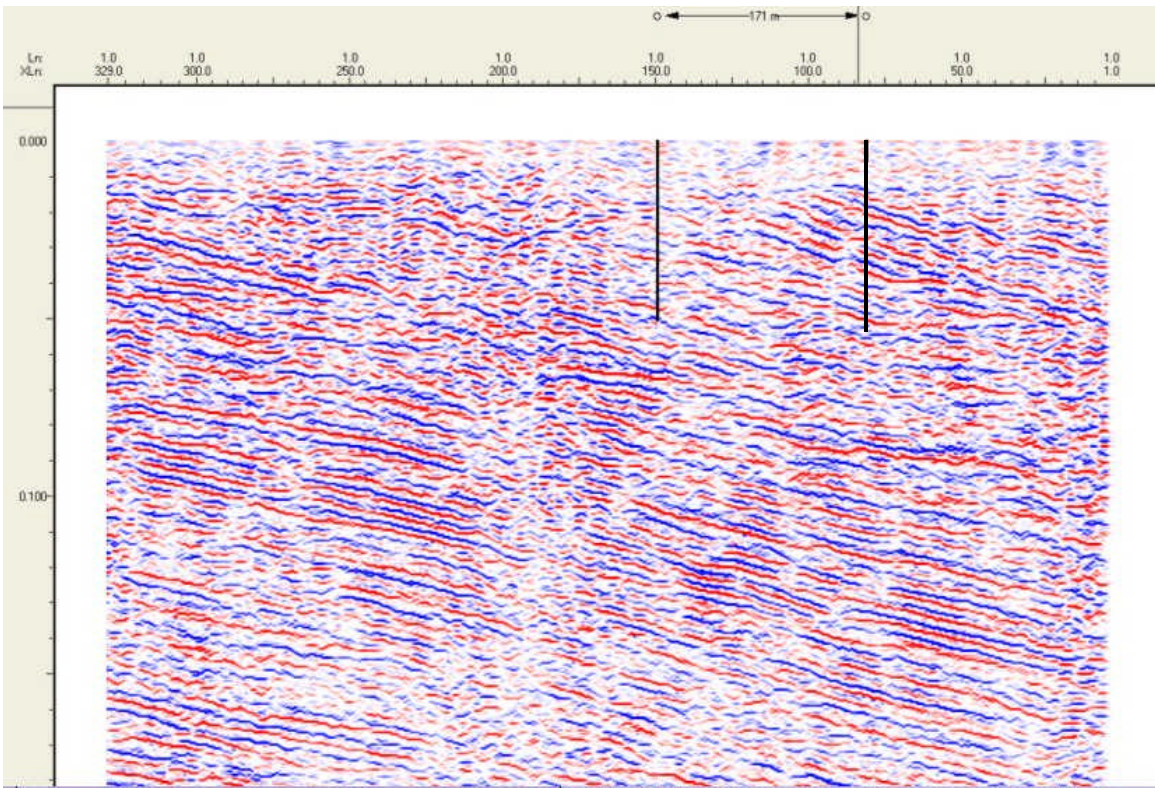

Figure 7.3 Seismic line with peak frequency versus bed thickness analysis.

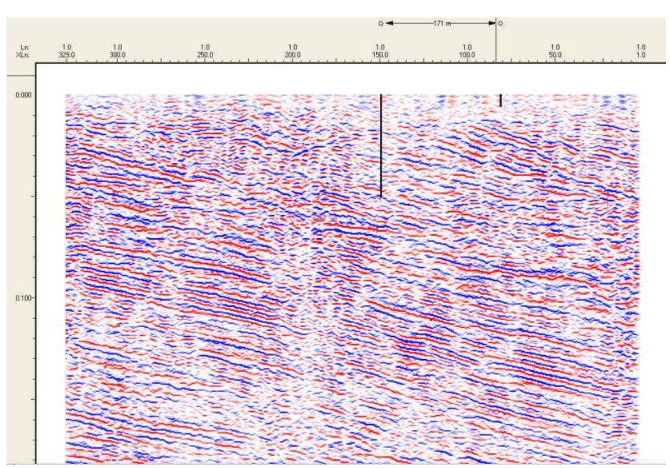
A

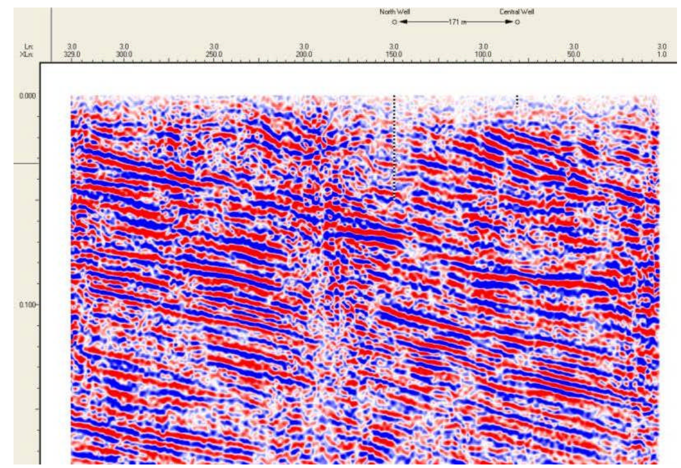

B

Figure 7.4 Comparison of the peak frequency versus bed thickness (A) to the original high- resolution seismic data (B).

Since an enhanced seismic section was available to aid in detecting the thin beds, a depositional model was generated using the modified Fischer plots from both the North and Central wells. The depositional environment data for the North and Central wells was obtained from Spang (2000), who identified the proximal levee, distal levee, and channel-fill deposits. The depositional environment information was used to generate the depositional model on the peak frequency versus bed thickness seismic line and the high-resolution seismic line (Figures 7.5, 7.6, 7.7 and 7.8). The peak frequency versus bed thickness seismic section provided better data for interpretation. The reflectors were more continuous in the peak frequency versus bed thickness section which aided in the interpretation. The original high-resolution seismic line had several chaotic, patchy areas that were cleared up after the peak frequency versus bed thickness analysis was performed.

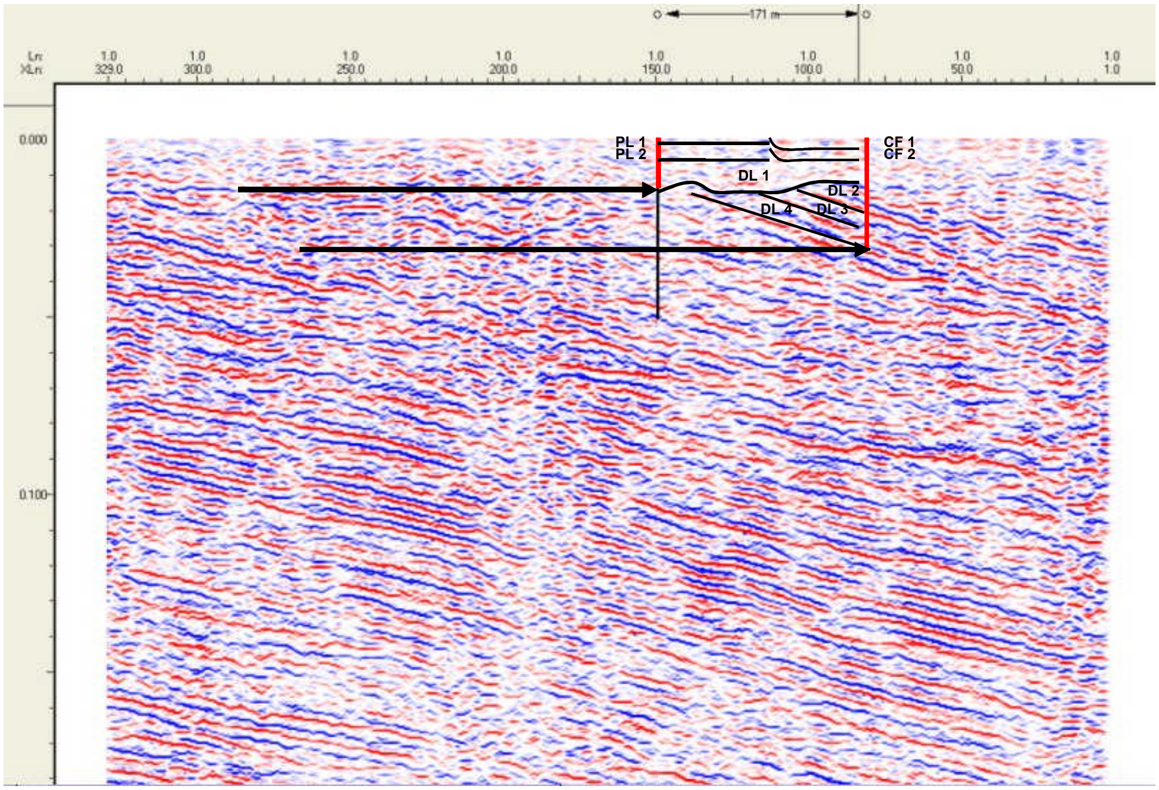

Figure 7.5. Peak frequency versus bed thickness seismic line with depositional model. Key for depositional environments: CF = channel-fill, PL= proximal levee, and DL= distal levee.

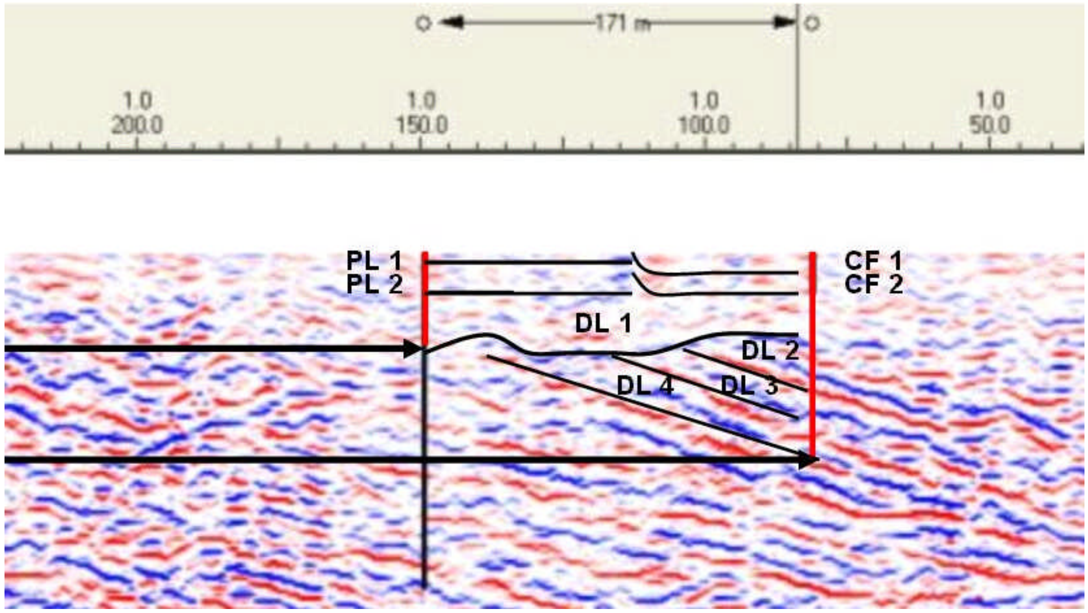

Figure 7.6. Peak frequency versus bed thickness seismic line with depositional model. Key for depositional environments: CF = channel-fill, PL= proximal levee, and DL= distal levee.

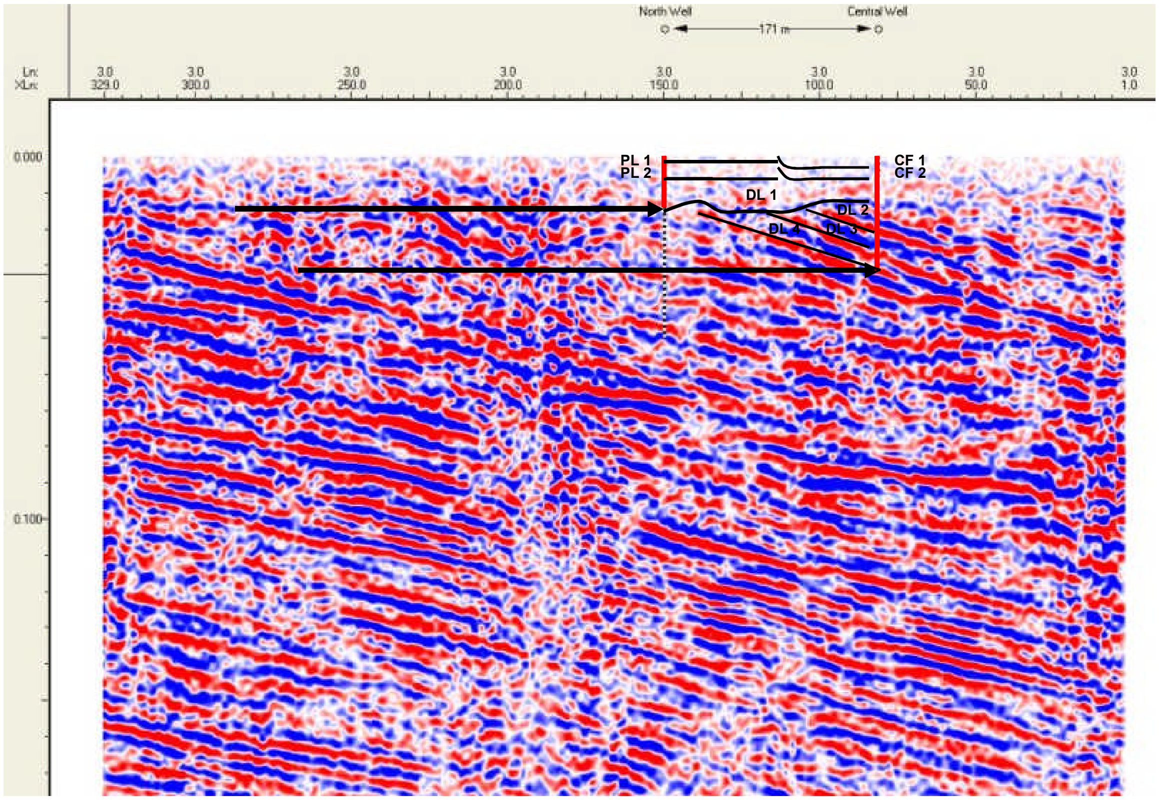

Figure 7.7. Original seismic line with depositional model. Key for depositional environments: CF = channel-fill, PL= proximal levee, and DL= distal levee.

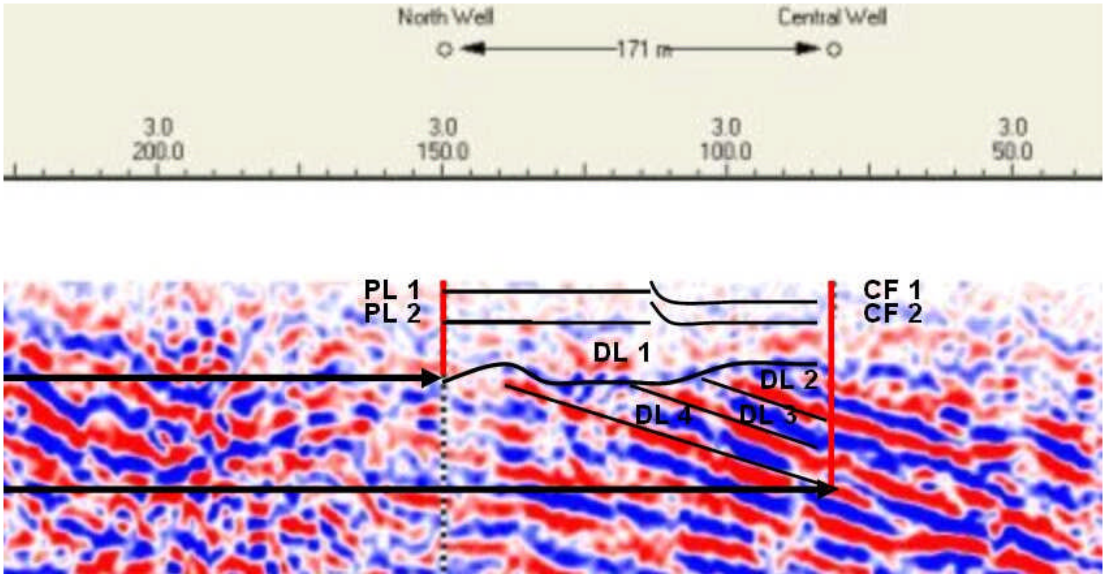

Figure 7.8. Original seismic line with depositional model. Key for depositional environments: CF = channel-fill, PL= proximal levee, and DL= distal levee.

The peak frequency versus bed thickness analysis provided an enhanced seismic section. The enhanced section allowed for a better interpretation of thin bed strata. The depositional model provides the interpretation of the channel-fill, proximal, and distal levees and the extent of the depositional environments between the North and Central wells.

CHAPTER 8. CONCLUSIONS AND DISCUSSION

There are three distinct parts to this dissertation: (1) develop a bed boundary detection algorithm, (2) using the results of the automatically generated bed boundary detection algorithm to determine the vertical distribution of some rock properties, and (3) to determine if thin-bedded intervals can be characterized on a seismic line using a spectral decomposition technique.

The bed boundary detection algorithm technique proved to be powerful for evaluating the geological and geophysical parameters investigated. Various geological and geophysical parameters were detected using one microresistivity curve from the borehole image log. Bed boundaries were detected using a sliding window algorithm on one curve from one pad. This technique allowed the sandstone/shale boundaries to be distinguished and the picking of bed boundaries to become more time efficient and less subjective. The bed boundary results were usable and often times were used as the input data in the calculation of subsequent parameters.

The background noise was successfully filtered using a threshold technique on the sliding window method results. The threshold method results were used in generating Modified Fischer plots for each threshold value. The different Modified Fischer plots vary greatly with threshold, thus leading to different stratigraphic interpretations. The larger threshold values eliminated some important geologic information.

Attempts at eliminating the threshold effect included calculating mean thickness and standard deviation of bed boundary thicknesses. These parameters did not result in removing the threshold effect; however, the mean thickness plots provide information about the stratigraphic thinning and thickening of the beds.

The Modified Fischer plot with zero threshold closely resembled Spang's (2000) manually computed one from the same dataset. This suggests that a threshold was not generally needed for bed boundary detection and the bed boundary picking algorithm, though simple, appears to be a very powerful tool.

Hurley (1996) suggests that generating modified Fischer plots would provide a quick look at the thinning and thickening trends of sediments on a larger geologic scale with more wells. The automated bed boundary detection and modified Fischer plot techniques in this dissertation will provide a faster and less subjective approach for determining the stratigraphic thinning and thickening trends of sediments on a larger geologic scale.

Estimating anisotropy versus threshold indicated that the anisotropy was only slightly affected by the number of bed boundaries. The different velocity values used in the anisotropy estimations did not show a significant change in anisotropy for the low and high velocity values. The difference between the low and high elastic moduli constants was a scalar change. Due to the low velocity values being half of the high velocity values, such a scalar change was expected. The elastic moduli constants L, M, and S were slightly affected by the threshold values when analyzing the entire well as a whole.

The elastic moduli constants L, M, and S were also affected by the threshold values when only analyzing the proximal levee deposits but not when only analyzing the distal levee deposits. Thus, the elastic moduli constants could be used to help differentiate between the proximal and distal levee deposits. The lab calculated anisotropy values exhibited no change in elastic constants and only showed a 1% change in elastic constants L, M, and S for the proximal levee deposits. There is less variation in the lab calculated anisotropy results since these used more detailed measurements (both saturated and unsaturated samples) from the study area. The Vp/Vs relationships derived from the core data justified the use of Vp/Vs relationships used to calculate the anisotropy. For the most part, the velocities did not indicate change for the lab data except in the distal levee deposit where the $V_{P,v}$ value at threshold 100 deviated from the $V_{P,h}$ value.

Seismic anisotropy caused by the fine layering is small and independent of the scale of the layering. This is not what is generally assumed. It is generally believed that layers do not become less effective in generating large-scale anisotropy as they become thinner (Backus 1962). Backus (1962) also states it is possible that layers too thin to be observed by conventional well logs are present and could contribute to the large-scale anisotropy of the crust. In this research, thin beds as thin as 1 cm were detected by the borehole image log. The results from this research indicate that geological and geophysical thin beds do not contribute to large-scale anisotropy. Therefore, from this research it was determined that seismic anisotropy is independent of the scale of the layering.

The well log spectral results did not suggest that there was a distinction between the proximal and distal levee deposits and therefore suggest that these results were not dependent on depositional environment.

The characterization of the thin beds on seismic using the spectral decomposition technique did not provide the anticipated results. The seismic spectral decomposition analyses did not indicate a distinction of frequencies between the channel-fill and distal levee deposit. Therefore the seismic spectral decomposition results were not dependent on the depositional environment. These results are contrary to expectations. Several studies (Badalini et al., 2000; Beaubouef and Friedmann, 2000) using spectral decomposition techniques in deep-water environments on high-resolution seismic data were able to differentiate depositional facies. However, broader band seismic acquisition/processing could potentially lead to improved spectral decomposition and subsequent stratigraphic facies analysis.

Peak frequency versus bed thickness analysis was performed on the high-resolution seismic data. The analysis enhanced the seismic section which allowed for an easier interpretation. This analysis has great potential as an excellent interpretation tool.

The techniques used in this research provide for potential applications to upscaling. The automated bed boundary detection algorithm could be used to generate Modified Fischer plots in an area with multiple wells. The Modified Fischer plots could be tied to the seismic data via conventional well log data and then trends of thinning and thickening of sediments could be identified on the seismic. Additional information such as the depositional environment could be identified on the seismic data with the use of the borehole image log and conventional well data as discussed in this chapter. By upscaling, a more regional picture could be defined.

Techniques in this research proved to be powerful and effective while other techniques were contradictory to results of previous work. The bed boundary algorithm, threshold analyses, and adjusted mean thickness results were positive and reinforced the validity of these newly developed techniques. Analyses such as estimating anisotropy, well log spectral, and spectral decomposition techniques led to unanticipated results and are contradictory to previously published research.

Studying the fine layering of thin bedded turbidites has revealed information that confirmed some of our pre-conceived notions but contradicted others. Therefore, continued studies of this kind should prove to be fruitful.

REFERENCES

Babuska, V. and M. Cara, 1991, Seismic anisotropy in the earth, Kluwer Academic Publication.

Backus, G. E., 1962, Long-wave elastic anisotropy produced by horizontal layering, Journal of Geophysical Research, 67, p. 4427-4440.

Badalini, G., B. Kneller, and C. Winker, 2000, Architecture and processes in the late Pleistocene Brazos-Trinity turbidite system, Gulf of Mexico continental slope, GCSSEPM Foundation 20th Annual Research Conference, p.16-34.

Beaubouef, R. T. and S. J. Friedmann, 2000, High resolution seismic/sequence stratigraphic framework for the evolution of Pleistocene intra slope basins, Western Gulf of Mexico: Depositional models and reservoir analogs, GCSSEPM Foundation 20th Annual Research Conference, p. 40-60.

Browne, G. H. and R. M. Slatt, 2002, Outcrop and behind-outcrop characterization of a late Miocene slope fan system, Mt. Messenger Formation, New Zealand, AAPG Bulletin, v.86, No. 5, p.841-862.

Browne, G. H., R. M. Slatt, and P. R. King, 2000, Contrasting styles of basin-floor fan and slope fan deposition; Mount Messenger Formation, New Zealand, AAPG Memoir, v. 72, p.143-152.

Browne, G. H., and R. M. Slatt, 1997, Thin-bedded slope fan (channel-levee) deposits from New Zealand: An outcrop analog for reservoirs in the Gulf of Mexico, Gulf Coast Association Geological Society Transactions, v.47, p.75-86.

Castagna, J. P., 2004, Personal communication.

Castagna, J. P, S. Sun, and R. W. Siegfried, 2003, Instantaneous sprectral analysis: Detection of low-frequency shadows associated with hydrocarbons, The Leading Edge, v. 22, n.2, p.120-127.

Castagna, J. P., 1999, AVO Analysis - Tutorial and Review, Offset-Dependent Reflectivity – Theory and Practice of AVO Analysis, ed. John P. Castagna and Milo M. Backus, p.3-36.

Castagna, J. P, M. L. Batzle, and T. K. Kan, 1999, Rock physics – The link between rock properties and AVO response, Offset-Dependent Reflectivity – Theory and Practice of AVO Analysis, ed. John P. Castagna and Milo M. Backus, p.135-171.

Castagna, J. P., M. L. Batzle, and R. L. Eastwood, 1985, Relationships between compressional-wave and shear-wave velocities in clastic silicate rocks, Geophysics, 50, no. 4, p. 571-581.

Charkraborty, A. and D. Okaya, 1995, Frequency-time decomposition of seismic data using wavelet-based methods, Geophysics, 60, no. 6, p. 1906-1916.

Chung, H. and D. Lawton, 1995, Frequency characteristics of seismic reflections from thin beds, Canadian Journal of Exploration Geophysics, v.31, p.32-37.

Coleman, Jr. J. R., et al., 1998a, An evaluation of outcrop analog development techniques for deep water sandstone reservoirs, AAPG Bulletin, v.82, No. 10, p.1902.

Coleman, Jr. J. L., et al., 1998b, Comparison of Two Miocene Turbidite Intervals: Taranaki Basin (New Zealand) and Gulf of Mexico (USA), Gulf Coast Association of Geological Societies Transactions, v.48, p.535.

Crampin, S., 1986, Anisotropy and transverse isotropy, Geophysical Prospecting, 34, p.94-99.

Doveton, J. H., 1994, Theory and applications of time series analysis to wireline logs, Geologic Log Analysis using Computer Methods.

Ekstrom, M. P., et al.1986, Formation imaging with microelectrical scanning arrays, Transactions of the SPWLA 27th annual logging symposium, Houston, June 9-13, p. BB.

Fillon, R. H., and P. N. Lawless, 2002, Deep-water depositional facies and reservoir quality evaluation based on Fourier analysis of gamma-ray logs, Gulf Coast Association of Geological Societies Transactions, 52, 267-275.

Fourier Transforms, DFTs, and FFTs, 2004, http://www.me.psu.edu/me82/Learning/FFT/FFT.html

Goolsby, S. M., R. M. Slatt, and N. F. Hurley, 2001, Core and borehole image log characterization of turbidite sandstones in the Lewis Shale, Green River basin, Wyoming, American Association of Petroleum Geologists Poster Presentation

Hansen, S. M., and T. Fett, 2000, Identification and evaluation of turbidite and other deepwater sands using open hole logs and borehole images, AAPG Memoir 72, p.317-338.

Hoffman, F., 2004, An introduction to Fourier theory, http://aurora.phys.utk.edu/~forrest/papers/fourier/#introduction

Hurley, N. F., 1996, Parasequence-Scale Stratigraphic Correlations in Deep-Marine Sediments using Borehole Images, GCSSEPM Foundation 17th Annual Research Conference, p. 147-152.

Jordan, D. W., D. J. Schultz, and J. A. Cherng, 1994, Facies architecture and reservoir quality of Miocene Mt. Messenger deep-water deposits, Taranaki Peninsula, New Zealand, GCSSEPM Foundation 15th Annual Research Conference, p. 151-166.

King, P. R., G. H. Browne, and R. M. Slatt, 1994, Sequence architecture of exposed late Miocene basin floor fan and channel-levee complexes (Mount Messenger Formation), Taranaki Basin, New Zealand, Submarine fans and turbidite systems: Gulf Coast Section SEPM 15th Annual Research Conference, p.177-192.

Marfurt, K. J. and R. L. Kirlin, 2001, Narrow-band spectral analysis and thin-bed tuning, Geophysics, 66, no. 4, p. 1274-1283.

Mavko, G, T. Mukerji, and J. Dvorkin, 1998**,** The Rock Physics Handbook: Tools for Seismic Analysis in Porous Media, Cambridge University Press, p.142-146.

McLaughlin, P., 2004, Introduction to Geophysical Logging, http://www.udel.edu/dgs/ftp/ppmcl/GEOL667%20Geophysical%20logging%20Q%20Env%20Micro%20F2003.pdf

Nye, J. F., 1957, Physical Properties of Crystals: Their Representation by Tensors and Matrices, Clarendon Press, Oxford.

Partyka, G., J. Gridley, and J. Lopez, 1999, Interpretational applications of spectral decomposition in reservoir characterization, The Leading Edge, 18, no. 3, p. 353-360.

Pavlovic, M. D., 1999, Thin-bed analysis using borehole image logs in the Northern Gulf of Mexico, South Texas Geological Society, v.39, No. 6, p.9-16.

Peyton, L., R. Bottjer, and G. Partyka, 1998, Interpretation of incised valleys using new 3-D seismic techniques: A case history using spectral decomposition and coherency, The Leading Edge, 17, no.9, p. 1294-1298.

Prokoph, A. and F. P. Agterberg, 2000, Wavelet analysis of well-logging data from oil source rock, Egret Member, offshore eastern Canada, AAPG Bulletin, 84, p.1617-1632.

Prokoph, A. and F. P. Agterberg, 1999, Detection of sedimentary cyclicity and stratigraphy completeness by wavelet analysis: An application to Late Albian cyclostratigraphy of the Western Canada sedimentary basin, Journal of Sedimentary Research, 69, 862-875.

Rampino, M. R., A. Prokoph, and A. C. Adler, 1999, Permian/Triassic boundary events; high-resolution stratigraphy based on fast-Fourier transform and wavelet analyses of Milankovitch-band cyclicity, Abstracts with Programs – Geological Society of America, 31, p. 439.

Robertson, J.D. and D. Corrigan, 1983, Radiation patterns of a shear-wave vibrator in near-surface shale, Geophysics, 48, 19-26.

Schlumberger, 1999, Flowchart of FMI Processing Chain

Schlumberger, FMI brochure, SMP-5822, April 2002.

Schlumberger, OBMI brochure, SMP-5806, June 2001.

Serra, O., 1989, Formation MicroScanner Image Interpretation: Houston (Schlumberger Educational Services), SMP-7028.

Sheriff, R.E., 2002, Encyclopedic dictionary of applied geophysics, Society of Exploration Geophysicists.

Slatt, R.M., 2004, Personal communication.

Slatt, R.M., 2001, Personal communication.

Slatt, R. M., D. W. Jordan, and R. J. Davis, 1994, Interpreting formation microscanner log images of Gulf of Mexico Pliocene turbidites by comparison with Pennsylvanian turbidite outcrops, Arkansas, GCSSEPM Foundation 15th Annual Research Conference, p.335-348.

Spang, R. 2000, Application of fullbore formation micro imager logs for evaluating thin-bedded turbidite strata, Masters Thesis, Colorado School of Mines.

Stephen, K. D., J. D. Clark, and A. R.Gardiner, 2001, Outcrop-based stochastic modeling of turbidite amalgamation and its effects on hydrocarbon recovery, Petroleum Geoscience, v. 7, p. 163–172.

Sullivan, K. B., and K. J. Schepel, 1995, Borehole image logs: Applications in fractured and thinly bedded reservoirs, SPWLA 36th Annual Logging Symposium, p. T.

Thomsen, L., 1986, Weak elastic anisotropy, Geophysics, 51, 1954-1966.

Tirado, S., 2004, Sand thickness estimation using spectral decomposition, University of Oklahoma, Masters Thesis.

Vertical Resolution Horizontal Resolution Fresnel Zone, 2004, http://www.geol.lsu.edu/juan/ReflectSeismol03/resolution.htm

Widess, M. B., 1973, How thin is a thin bed?, Geophysics, v. 38, p. 1176-1180.

Witton-Barnes, E. M., N. F. Hurley, and R. M. Slatt, 2000, Outcrop and subsurface criteria for differentiation of sheet and channel-fill strata: Example from the Cretaceous Lewis Shale, Wyoming, GCSSEPM Foundations 20th Annual Research Conference, p.1087-1104.

Young, R., 1999, Introduction to Seismic Exploration class notes, Fall 1999 semester.